TiO_2 AND ZnO LOADED FLY ASH CATALYSTS

by

Duygu TUNCEL

B.S., Chemistry, Yıldız Technical University, 2012

Submitted to the Institute for Graduate Studies in
Science and Engineering in partial fulfillment of
the requirements for the degree of
Master of Science

Graduate Program in Chemistry
Boğaziçi University
2014

TiO_2 AND ZnO LOADED FLY ASH CATALYSTS

APPROVED BY:

Assoc. Prof. Ayşe Neren Ökte …..……..……....
(Thesis Supervisor)

Prof. Zekiye Çınar ………………….

Prof. İlknur Doğan …………….……

DATE OF APPROVAL: 06.06.2014

ACKNOWLEDGEMENTS

First of all, I would like to thank to my supervisor Assoc. Prof. Ayşe Neren Ökte for her invaluable guidance, patience, encouragement and help in every stage of this thesis and during my education in Boğaziçi University. I have tried to learn the spirit of research and being a virtuous researcher from her. I am really grateful to have the chance to know and work with her. She has a place in my life more than a teacher.

I also express my thanks to Prof. Zekiye Çınar and Prof. İlknur Doğan for being my committee members and spending their valuable time. And special thanks to Prof. Zekiye Çınar; being her undergraduate thesis student was an honour and an unprecedented scholarly experience for me.

And also, many thanks to Assist. Prof. Dimitris Karamanis from University of Ioannina, Department of Environmental and Natural Resources Management, Agrinio, Greece. He supplied all fly-ashes used in our lab from Greece.

I would like to extend my thanks to all the faculty members in the Boğaziçi University Chemistry Department for their altruism and kindness during my master education. I wish to thank Bilge Gedik Uluocak for SEM analysis and Erkan Karabekmez for XRD analysis.

I owe thank to my laboratory colleagues Hazal Pekcan and Taner Özden for their help during the experimental part as well as the theorical part of this thesis. It was delightful to be working in the same laboratory. I would also like to thank to Birses Debir, Ege Uysal, Sesil Agopcan, Can Şekerci, and Canses Erkol for moral support and friendship. I wish to thank to Gökçe Sürmen for providing me a sistership in this life.

It is a good opportunity to express my thanks to my father (Mehmet Hasan Tuncel) and my mother (Feride Sunar Tuncel) who dedicate their life to me without hesitating and to my uncle (Rıza Şadi Ölçüm) who is always as close as a father for me. And my brother (Baki Saim Tuncel) to give me a chance for experience being a sister.

And extra thanks to my dear grandmother (Gülsüm Ölçüm) who is the most impressive person in my life. They always support me and make a great effort with me for my success. I am evermore indebted them for their unconditional love, support and sensibility during my life.

To the memory of Soma miners...

This study was supported by Boğaziçi University Research Foundation (Project No. 11B05P4 and 13B05P7) and also by the framework of the Joint Research and Technology Programs between Turkey (TUBITAK, 209T109) and Greece (General Secretariat for Research and Technology and European Regional Development Fund, GSRT 10 TUR/1-25-1) (2011–2013).

ABSTRACT

TiO_2 AND ZnO LOADED FLY ASH CATALYSTS

In this study, two binary catalysts TiO_2 supported fly ash (TiO_2-FA) and ZnO supported fly ash (ZnO-FA) were sythesized by sol-gel and co-precipitation technique. The as-prepared catalysts were characterized by using several analytical methods and their photocatalytic activities were examined for degradation of methyl orange (MO) under UV irradiation. X-ray diffractometer (XRD), scanning electron microscopy (SEM) with energy dispersive X-ray (EDX) and elemental mapping analysis, surface area analyzer (BET) and UV-vis diffuse reflectance spectrometry (UV-vis DRS) were used for the characterization of the catalysts. XRD analysis supplied information about the anatase phase of TiO_2 and ZnO crystallite. The particle sizes of TiO_2 in the supported catalysts remained almost the same values while ZnO exhibited reduced crystalline sizes on the ZnO-FA catalysts. SEM (EDX) images revealed variations in the surface morphology of the raw FA after loaded with TiO_2 or ZnO nanoparticles. The surface area measurements (BET) of the supported catalysts indicated the formation of mesoporous structures. The supported catalysts revealed higher dark adsorption capacities, following pseudo-second order kinetics. Langmuir adsorption isotherm was well fitted to the experimental data obtained in the dark for both supported catalysts. The loading amounts of the TiO_2 and ZnO nanoparticles were effective in the photocatalytic degradation experiments and the best performances were obtained in the presence of 40% TiO_2-FA and 0.5M ZnO-FA catalysts. The photocatalytic reactions obeyed the pseudo-first-order kinetics by varying the initial concentrations of the MO. Langmuir-Hinshelwood model was also applicable. The repeatability in the photoactivities of the supported catalysts were confirmed by the recycling studies. A mechanism was postulated for MO degradation. The supported catalysts did not show an activity under visible light irradiation.

ÖZET

TiO_2 VE ZnO KATILIMLI UÇUCU KÜL KATALİZÖRLERİ

Bu çalışmada, TiO_2 destekli uçucu kül (TiO_2-FA) ve ZnO destekli uçucu kül (ZnO-FA) katalizörleri sırasıyla sol-jel ve çöktürme teknikleri kullanılarak sentezlenmiştir. Hazırlanan katalizörler çeşitli analitik yöntemler kullanılarak karakterize edilmiş ve metil oranj model maddesi varlığında UV ışığı altında fotokatalitik aktiviteleri incelenmiştir. Katalizörlerin karakterizasyonu için X-ışını kırınım ölçer (XRD), enerji dağınımlı X-ışınları analizi ve elementel dağılım haritası beraberindeki taramalı elektron mikroskobu (SEM-EDX), yüzey alanı analizi (BET) ve dağınık yansıtmalı UV-vis spektometresi (UV-vis DRS) kullanılmıştır. XRD analizi ile TiO_2 anataz ve ZnO kristal fazı hakkında bilgi sağlanmıştır. Destekli katalizörlerde ZnO kristal boyutu azalırken, TiO_2 kristal boyutu aynı değerlerde kalmıştır. SEM (EDX) görüntüleri, saf uçucu küle TiO_2 ve ZnO nanopartiküllerinin eklenmesiyle oluşan değişimleri göstermiştir. Destekli katalizörlerin yüzey alanı ölçümleri ile mezofor yapı oluşumu saptanmıştır. Destekli katalizörler daha iyi adsorpsiyon kapasitesi sergilemiş ve görünür ikinci mertebe kinetiği izlemiştir. Her iki katalizör için de karanlık ortamda elde edilen deneysel veriler Langmuir adsorpsiyon izotermi ile uyumluluk göstermiştir. Katalizördeki TiO_2 ve ZnO nanopartikül miktarları fotokatalitik bozunma deneylerinde etkileyici olmuş ve en yüksek performanslar 40% TiO_2-FA ve 0.5M ZnO-FA katalizörleri varlığında elde edilmiştir. Farklı MO başlangıç konsantrasyonları kullanılarak yapılan fotokatalitik reaksiyonlar görünür birinci mertebe kinetiğine uymuştur. Langmuir-Hindhelwood kinetik modeli ayrıca incelenmiştir. Katalizörlerin fotokatalitik aktivitelerinin tekrarlanabilirliği, yeniden kullanım çalışmaları ile teyit edilmiştir. Metil oranj bozunması için bir mekanizma öngörülmüştür. Katalistler görünür ışık altında aktivite göstermemiştir.

TABLE OF CONTENTS

LIST OF FIGURES

LIST OF TABLES

LIST OF SYMBOLS

D	Crystal Size
e^-	Electron
E_{bg}	Band Gap Energy
h^+	Hole
k_{app}	Appearent Rate Constant
k	Reaction Constant
K	Adsorption Constant
l	Path length of the Spectrophotometer
Ω	Omega
λ	Wavelength of X-ray radiation
θ	Angle between X-ray radiation

LIST OF ACRONYMS / ABBREVIATIONS

AOP	Advanced oxidation process
BET	Surface Area
CB	Conducton Band
DRS	Diffuse Reflectance Spectroscopy
EDX	Energy Dispersive X-Ray
FA	Fly ash
FWHM	Full Width Half Maximum
MO	Methyl Orange
XRD	X–Ray Diffraction
SA	Salicylic acid
SEM	Scanning Electron Microscopy
TiO_2	Titaniumdioxide
UV-Vis	Ultra Violet-Visible
VB	Valence Band
ZnO	Zinc oxide

1. INTRODUCTION

Heterogeneous photocatalysis stands out as an impressive technique leading to degradation of toxic compounds to non-hazardous forms. Utilization of illuminated semiconductors and their applications under ambient conditions point out the increased interest in the heterogeneous photocatalytic reactions. In summary, the mechanism of these reactions is initiated by the band-gap illumination and formation of electron-hole pairs. After separation, electrons and holes migrate to the catalyst surface, induce redox reactions with adsorbed pollutants and eventually resulting in the degradation of the pollutants. TiO_2 has proven to be the most suitable photocatalyst for widespread environmental applications owing to its high photoactivity, non toxicity and chemical stability. In the past few years, ZnO has attracted much attention because of its distinctive optoelectronic, low cost, catalytic and photochemical properties. In some cases, ZnO has revealed higher activities than TiO_2 owing to the smaller particle sizes and better dispersion. Moreover, ZnO functions in a larger fraction of UV spectrum. However, there are certain disadvantages in the usage of bare TiO_2 and ZnO catalysts. The nanosized particles show rapid deactivation in bulk due to increased tendency of aggregation which eventually reduces the light incidence. In addition, poor adsorption capacity (by being non-porous), the low surface area and recycling difficulties owing to long time centrifugation or sedimentation processes restrict the utilization of these bare forms in the photocatalytic reactions. To minimize these problems, recent studies have been focused on the immobilization of TiO_2 and ZnO nanoparticles on some adsorbents like silica, alumina, activated carbon, zeolite and clay. Such materials provide higher surface areas and more effective adsorption sites. The enhanced degradation rates can be attributed to the increased condensation of pollutants on the supported catalysts by adsorption and the reduced electron-hole recombination process on the surface.

Fly ashes (FA) are aluminosilicate-rich by-products generated in coal firing powder plants. They are unique, non-toxic, chemically and physically stable, abundant and cheap, hollow particles. They can be beneficially used in the building industry and road construction applications such as cement or asphalt additive, concrete block, highway ice control, hazardous waste removal etc. In spite of these applications, the large quantities fly ashes produced by industry create environmental waste. Therefore, the development of alternative potential applications and further means to facilitate the recycling of ashes are needed.

In this study, two binary composites were prepared; TiO_2 supported fly ash (TiO_2-FA) and ZnO supported fly ash (ZnO-FA) by using a sol-gel technique and a co-precipitation method, respectively. Characterization of the as-prepared catalysts were done by X-ray diffraction (XRD) analysis, scanning electron microscopy (SEM), energy dispersive X-ray (EDX) analysis and elemental mapping, surface area (BET) measurements and UV–vis diffuse reflectance spectra (UV–vis DRS).

The photocatalytic performances of the catalysts were controlled under UV light irradiation by using methyl orange (MO) as the probe molecule. The kinetics were examined both in the dark and under irradiation. Pseudo-first, pseudo-second order equations, Freundlich and Langmuir adsorption isotherms were employed to express the dark adsorption kinetics of the catalysts. The photocatalytic reactions followed pseudo-first-order kinetics by varying the initial concentrations of the MO and discussed in terms of Langmuir-Hinshelwood model. The effect of TiO_2 and ZnO loading amounts were examined in the degradation runs. The repeatability of the photocatalytic activities was tested. A plausible mechanism was proposed for the degradation routes of the MO molecule. The catalytic efficiencies were also evaluated under visible light irradiation in the presence of salicylic acid (SA) model compound.

2. THEORY

2.1. Heterogeneous Photocatalysis

Heterogeneous photocatalysis is an advance oxidation process which has proven to be a promising technology for degradation of organic compounds. Photocatalysis can be defined as “acceleration of a reaction in the presence of a photocatalyst” [1]. Photocatalytic reactions require a catalyst that can absorb light and generate active radical species [2].

Semiconductors are usually defined rather loosely as a material with electrical resistivity lying in the range of 10^{-2}-10^{-9} Ω cm. Semiconductors are crystalline materials whose outer shell atomic levels exhibit an energy band structure with an energy gap between the highest occupied energy band (valence band) and the lowest unoccupied band (conduction band). The band gap energy of semiconductors for electronic excitation differs from 0 eV to 3 eV [3].

When a semiconductor catalyst is illuminated with photons whose energy is equal to or greater than their band gap energy, the energy is absorbed by the semiconductor. With this absorption, an electron from the valence band (VB) is excited to the conduction band (CB), leaving behind a hole in the valence band. Thus in concert, electron and hole pair as reductant and oxidant, respectively, is created (Equation 2.1) [4].

$$\text{Semiconductor} + hv \rightarrow e_{CB}^{-} + h_{VB}^{+} \qquad (2.1)$$

Both these entities can migrate to the catalyst surface, where they can enter in a redox reaction with other species such as organic compounds adsorbed on the surface.

The photogenerated hole is enough to directly oxidize the organic dye molecule to form R^{+} and decompose it as shown in Equation 2.2.

$$h_{VB}^{+} + \text{dye} \rightarrow \text{dye}^{\bullet+} \rightarrow \text{dye (decolorization and degradation)} \qquad (2.2)$$

On the other hand, the hole can react with surface adsorbed water (Equation 2.3) or hydroxyl anion for oxidizing them into hydroxyl radical (Equation 2.4) whereas photoexcited electron can react with O_2 to produce superoxide radical anion of oxygen (Equation 2.5) [5].

$$h_{VB}^{+} + H_2O \rightarrow OH^{\bullet} + H^{+} \qquad (2.3)$$

$$h_{VB}^{+} + OH^{-} \rightarrow OH^{\bullet} \qquad (2.4)$$

$$e_{CB}^{-} + O_2 \rightarrow O_2^{\bullet -} \qquad (2.5)$$

These reactions prevent the recombination of the electron and the hole which are produced in the Equation 2.1.

The produced superoxide radical, $O_2^{\bullet -}$, is known as oxidizing agent and contributes to the formation of the hydroxyl radicals through generation of hydrogen peroxide and hydroperoxyl radical [6].

$$O_2^{\bullet -} + H^{+} \rightarrow HO_2^{\bullet} \qquad (2.6)$$

$$2HO_2^{\bullet} \rightarrow H_2O_2 + O_2 \qquad (2.7)$$

$$H_2O_2 + O_2^{\bullet} \rightarrow OH^{\bullet} + O_2 + OH^{-} \qquad (2.8)$$

The resulting $OH^{\bullet}$ radical (obtained in Equation 2.4 and 2.8) is known as highly reactive oxidizing agent with the standard redox potential +2.8 V and responsible for the heterogeneous photodecomposition of most organic substrates.

$$OH^{\bullet} + \text{dye} \rightarrow \text{decolorization and degradation} \qquad (2.9)$$

A schematic illustration of the process is shown in Figure 2.1.

The ability of a semiconductor to undergo photoinduced electron transfer to an adsorbed particle is governed by the band energy positions of the semiconductor and the redox potential of the adsorbates. The energy level of the conduction band can be thought as the reduction potential of photoelectrons and the energy level of the valence band determines the oxidizing ability of photoholes, each value reflecting the ability of the system to promote reductions and oxidations [7].

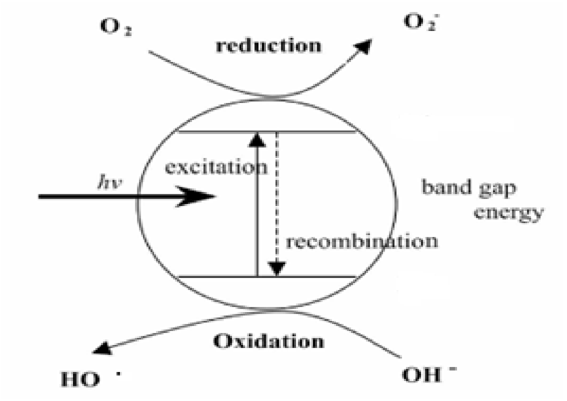

Figure 2.1. Photocatalytic degradation mechanism.

For an energetically feasible system, the conduction band minimum of the semiconductor has to be more negative than the reduction potential of H^+/H_2, while the valence band maximum needs to be more positive than the oxidation potential of O_2/H_2O (Figure 2.2) [8]. This means that the band gap energy of the photocatalyst must be around 3 eV with appropriate band positions.

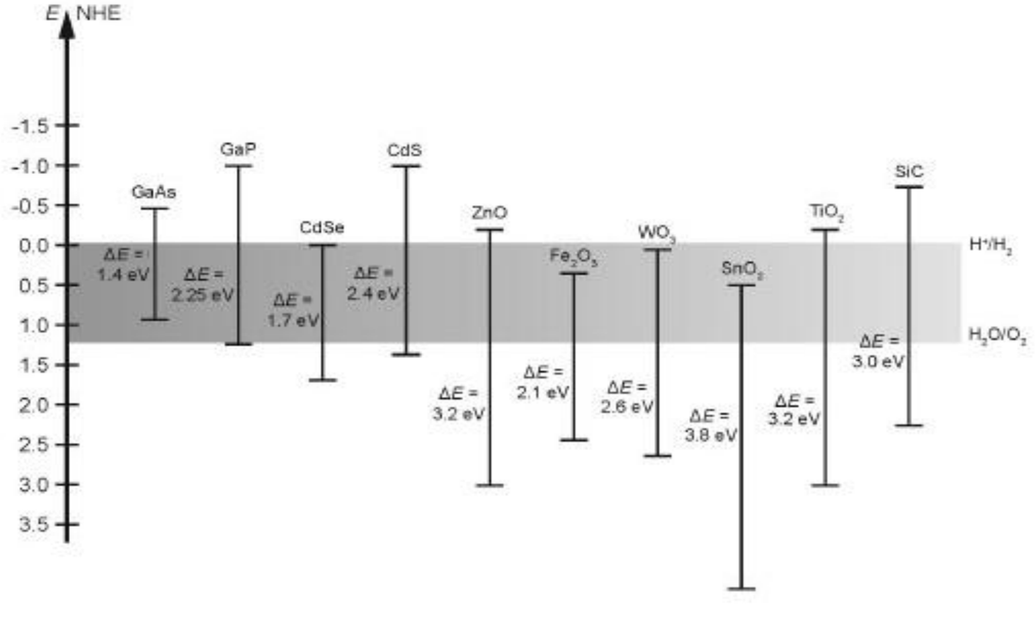

Figure 2.2. Band positions and band gap energies of the several semiconductors.

Figure 2.2. shows the band gap of the several semiconductors and some standart potentials of redox couples. Among all these semiconductors, the most widely used semiconductor catalyst for photocatalytic reactions are titanium dioxide (TiO_2) and zinc oxide (ZnO) due to the their valence and conduction band positions and value of the band gap energies. Moreover, a semiconductor photocatalyst should be chemically and biologically inert, photocatalytically stable, easy to produce, cheap and without risk for the environment or human.

2.2. Titanium Dioxide

Titanium is the one of the most widely found metal on the earth. It was discovered in 1971 in England by Reverend William Gregor. Titanium metal is not found unbound to other elements and that are present in various rocks and sediments. Its most common compound titanium dioxide (TiO_2) belongs to the family of transition metal oxides. In the beginning of the 20th century, industrial production of TiO_2 was started with using it as pigment for white paint. At present, the annual production of TiO_2 exceeds 4 million tons [9]. 31% of total production of TiO_2 is used as white pigment in paints, plastic, cosmetic and paper industries. The rest can be assorted in the versatile potential applications. For example, as a result of its high refractive index, it is used as anti-reflection coating in thin-film optical devices [10]. Due to its biocompatibility with the human body, TiO_2 appears as a biomaterial in biological or biomedical applications [11]. It is also utilized in solar cells for the production hydrogen and electric energy.

The photo-induced phenomena of TiO_2 was unfolded by the pioneering research of Fujishima and Honda in the early 1970’s. These workers revealed the possibility of water splitting by TiO_2 photoelectrochemical cell, then the application of TiO_2 photocatalysis extended to environmental frontiers. In 1977, Frank and Bard [12] for the first time, reported the photocatalytic application of TiO_2 for oxidation of CN^- and SO_3^{2-} in aqueous medium under solar light illumination. Afterwards, numerous researches have been done on decomposition of different pollutants utilizing photo-assisted TiO_2 systems, due to chemical-physical stability, non-toxicity, low cost and high photoactive nature of TiO_2.

Titanium dioxide exists in three mineral forms: anatase, rutile and brookite (Figure 2.3). The structures of rutile, anatase and brookite can be discussed in terms of (TiO_2^{6-}) octahedral. The three crystal structures differ by the distortion of each octahedral chains. Brookite was named in honor of English mineralogist, H. J. Brooke and was discovered in 1825. This type of TiO_2 has an orthorhombic crystalline structure. The brookite type TiO_2 does not exhibit photocatalytic activity.

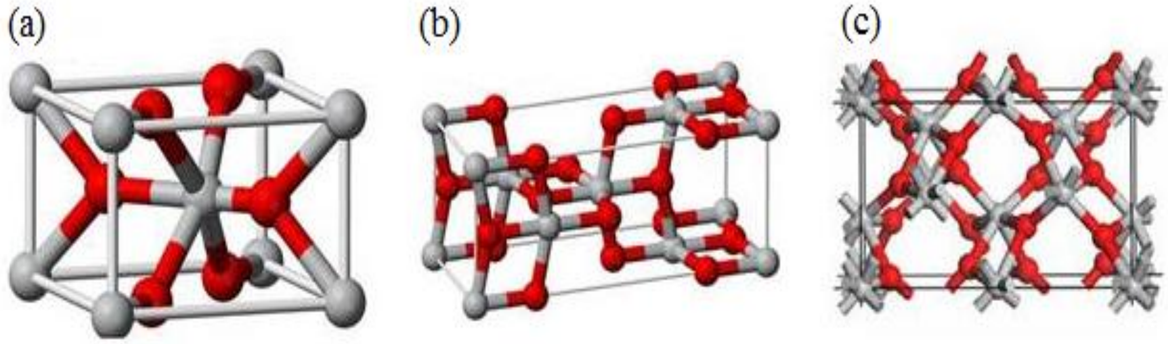

Figure 2.3. Crystal structures of rutile (a), anatase (b) and brookite (c).

Rutile is the most stable form of TiO_2 and the major ore of titanium was discovered in 1803. Rutile type TiO_2 also has a tetragonal crystal structure (with prismatic habit). This type of titania is mainly used as white pigment in paint.

Anatase type of TiO_2 has a crystalline structure that corresponds to the tetragonal symmetry. Anatase form was named by R. J. Hauy in 1801 from the Greek word “anatasis” meaning “extension”, due to its longer vertical axis compared to that of rutile [13].

Particle size experiments affirm that relative phase stability may reverse when particle sizes decrease sufficiently low values due to surface energy effects. If the particle sizes of the three crystalline phases are equal, anatase is most thermodynamically stable at sizes less than 11 nm, brookite is most stable between 11 and 35 nm and rutile is most stable at sizes greater than 35 nm [14]. Anatase is the low-temperature stable form and rutile is the dominant form in high temperature preparations. The reduced density of anatase as compared to rutile (3.89 g/cm^3 versus 4.26 g/cm^3) leads to significant differences in many physical properties.

Rutile and anatase phases have different activities for photocatalytic reactions. Many studies exhibited that pure anatase phase is the most photo active cyristalline form of TiO_2. The higher photocatalytic activity of anatase form is assumed because of the difference between their optical bandgap. Kavan *et al.* [15] point out that the difference between the 3.2 eV band gap of anatase and the 3.0 eV bandgap of rutile lies mainly in the position of the conduction band edge, the edge for anatase being around 0.2 eV higher than that of rutile (Figure 2.4).

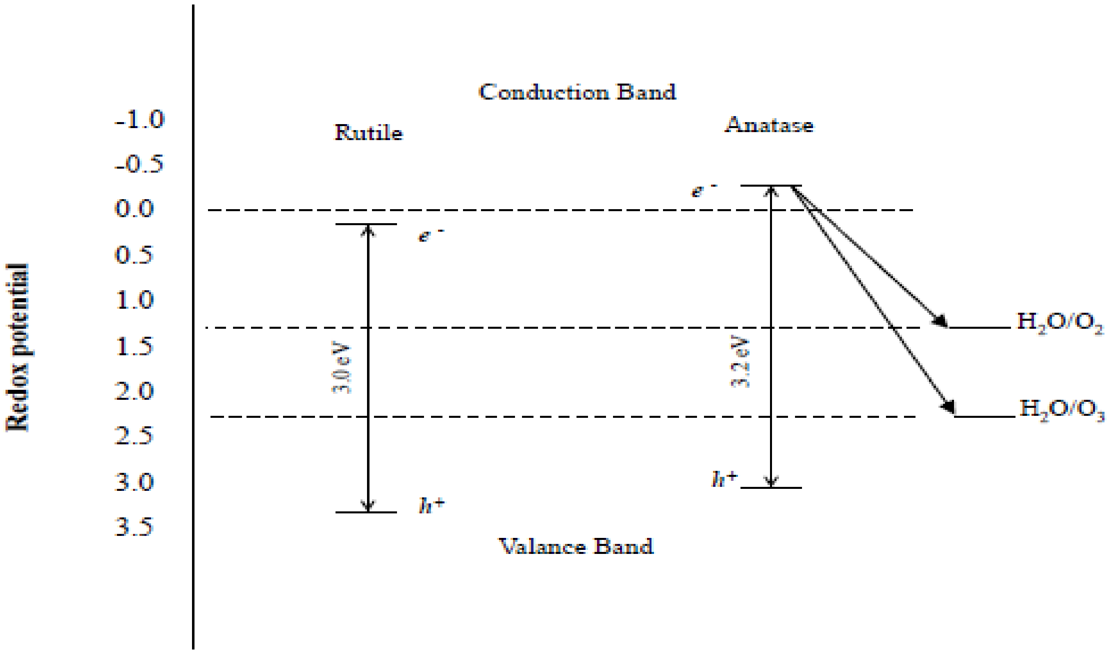

Figure 2.4. Band positions of rutile and anatase cyrstal forms of TiO_2.

2.3. Zinc Oxide

Zinc element is one of the oldest metal that has been recognized through the science history. The name of the metal was first documented by German alchemist Paracelsus who referred to the metal as "zincum" or "zinken" in the 16th century.

Zinc oxide (ZnO) is an oxidic compound naturally occurring as the rare mineral zincite which was discovered in 1810 by Dr. Archibald Bruce. ZnO is a polar crystal and exhibits a wurtzite structure with hexagonal unit cell (Figure 2.5) [16]. At ambient conditions, wurtize phase shows a thermodynamically stable form.

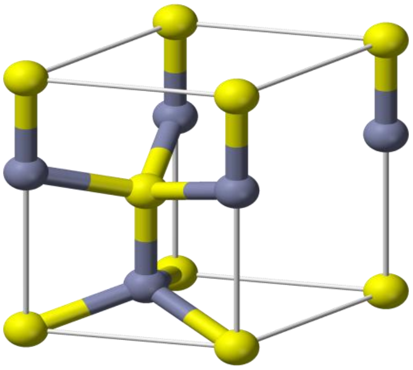

Figure 2.5. Crystal structure of wurtizite

With the beginning of the semiconductor age after the invention of the transistor [17], systematic investigations of ZnO as a compound semiconductor were performed. Today, 10^5 tons of ZnO is produced per year for industrial use [18].

ZnO is a good semiconducting material for photocatalytic applications, due to its environmental stability, low cost and great photochemical properties when compared with other nanosized metal oxides. Especially recent years, ZnO has investigated to be an efficient catalyst concerning water detoxification [19], with high reaction and mineralization rates [20]. Moreover, in some cases, ZnO has revelaed higher photocatalytic activity than TiO_2 owing to the smaller particle size that leads to better dispersion [21,22]. The biggest advantage of ZnO in comparison with TiO_2 is that ZnO absorbs over a larger fraction of solar spectrum thereby can be activated under even visible irradiation. Hence, ZnO has been emerged as a suitable alternative photocatalysts to TiO_2.

2.4. Factors Affecting Surface and Morphological Aspects in Photocatalysis

2.4.1. Surface Area

In photocatalysis, large surface area can be the determining factor of adsorbed organic molecules which promotes the reaction rate. However, powders with a large surface area usually associated with large amounts of crystalline defects, which favour the recombination of electrons and holes leading to a poor photoactivity [23].

BET theory is a rule for the physical adsorption of gas molecules on a solid surface and serves the measurement of the specific surface area of a material as a basis important analysis technique. BET stands for Brunauer, Emmett and Teller, who optimized the theory in 1938 [24]. The concept of the theory is an extension of the Langmuir theory, which is a method for monolayer molecular adsorption, to multilayer adsorption. According to the BET theory, the amount of the adsorbated gas corresponding to a monomolecular layer on the surface and due to the non-being interaction between each adsorption layer, the Langmuir theory can be applied to each layer. The determination is carried out at the temperature of liquid nitrogen. A BET isotherm is not accurate at all pressure, but used in many application areas to determine the surface areas of solids by interpreting of adsorption-desorption isotherms [25].

2.4.2. Particle Size

Particle size of a catalyst is one of the most important parameter that can affect the degradation efficiency. It is well known that in the nanometer size range, physical and chemical properties of semiconductors are modified (compared with bulk). Small variations in particle diameters lead to great modifications in the surface/bulk ratio, thus modifying the significance of volume and surface electron-hole recombination. When the size of the catalyst particle decreases, photon absorbance increases due to the increase in the amount of the dispersion particles per volume in the solution [26]. Also, the surface area of the photocatalyst increases which promotes the adsorption of more dye molecules on the surface. Additionally, electron-hole recombination will be suppressed [27].

The average particle sizes are determined by the application of Scherrer's equation (Equation 2.10) to the (101) diffraction of anatase [28] and (101) diffraction of ZnO [29]

$$D = \frac{A\lambda}{FWHM \ \cos\theta} \tag{2.10}$$

where D is the average crystal size, A is Scherrer's Constant (0.94), λ is the wavelength (0.1542 nm), FWHM is full width half maximum value of the corresponding diffraction peak and θ is the diffraction peak angle.

2.4.3. Sol-Gel Method: Preparation of TiO_2 Nanoparticles

Sol-gel method is used for the synthesis of thin films, powders, and membranes. Sol–gel is one of the most successful technique for preparing nanosized metal oxide materials with high photocatalytic activities [30].

The process of sol–gel materials in general include a wet-chemical process to form a precursor sol or gel solution followed by a heat treatment to convert the amorphous precursor into crystalline particles [31]. This method is based on basically phase transformation of a sol obtained from metallic alkoxides or organometallic precursors. The non-alkoxide route uses inorganic salts (such as nitrates, chlorides, acetats, carbonates, etc.) which requires an additional removal of the inorganic anion while the alkoxide route uses metal alkoxides as starting material. The metallic alkoxide route involves the formation of TiO_2 sol-gel by hydrolysis and condensation of alkoxides precursors. These reactions are pursued by thermal treatment (450-600^o C) to remove the organic part and to cyrstallize anatase TiO_2 [32]. However, very high calcination temperature results in aggregation or phase transformation, and affects the microstructures as well as the properties of TiO_2 nanoparticles.

The sol–gel process offers many advantages for preparing oxide catalysts such as low cost, ease of processing and stochiometric control [33]. By tailoring the chemical structure of primary precursors and carefully controlling the processing variables, nanocrystalline products with very high level of chemical purity can be achieved. In addition, the processing provides for excellent chemical homogeneity and the possibility of deriving unique stable structures of catalysts at low temperatures [34].

2.4.4. Co-precipitation Method: Preparation of ZnO Nanoparticles

The synthesis method of ZnO nanoparticles is particularly important because of their size and/or surface properties dependence. These particles present different chemical, electrical, optical and mechanical properties compared to their corresponding bulk solid.

Several methods have been reported for ZnO nanoparticle synthesis. However, the large-scale methods are thought unfavorable due to expensive raw materials, complex process control and sophisticated equipment [35]. Among the synthesis techniques, the co-precipitation method stands out an easier and cheaper alternative route. The co-precipitation route exhibits several advantages: requires minimal manipulation, simple equipment, cheap raw materials, low synthesis temperature, easier compositional and particle size control by varying the reaction conditions and initial reactants ratio. Hence, this precipitation technique can be applied for low temperature synthesis of high purity and excellent chemical homogeneity ZnO nanoparticles. The main disadvantage of co-precipitation is the fact that process is limited to cationic solutions with similar solubility products. The most common starting materials used are hydroxides, carbonates, sulphates and oxalates [36].

2.5. Support

In heterogeneous photocatalysis, a powder form catalyst is generally suspended in wastewater to degrade pollutants. Although TiO_2 and ZnO are known as the most favorite photocatalysts, there are certain limitations of using bare forms of these semiconductors. In suspension systems, the small particle size of the catalysts has tendency to rapid agglomeration that inhibiting active sides of the photocatalysts and eventually reduce the catalytic efficiency [37]. Also, the small particle size leads to high filtration costs of catalyst removal and recycling difficulties, thus hindering its industrial application [38,39]. For this reason, the synthesis of photocatalysts with high activity and effective reuse properties simultaneously is a priority topic. In addition, because of the non-porous structure of the metal oxide catalysts, bare TiO_2 and ZnO exhibit low adsorption ability for the pollutants in wastewater.

These problems have motivated the development of supported photocatalysts, wherein photocatalysts are immobilized on the adsorbent materials such as, silica [40], alumina [41], activated carbon [42], clay [43], zeolite [44].

Adsorption properties are strongly influenced by the chemical nature of the pollutant and the surface properties of the support. A supporting material should sufficiently bond either via physically or chemically to the photocatalyst without reducing the its reactivity. The basic concept is based on the physisorption of reactants on inert substrates followed by their surface diffusion to the interface between the adsorptive sites and photocatalytic sites. The first step is achieved by using supports with large surface areas for adsorption and high adsorption capacity for the target substances, while the second is achieved only if the adsorption strength is moderate enough to allow diffusion of adsorbed substrates to the loaded TiO_2 [45]. A support material should have stability against degradation by strong oxidative radicals generated by the photocatalyst. Moreover, non-toxicity is an urgent property as a support material for consideration environmental aspects. On the other hand, the costs of support materials have to be seriously consideration when putting them into applications. Based on these criteria, fly ash can be investigated and utilized as a support material for TiO_2 and ZnO photocatalysts.

2.5.1. Fly Ash

Fly ash is a fine grey powder and is the principal by-product generated during coal combustion process [46]. Fly ash consists of particles arising from the combustion of pulverized coal at high temperatures ranging from about 1400 °C to 1700 °C [47]. Wide scale coal firing for power generation began in the 1920s [48] and since then large quantities of fly ash have been produced in power plants throughout the world every year. Fly ash accounts for approximately 75-80% of the total ash produced from the combustion of pulverized coal in power plants [49]. As of 2010, the estimated annual amount of fly ash produced worldwide was 600 million tons [50]. The generation of coal fly ash is anticipated to increase for many more years, as a result of the world’s increasing reliance on coal-fired power generation.

Fly ash is a ferro aluminosilicate-rich inorganic material. The primary minerals in fly ash can be listed as 60-65% silica (SiO_2), 25-30% alumina (Al_2O_3) and 6-15% iron oxide (Fe_2O_3) [51]. The most common elements found in fly ash include Si, Al, Fe, Ca, Mg, K and Na. Fly ash may also contain trace elements such as As, Zn, Pb and Se [52]. An empirical formula for fly ash based on the dominance of certain key elements has been proposed as : $Si_{1.0}\ Al_{0.45}\ Ca_{0.51}\ Na_{0.047}\ Fe_{0.039}\ Mg_{0.020}\ K_{0.013}\ Ti_{0.001}$

Fly ash consists of fine, powdery particles predominantly spherical in shape, either solid or hollow, and mostly glassy (amorphous) in nature. The carbonaceous material in the fly ash is composed of angular particles [53]. The specific gravity of fly ash usually ranges from 2.1 to 3.0, while its specific surface area may vary from 170 to 1000 m_2/kg [54]. The hollow spheres found in fly ash, commonly known as “cenospheres”, vary in size ranging between 45 μm and 150 μm [55]. The cenospheres, are formed as a result of thermochemical transformations of mineral particles during coal combustion process, where the minerals melt to form small droplets, which upon sudden cooling and action of surface tension forces adopt the spherical shape [56]. Fly ash particles have a smooth outer surface which is due to the presence of the aluminosilicate glass phase [57]. The colour of fly ash can vary from tan to gray, depending on the amount of unburned carbon in the ash.

Currently, the main application of fly ash is building industry and road construction enclosing cement, brick and asphalt production. Other uses include soil amelioration [58], zeolite synthesis [59], ceramic industry [60], geompolymer synthesis [61] and valuable metals recovery [62]. In spite of these applications, the large quantities produced fly ash still creates environmental pollution. Therefore, researches focus to find out the various ways to utilize this by-product to prevent any environmental problems as well as effectively use it.

The attracting physicochemical characteristics of fly ash, such particle size, porosity and surface area makes it suitable for use as an adsorbent material. Additionally, fly ash particles are easy to separate from water because of their larger particle size and heavier weight comparing with nanometer sized TiO_2 and/or ZnO particles. Among the other adsorbent materials, fly ash (FA) appears an attractive support material for TiO_2 and ZnO owing to the fact that its unique structure, non-toxicity, high chemical and physical stability and low-cost.

2.6. Literature Survey

The removal of chlorophenols in the presence of fly ash materials was carried out by Kao *et al.* [63]. The adsorbed amount of chlorophenol by fly ash was affected by particle diameter, carbon content, and the specific surface area of the ash. The ash with a higher carbon content revealed larger surface areas and efficient adsorption capacities. Moreover, the adsorbed amount of chlorophenol was not influenced by the matrix in the wastewater.

In order to separate TiO_2 photocatalyst more easily from the treated wastewater, TiO_2 immobilized on a coal fly ash by using a precipitation method [64]. The crystalline structure was anatase in the supported matrix with a size of 9 nm. Under UV irradiation, the removal rate of NO gas was 63–67.5% in the presence of the TiO_2-coated coal fly ash.

In 2007, Çetin and Pehlivan presented a comparative study about the ability of fly ash and activated carbon to remove Ni^{2+} and Zn^{2+} from an aqueous solution [65]. Kinetic studies showed that an equilibrium time of 1 h was required for the adsorption of Ni^{2+} and Zn^{2+} on both adsorbents. With an increase in the concentrations of these metals, the adsorption of Ni^{2+} and Zn^{2+} decreased on both of the adsorbents. The effectiveness of fly ash as an adsorbent improved with increasing calcium content. Adsorption data in the range of pH values (3.0-8.0) using Ni^{2+} concentration of 25 ± 2 mg/L and Zn^{2+} concentration of 30 ± 2 mg/L in solution were correlated using the linear forms of the Langmuir and Freundlich equations.

Mohan and Gandhimathi investigated the possibility of the utilization of coal fly ash as a low cost adsorbent material for the adsorption of heavy metal ions (Zn, Pb, Cd, Mn and Cu) present in the municipal wastes [66]. Batch experiments were conducted to determine the effect of contact time and fly ash dosage. Experimental data were evaluated to find out kinetic characteristics of the adsorption process. The isothermal data could be well described by the Freundlich adsorption model. Kinetic parameters of adsorption such as the pseudo first-order constant, pseudo second-order constant and the intraparticle diffusion rate constant were determined. The fly ash concentration required to achieve maximum heavy metal removal was found to be 2 g/L with the removal efficiencies of 39%, 28%, 74%, 42% and 71% for Cu, Mn, Pb, Zn and Cd respectively. The results of the study demonstrated that the fly ash could be used as an effective low cost adsorbent for the removal of heavy metal ions from municipal wastes.

Visa *et al.* investigated treatment of wastewater in the presence of methyl orange and heavy metals on TiO_2, fly ash and their mixture [67]. The fly ash morphology was controlled by using AFM and XRD analysis. The adsorption parameters (contact time, wastewater volume, adsorbent mass ratio) were optimized and the adsorption mechanisms were discussed. The adsorption of cadmium and copper ions was found to be significant in the exitence of the FA modified TiO_2. The best adsorption efficiency was registered on mixture with 25% of TiO_2 content. The photodegradation experiments conducted on the substrate mixtures. The increase of FA content did not affect the efficiency of the process,. Dye concentration played a significant role in the photodegradation mechanism.

In 2010, Huo *et al.* prepared the TiO_2/fly-ash via sol-gel method and modified the surface of TiO_2/fly-ash cenospheres by hydrogen peroxide (H_2O_2) [68]. SEM, XRD, UV-vis DRS, photoluminescence (PL) and X-ray photoelectron spectroscopy (XPS) were applied to characterize the structure, performance and chemical composition of as-prepared samples. The photocatalytic activity of as-prepared samples was evaluated by degradation of methylene blue under visible light irradiation. The modified photocatalyst of TiO_2/fly-ash was effective for the absorption of light. The photocatalytic degradation of methylene blue enhanced under visible light irradiation, with 42.5% higher degradation rate than the untreated TiO_2/fly-ash.

In the study of Huo *et al.*, floating fly-ash cenospheres supported $AgCl/TiO_2$ films photocatalysts were prepared by a simple sol-gel method [69]. The catalysts were characterized by XRD, SEM, thermo gravimetric analysis-differential scanning calorimeter (TG-DSC), UV-vis DRS. The results showed that the fly-ash cenospheres were coated with about 2 μm thickness of $AgCl/TiO_2$ nano-composite films with high visible-light- activity for the decomposition of Rhodamine B in waste water. When the photocatalyst contained the dosage of 0.21 g AgCl, the photo-degradation rate could reach 94.96% in 180 min.

In 2011, Fe^{3+}-doped TiO_2 film deposited on fly ash cenosphere (Fe-TiO_2/FAC) was successfully synthesized by the sol-gel method. These photocatalysts were characterized by XRD, SEM and thermogravimetric analyses (TGA) [70]. The XRD results showed that Fe element may maintain metastable anatase phase of TiO_2. At 650^{o}C, rutile phase appeared for 0.01% Fe-TiO_2/FAC. The SEM analysis revealed the Fe-TiO_2 films on the surface of a fly ash cenosphere with a thickness of 2 μm. The absorption threshold of Fe-TiO_2/FACs shifted to a longer wavelength compared to the photocatalyst without Fe^{3+}-doping in the UV-vis absorption spectra. The photocatalytic activity and kinetics of Fe-TiO_2/FAC with varying the iron content and the calcination temperatures were investigated by measuring the photodegradation of methyl blue (MB) under visible light irradiation. Compared with TiO_2/FAC and Fe^{3+}-doped TiO_2 powder (Fe-TiO_2), the degradation ratio using Fe-TiO_2/FAC increased by 33% and 30%, respectively, and the best calcined temperature was 450^{o}C and the optimum doping of Fe/Ti molar ratio was 0.01%.

The TiO_2/fly-ash cenosphere photocatalysts modified with heteropolyacid were synthesized by using sol-gel method and observed for the degradation of ciprofloxacin (CPFX) under visible light irradiation [71]. Chemical composition and optical absorption of the novel catalysts were characterized by XRD, UV-vis DRS, Fourier Transform Infra Red spectroscopy (FTIR) and SEM. It was found that heteropolyacid modification could facilitate the absorption edge of TiO_2/fly-ash cenosphere photocatalyst to shift the visible light region. The result from degradation of CPFX suggested that the photocatalytic activity of TiO_2/fly-ash cenospheres modified with silicotungstic acid was superior. The synergistic effects of heteropolyacid in modified TiO_2/fly-ash cenospheres photocatalyst particles were responsible for improving visible light photocatalytic activity.

Wang *et al.* investigated the polypyrrole-sensitized TiO_2 layer on fly ash cenosphere (PPy-TiO_2/FAC) [72]. This photocatalyst could float in water due to the low density of FAC, which can take advantage of sunlight in its industrial application. The size and shape of FAC, TiO_2/FAC and PPy-TiO_2/FAC were presented by SEM images. XRD analysis showed that the dope of PPy did not change the crystallization performance of TiO_2. UV-vis diffuse reflectance spectra confirmed that PPy-TiO_2/FAC absorbed more photons under visible light irradiation. The experimental results indicated that PPy-TiO_2/FAC showed higher photocatalytic activity than TiO_2/FAC on the degradation of MB and phenol due to the sensitizing effect of PPy.

In another study, surface imprinted TiO_2/fly-ash photocatalyst was prepared by molecular imprinted technology with coordination compounds of La^{3+} and oxytetracycline as molecular template [73]. The phase, surface structure and light absorption of as-prepared imprinted photocatalyst were characterized by XRD, SEM, UV-vis DRS and FT-IR, respectively. The preferentially selected degradation and activity of imprinted photocatalyst were evaluated by degradation of different antibiotics in waste water. The results indicated that molecular/ions surface imprinted photocatalyst could preferentially degrade tetracycline antibiotic effectively and enhance the photocatalytic activity. The degradation rate of oxytetracycline ligand molecular could reach 76% in 60 min under visible light irradiation.

Visa and Duta syntesized TiO_2/fly ash substrate and tested removal of heavy metals (Cd^{2+} and Cu^{2+}) and surfactants (1-hexadecyltrimetylammonium bromide HTAB and dodecylbenzenesulfonate-SDBS) from synthetic wastewaters containing two (heavy metal + surfactant) and three pollutants (two heavy metals + one surfactant), in a single step process, involving adsorption and photocatalysis [74]. The substrate proved to be highly efficient in heavy metals adsorption and the TiO_2 layer on the fly ash grain support demonstrated a good activity in surfactants photodegradation. The adsorption kinetics, mechanisms and the substrate capacities were further discussed with the surface caracterization studies XRD, EDX, FTIR, SEM and AFM. The FA-TiO_2 structural and morphology analysis showed that the substrate has a high crystallinity degree and a surface with broad open pores, efficient in heavy metals (cadmium and/or copper) removal from systems also containing surfactants (SDBS or HTAB). The new substrate had the grains in the micrometric range, representing thus a promising alternative to Degussa P25 slurries, allowing a simpler and cost effective method to recycle the substrate in industrial wastewater treatment processes.

Nitrogen-doped TiO_2 (N-TiO_2) composites supported by fly ash cenospheres were prepared and characterized for the photocatalytic applications [75]. The photocatalytic activity and kinetics of the composites produced at different calcination temperatures and with different nitrogen doping contents were studied under visible light irradiation by monitoring the degradation of methylene blue (MB). The MB degradation ratio of N-TiO_2/FAC (25%, 450^o C) was 10% higher than that of N-TiO_2 and 40% higher than that of TiO_2/FAC. It was observed in this study, these N-TiO_2/FAC composites floated in water and were recovered, and their original photocatalytic ability was retained after two cycles of reuse.

Lv *et al.* studied for preparation of nano-TiO_2/fly ash beads composite materials from $TiCl_4$ as the titanium source, urea as the precipitating agent $(NH_2)_2CO$ and $(NH_2)_2SC$ as the N and S source respectively, by hydrolysis-precipitation method [76]. The composite materials were characterized by SEM, EDS, XPS, and UV-vis spectrophotometer methods. The UV-vis absorption spectra results exhibited that the absorption edge of un-doped composites was 390 nm while that of doped composites red-shifted to 500 nm. The photocatalytic activity of composite materials was evaluated by degradation of methyl orange under visible light irradiation. After irradiation for 1 h, degradation rate of N, S co-doped-TiO_2/fly ash beads composite material reached 65%, while the degradation rate of bare TiO_2 was 6%. It was detected the fly ash beads with the hollow structure were provided as a spherical substrate for TiO_2 and TiO_2 coating was firmly combined with fly ash surface. The fly ash beads not only reduced the reunion effect, but also improved the operability and recycle of the catalyst.

In 2013, Li *et al.* studied on the preparation of fly ash/ nano-ZnO composite and its adsorption properties for reactive dyes from aqueous solution [77]. The fly ash/nano-ZnO composite was prepared by chemical precipitation method using waste fly ash, $ZnSO_4$ and $(NH_4)_2CO_3$ as raw materials and analyzed by specific surface area and XRD. Effects of important preparation conditions on the dye adsorption capacity of the composite were investigated. The fly ash/nano ZnO composite obtained under optimal conditions of Fly ash/ ZnO mass ratio of 1:0.5 reaction. This composite revealed higher adsorption capacities for four different reactive dyes, reactive turquoise blue KN-G, reactive brilliant blue KN-R, reactive brilliant red X-3B and reactive brilliant red KD-8B from aqueous solution.

Two-dimensional honeycomb-like ZnO nanowalls were fabricated on porous material of fly ash by simple sol-gel and hydrothermal synthesis method in order to maximize the specific surface area and photocatalytic performance [78]. The technologic parameters, such as calcination temperature, reaction time and the concentration of the growth solution were found to be important on the structure and photocatalytic activity of the catalysts. The degradation of methylene blue was about 90% after 30 min under UV irradiation in the presence of these composites.

In the study of Ökte and Karamanis, ZnO-Fly ash (ZnO-FA) catalysts has been prepared and tested for the degradation of methyl orange (MO) and water vapor adsorption toward evaporative cooling of hydrophilic surfaces [79]. BET measurements of the supported catalysts revealed type IV adsorption isotherms. In SEM images the non-shaped ZnO aggregates existed either on the surface of the FA spheres or heterogeneously dispersed over the whole catalyst matrix. XPS confirmed the buildup of ZnO nanoparticles while the form of Zn^{2+} oxidation state on the catalyst surface was demonstrated by the sharp Zn $2p_{3/2}$ peaks. The absorption edges in the UV-vis DRS of all supported catalysts were found to be slightly shifted to longer wavelength regions due to the existence of FA in the composite structure. Moreover, water vapor sorption was increased to 0.2 g/g in the presence of 0.25 M ZnO-FA from 0.037 g/g in the hydrophobic FA. Dark adsorption property of 0.5 M ZnO-FA was further enhanced under UV illumination.

Ökte *et al.* also prepared, characterized and evaluated activities of TiO_2-Fly ash catalysts [80]. XRD analysis supplied information about the generation of anatase phase . SEM images revealed variations in the surface morphology of raw FA after TiO_2 loading. Nitrogen adsorption-desorption isotherms indicated the formation of a mesoporous structure. XPS confirmed the buildup of TiO_2 nanoparticles on the FA matrix with the form of Ti^{4+} oxidation state. The supported nanocatalysts were tested for water vapor adsorption towards evaporative cooling of hydrophilic surfaces and for decolorization and degradation of methyl orange (MO) under UV irradiation. The mesoporous TiO_2-FA was found to be hydrophilic with capillary condensation in the water vapor adsorption isotherm. Kinetics was discussed in terms of Langmuir-Hinshelwood model. H_2O_2 was used as an electron scavenger and accelerated decolorization and degradation rates of MO.

3. EXPERIMENTAL

3.1. Materials

Fly ash was obtained from a lignite power plant in Greece and collected in a dry state from the electrostatic precipitators of a power station. All samples were grounded by hand and sieved to a fragment size less than 200 μm. Zinc nitrate hexahydrate ($Zn(NO_3)_2 \cdot 6H_2O$) (99%, Merck), sodium carbonate (Na_2CO_3) (Analytical Grade, Merck), [4-[[(4-dimethylamino)phenyl]-azo] benzenesulfonic acidsodium salt], methyl orange (Merck), titanium tetraisopropoxide (98%, Aldrich), acetic acid (96%, Merck) and salicylic acid were used as provided by the suppliers without further purification. Deionized water, purified with an Elga-Pure Water Purification (UHQ II) system, was used for preparing solutions in the experiments.

3.1.1. Methyl Orange

In industrial wastewater, dye stuffs and effluents are the major constituents of pollutans [81]. Azo dyes are an abundant class of synthetic, colored and organic compounds which are characterized by the presence of one or more azo bonds (-N=N-) [82]. Large quantities of these dyes are manufactured worldwide and used in a variety of applications. The discharging of azo dyes into water introduces intensive color and toxicity to aquatic systems. Azo dyes can be readily reduced under anaerobic conditions to aromatic amines which are potentially carcinogenic. Therefore, the removal of azo dyes from water is an important issue. Due to the complicated aromatic structures and chemical stability of azo dyes, conventional treatment methods either are ineffective in removing them from wastewater, or they can only transfer them to another phase, causing secondary pollution [83]. Hence, the development of more powerful water treatment technology such as the heterogeneous photocatalysis is necessary for the detoxification of azo dyes in. Methyl orange is a well-known azo dye (Figure 3.1). Its structure is also characterized by sulfonic groups, which are responsible for the high solubility of these dyes in water. The UV-Vis (Shimadzu UV-1600) spectrum of methyl orange shows two absorption maxima; the first band at 278 nm and a more intense second band at 464 nm (Figure 3.2).

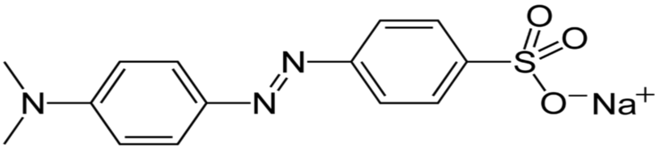

Figure 3.1. Chemical structure of methyl orange.

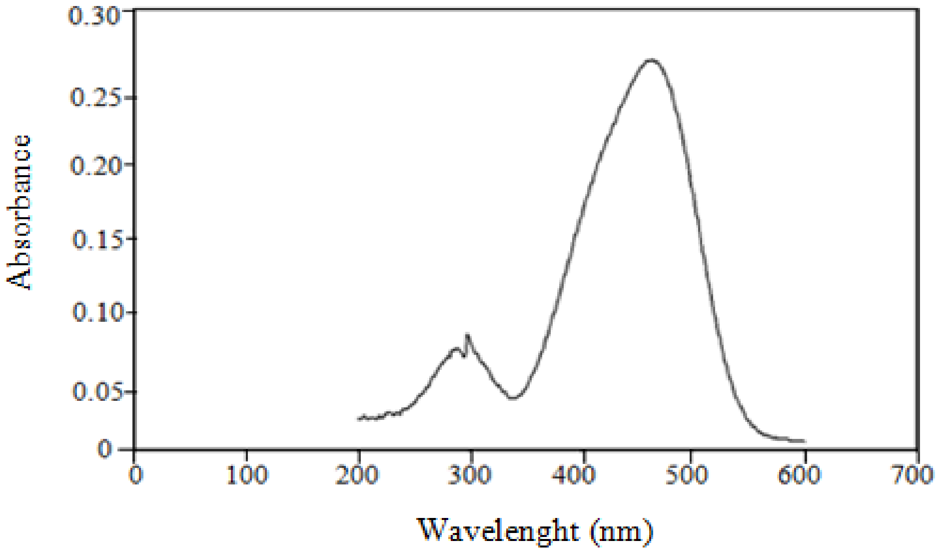

Figure 3.2. UV-vis spectra of MO.

3.1.2 Salicylic Acid

Salicylic acid (SA), also known as 2-hydroxybenzoic acid (Figure 3.3), is a white acicular crystalline powder. It is produced synthetically by heating sodium phenolyate with carbon dioxide under pressure and the oxidation of naphthalene [84]. SA is a key additive in many creams, gels and dermal patches. SA is also found commonly in dyes as a chemical. However, salicylic acid is easy to sublimate and can evaporate along with the steam, which destroys the environment and impairs people’s health. Wastewater containing salicylic acid originates mainly from the synthesis of salicylic acid and its derivatives and from the rinsing of medical and cosmetic manufacture equipment. Therefore it requires degradation to non-toxic substituents. Salicylic acid shows an absorption maxima at 296 nm, which indicates to the aromatic structure of the compound (Figure 3.4).

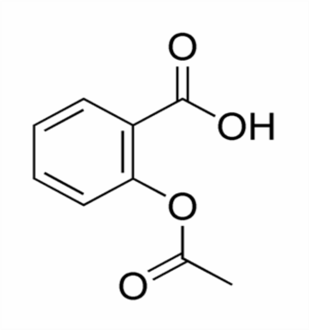

Figure 3.3. Chemical structure of salicylic acid.

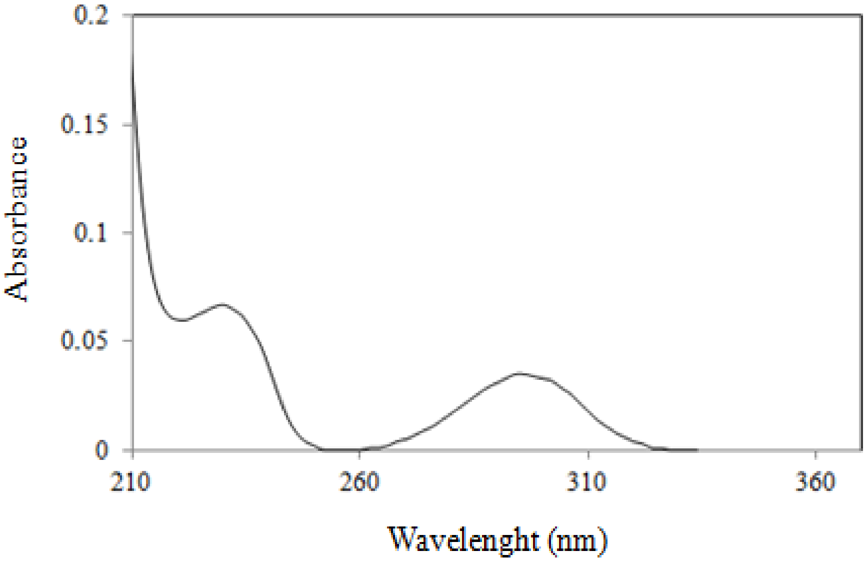

Figure 3.4. UV-vis spectra of salicylic acid.

3.2. Preparation of Catalysts

The nanocrystalline TiO_2 powders were prepared from the precursors of titanium tetraisopropoxide ($Ti(OC_3H_7)_4$) and acetic acid (CH_3COOH) via sol-gel synthesis [85].

$$2\,(Ti(OC_3H_7)_4) + 2\,AcOH \rightarrow Ti_2(OC_3H_7)_6(OAc)_2 + 2C_3H_7OH \qquad (3.1)$$

The preparation method of bare TiO_2 and supported catalysts was briefly as follows: 20 mL of titanium tetraisopropoxide was added gradually to 80 wt% acetic acid solution under continuous stirring for 2 h at 50^{o}C to produce a transparent sol. Depending on the loading of TiO_2 on the support, requisite amount of titania-sol was added to the aqueous suspension of the FA (initially 2 g in water for 2 h with a natural pH value of 12). After agitation and extensive washings, the catalysts were dried at 100^oC for 12 h. The calcination process was carried out in a muffle furnace using ambient air and 500^oC with a heating rate of $10^oC/min$. The obtained supported catalysts were ground into fine powders and named as 10% TiO_2-FA, 25% TiO_2-FA and 50% TiO_2-FA. 25% TiO_2 was also prepared by using the above procedure in the absence of the support.

For the preparation of ZnO nanoparticles, a co-precipitation method was applied [86]. Certain concentrations of zinc nitrate hexahydrate ($Zn(NO_3)_2{\cdot}6H_2O$) and sodium carbonate (Na_2CO_3) were used as precursors.

$$Zn(NO_3)_2{\cdot}6H_2O + Na_2CO_3 \rightarrow ZnCO_3 + 2NaNO_3 + 6H_2O \qquad (3.2)$$

($Zn(NO_3)_2{\cdot}6H_2O$) dissolved in 100 mL deionized water was added slowly into a 100-mL (Na_2CO_3) solution and mixed for 2 h at room temperature. The supported catalysts were prepared by the addition of 200-mL white solution into the 2 g raw FA saturated with deionized water. After stirring the suspensions, and centrifuging and washing them extensively, the catalysts were dried at 100^oC for 12 h and calcinated at 500^oC for 12 h. Finally the catalysts were ground and hereafter labeled as 0.125 M ZnO-FA, 0.25 M ZnO-FA, 0.5 M ZnO-FA. Bare ZnO was also prepared by using the above procedure in the absence of the support. All catalysts were stored in the dark.

3.3. Analysis

3.3.1. Characterization Techniques

Different analytical methods were used to determine of the structural features of the raw FA and the supported catalysts. X-ray diffraction (XRD) technique was used to identify the crystal structure of the synthesized supported catalysts. XRD patterns were obtained with Rigaku-D/MAX Ultima diffractometer with Cu Kα radiation (λ =1.54 Å) operating at 40 kV and 40 mA and scanning rate 2 min^{-1}.

The surface morphologies of the catalysts were determined using SEM in combination with EDX analysis on an ESEM-FEG/EDAX Philips XL-30 instrument operating at 20 kV using catalyst powders supported on carbon tape.

The BET (Brunauner–Emmet–Teller) isotherms were obtained at liquid nitrogen temperature 77 K by using Quantachrome Nova 2200e automated gas adsorption system. The specific surface areas were determined using multi-point BET analysis and the pores sizes were measured by the BJH method of adsorption.

The UV-Vis DRS of the catalysts were recorded on a Shimadzu UV-2450, equipped with an integrating sphere reflectance accessory. The baseline correction was done by $BaSO_4$. The analysis range was from 200 to 600 nm for all catalysts.

3.3.2. Photocatalytic Experiments

The photocatalytic performances of the catalysts were examined in laboratory constructed irradiation boxes.

For the experiments under UV irradiation, the first irradiation box was equipped with eight black fluorescent lamps (Philips TL 15 W/5 BLB) that supply light of wavelength 320-440 nm (with a maximum emission at 365 nm) (Figure 3.5). The incident photon flux for all lamps was measured as 4.7×10^{15} photon/s using potassium ferrioxalate ectinometer in the previous experiments [87]. In the experiments, a pyrex erlenmeyer flask was used as a reactor with an inlet for circulation of air and outlet for the collection of aliquots. Air circulation was supplied by using a pump. The connection between the pump and the flask were made with Tygon tubing. The lamps were positioned to surround the flask from two sides. A fan was placed at one end of the box in order to eliminate the heating effect of the lamps. Prior to illumination, to ensure the equilibrium of adsorption process, suspensions were magnetically stirred in the dark for 30 min (for TiO_2-FA catalysts) and for 2 min (for ZnO-FA catalysts). All experiments were performed in continuous circulation mode at room temperature and at pH=8 (3.27 mg/L MO in the presence of 0.25M ZnO-FA) or pH=8.5 (3.27 mg/L MO in the presence of 25% TiO_2-FA) without concerning the degradation intermediates. Also, measurements were conducted at least twice and the average value was recorded. Aliquots (about 5 mL) were retrieved from the flask-outlet at certain time intervals and analyzed after filtering through Millipore filters (0.45 μm for TiO_2-FA catalysts and 0.22 μm for ZnO-FA catalysts). UV-Vis Spectrophotometer (Shimadzu 2450) was used to monitor the absorbance spectra of MO as a function of illumination time. The absorbance at 278 nm represented the aromatic content of MO and the decrease of the band at this wavelength indicated degradation of MO's aromatic moiety. The absorbance at 464 nm was due to the color of MO solution and it was used to examine the decolorization of MO solution.

Figure 3.5. Irradiation box for the experiments under UV irradiation.

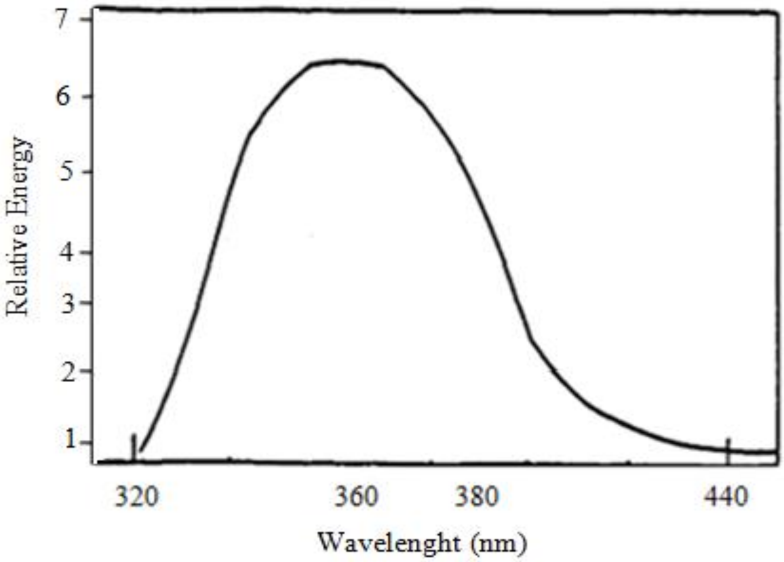

Figure 3.6. Emission spectrum of a fluorescent lamp used in the UV-irradiation box.

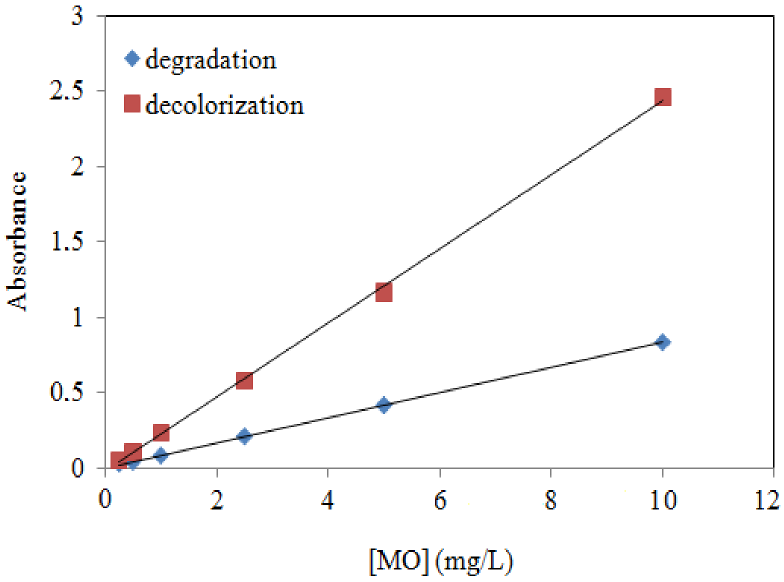

Figure 3.7. Calibration plots of MO at 278 nm (degradation) and 464 nm (decolorization).

The second irradiation box was used to control the visible light activities of the catalysts for the degradation of SA as the probe molecule with no absorption band in the visible region (λ > 400 nm). All experiments were performed in a gas recycling reactor. The reactor consisted of a 36.2 cm-long Pyrex tube with an inner diameter of 3.5 cm. To allow temperature regulation via water circulation, there was a sealed inner glass tube in the reactor with thickness of 2 cm. The catalyst suspensions were contained in the annulus formed between the two tubes. The gas above the suspension was pumped using a pump. A sintered glass disk, placed at the bottom of the reactor, provided circulation of air and prevented settlement of the suspension. The reactor was located in the irradiation box containing six commercial white lamps with light of wavelength 450-600 nm (Philips TL 20W/52). The lamps were positioned to surround the reactor from three sides. The front side of the box was designed to operate as a door with the reactor attached. This maintained a uniform geometry throughout experiments. A fan was placed at the top of the box and air was also circulated through the box in order to eliminate heating effects of the lamps. Prior to vis light irradiation, the suspensions were magnetically stirred in the dark for 30 min for both TiO_2-FA and ZnO-FA catalysts. All experiments were performed at room temperature and at the natural pH of SA solution (pH=6.5). Aliquots (about 5 mL) were retrieved from the flask-outlet at certain time intervals and analyzed after filtering through Millipore filter (0.45 μm for TiO_2-FA catalysts and 0.22 μm for ZnO-FA catalysts). For all experiments, the initial concentration of SA was 1.38 mg/L (1x10^{-5} M). The residual amount in the aqueous phase was measured by using Shimadzu 2450-UV-Vis Spectrophotometer following the progressive decrease in the 296 nm peak.

Figure 3.8. Irradiation box for the experiments under visible light irradiation.

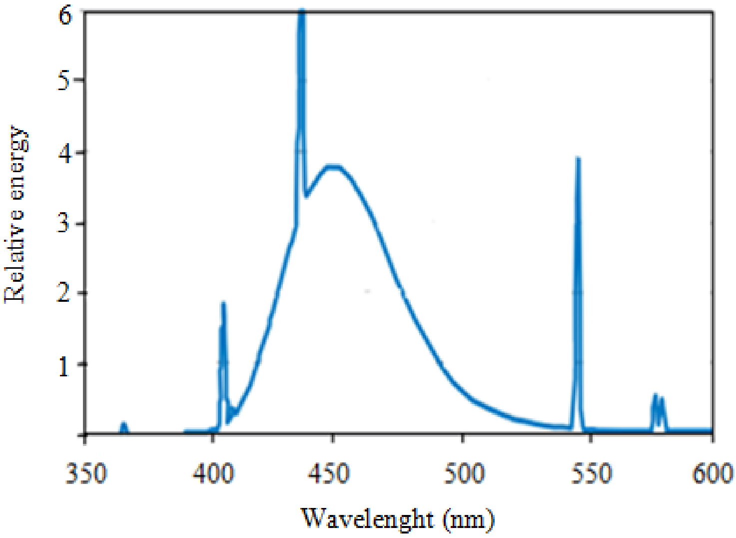

Figure 3.9. Emission spectrum of a fluorescent lamp used in the Vis-irradiation box.

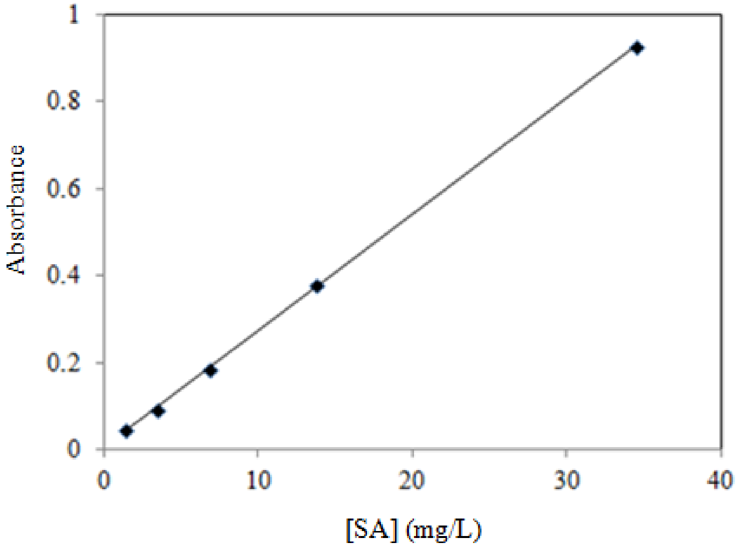

Figure 3.10. Calibration plot for SA at 296 nm.

3.3.3. Kinetic Study

3.3.3.1. Dark Adsorption Kinetics. Adsorption kinetic experiments were investigated to study adsorption details of the MO on 25% TiO_2-FA and 0.5M ZnO-FA catalysts. The amount of MO adsorbed per gram of adsorbent (25% TiO_2-FA or 0.5M ZnO-FA) at time t (min) (q_t) can be found by the following equation [88]

$$q_t = \frac{(C_0 - C_t)V}{m} \tag{3.3}$$

where C_0 was the initial concentration of MO in solution, C_t was the concentration of MO at time t, V was the volume of the solution and m was the mass of catalyst used. In case C_t was replaced with C_e (concentration of MO at equilibrium), q_e could be found as the amount of adsorbed MO molecule per gram of adsorbent at equilibrium.

To further understand the adsorption kinetics, the well-known adsorption equations of pseudo first order and pseudo-second order models were applied to our catalyst systems. The pseudo-first order equation was given by the following equation

$$\frac{dq_t}{dt}=k_1(q_e\text{-}q_t) \tag{3.4}$$

where k_1 was the pseudo-first order rate constant. After the integration of the Equation 3.4 by using the integral limits of q_t= 0 at t= 0 and q_t= q_t at t= t,

$$\ln (q_e – q_t) = \ln q_e – k_1t. \tag{3.5}$$

was obtained. The plot of ln (q_e-q_t) versus t gave a straight line with correlation coeffients. The rate constant (k_1) was calculated from the slope of this line.

The pseudo-second-order model was expressed as follows

$$\frac{dq_t}{d_t}=k_2(qe-qt)^2. \tag{3.6}$$

After the integration of the equation by the integral limits of q_t=0 at t=0 and q_t=q_t at t=t, Equation 3.6 became

$$\frac{t}{q_t}=\left(\frac{1}{k_2q_e^2}\right)+\frac{t}{q_e}. \tag{3.7}$$

The linearity obtained in the plot of t/q_t versus t resulted in correlation coefficients for decolorization and degradation experiments.

<u>3.3.3.2. Adsorption Isotherms.</u> Freundlich and Langmuir isotherm models were applied as the most studied isotherm models for our catalyst systems. The Freundlich isotherm, the earliest known relationship describing the adsorption process, was an empirical equation employed to describe heterogeneous systems. Its application suggested that adsorption energy exponentially decreased on completion of the sorptional centers of an adsorbent. The linearized form of the Freundlich isotherm was given in the following equation [89,90].

$$\ln q_e = \ln K_F + b_F \ln C_e \tag{3.8}$$

where K_F was the Freundlich constant, b_F was the adsorption intensity constant and C_e was the concentration of the MO at equilibrium.

According to Langmuir theory, it assumed that the adsorption occurred at a specific homogeneous site within adsorbent, all sites were equivalent, and there were no interactions between adsorbate molecules [91]. The linearized Langmuir equation was given in Equation 3.9

$$\frac{C_e}{q_e} = \frac{C_e}{q_{max}} + \frac{1}{q_{max} K_L} \tag{3.9}$$

where q_{max} was the maximum capacity of the adsorbent and K_L was the Langmuir adsorption constant.

3.3.3.3. Kinetic Studies for the Experiments Followed Under UV Irradiation. For these studies, initial MO concentrations were varied in range of 3.27 mg/L to 32.27 mg/L. Pseudo-first order kinetics were followed based on the following rate equation (Equation 3.10),

$$R = \frac{dC}{dt} = kC \tag{3.10}$$

where R was the rate of degradation reaction, C was the concentration of MO molecule at time t and k was the rate constant. The equation could be simplified by integration as

$$\ln \frac{C_0}{C} = kt \tag{3.11}$$

where C_0 was taken as the equilibrium concentration of the MO after dark adsorption.

The kinetics of the photocatalytic degradation processes was also analyzed by using Langmuir-Hinshelwood model. This model was rationalized for the experimental results by the following equation:

$$R = \frac{k_r K C_t}{1+KC_t} = k_{app}\,C_t \tag{3.12}$$

where R was the rate of degradation reaction, k_{app} apparent first order rate constant, C_t was the remaining concentration of MO in solution by time, t was the time of reaction, K was adsorption coefficient of MO on the supported catalyst and k_r was the reaction constant. From the Equation 3.12, the rate (R) could be written as

$$\frac{1}{\text{Rate}} = \frac{1+KC_t}{k_r K C_t} \tag{3.13}$$

This equation could be arranged as

$$\frac{1}{k_{app}\,C_t} = \frac{KC_t}{KC_t k_r} + \frac{1}{k_r C_t K} \tag{3.14}$$

Finally, the Equation 3.15 was obtained by substitution of C_0 in place of C_t as the equilibrium concentration of MO molecule after dark adsorption.

$$\frac{1}{R} = \frac{1}{k_{app}\,C_0} = \frac{1}{k_r K C_0} + \frac{1}{k_r} \tag{3.15}$$

4. RESULTS and DISCUSSION

4.1. Characterization Results of TiO_2-FA Catalysts

4.1.1. XRD Analysis

XRD analysis was used to assess the crystallinity of the TiO_2 particles. The characteristic TiO_2 anatase diffraction of (101) was detected at 25.4^o (2θ) in the pattern of the 25% TiO_2 (Figure 4.1). Other anatase reflections of (004), (200), (105), and (211) also appeared at 37.2, 48.2, 54.2, 55.3^o (2θ), respectively. Figure 4.2 presented XRD patterns of the raw support (FA) and supported catalysts. FA was mainly composed of amorphous aluminosilicate glass and five crystalline mineral phases; namely quartz (SiO_2), calcite ($CaCO_3$), mullite ($Al_2O_3.2SiO_3$), lime (CaO) and magnetite (Fe_3O_4). The respective diffractions were noticed at low-angle ($2\theta < 10^o$) and also high-angle ($20^o < 2\theta < 60^o$) ranges (Figure 4.2A). The supported catalysts revealed (101), (004), (200), (105), and (211) anatase peaks at 25.4, 37.2, 48.2, 54.2, 55.3^o (2θ) (Figure 4.2 B-D). Rutile phase was not detected in the crystalline structure of the 25% TiO_2 and the supported catalysts, as evidenced by the absence of 27.4^o (2θ) peak. TiO_2 reflections were more clearly observed in the patterns of 25% TiO_2-FA and 40% TiO_2-FA catalysts. However, signals were not intensified in the presence of 40% TiO_2-FA, indicating a kind of saturation effect at 25% TiO_2 loading. The crystalline sizes of TiO_2 ($D_{anatase}$) were calculated from (101) peak broadening by using Scherrer's equation as 17 nm, 15 nm and 18 nm for the 25% TiO_2, 25% TiO_2-FA and for 40% TiO_2-FA, respectively (equation 2.10). There seems to be no significant variation in the TiO_2 crystalline sizes. Meanwhile, intensities of the FA peaks became weaker with the TiO_2 loading. This may suggest dispersion of the TiO_2 nanoparticles throughout the surface and bulk of the support.

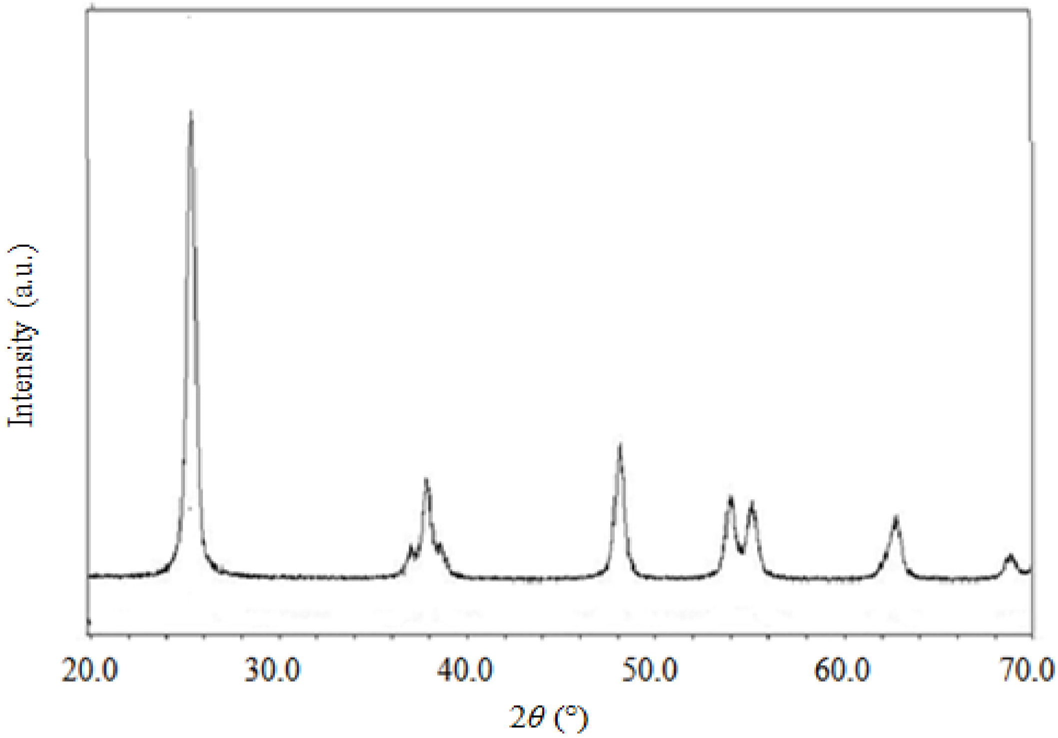

Figure 4.1. XRD patterns of 25%TiO_2.

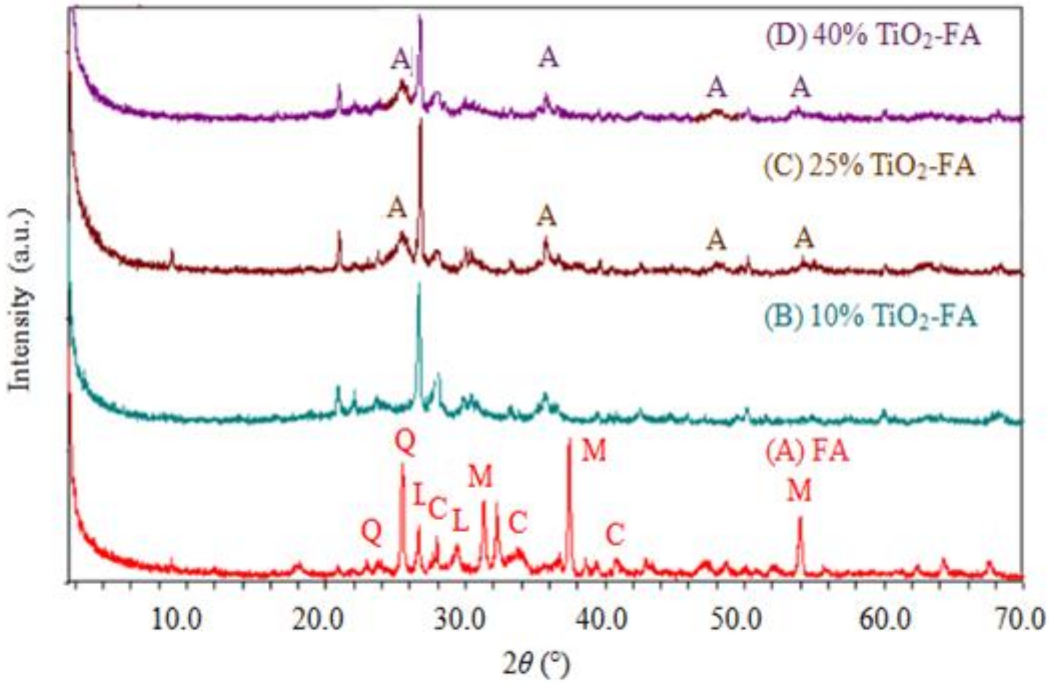

Figure 4.2. XRD patterns of FA and supported catalysts. (A: anatase, Q: quartz, M: mullite, C: calcite)

4.1.2. SEM (EDX) and Elemental Mapping Analysis

Structural morphologies of the 25% TiO_2, FA, and 40%TiO_2-FA were investigated by SEM analysis. The image of 25% TiO_2 showed uniformly distributed corn-shaped nanoparticles (Figure 4.3). According to the EDX analysis, 67.2 wt % Ti and 32.8 wt % O were found over the whole surface of 25% TiO_2 catalyst. The FA illustrated two types of clusters; spherical and non-shaped aggregates (Figure 4.4). The spherical ones had cavities and air holes (cenospheres) on the outer surface. The non-shaped aggregates were either existed on the spherical particles or heterogeneously dispersed over the matrix. The EDX analysis reported Si, Al and Ca as major and Mg and Fe as minor constituents of the FA (Table 4.1). Only 0.06 wt % Ti was also found within the FA structure. For the 40% TiO_2-FA catalyst, two images were exhibited to demonstrate the retained spherical and non-shaped morphology of the support (Figure 4.5 ‘A’, Figure 4.6 ‘A’). Formation of smooth layers on top of the spheres and aggregates was noticed. The EDX-spot analysis showed significant increments in the Ti percentages; 27.2% Ti was found on the surface of the sphere and 53.3% Ti was detected on the non-shaped aggregate. The higher percentages of Ti was also verified in the mapping images of the 40%TiO_2-FA catalyst, where Ti signals were dominated on top of the sphere and also on the bright-edged agglomerate (Figure 4.5 ‘F’, Figure 4.6 ‘F’).

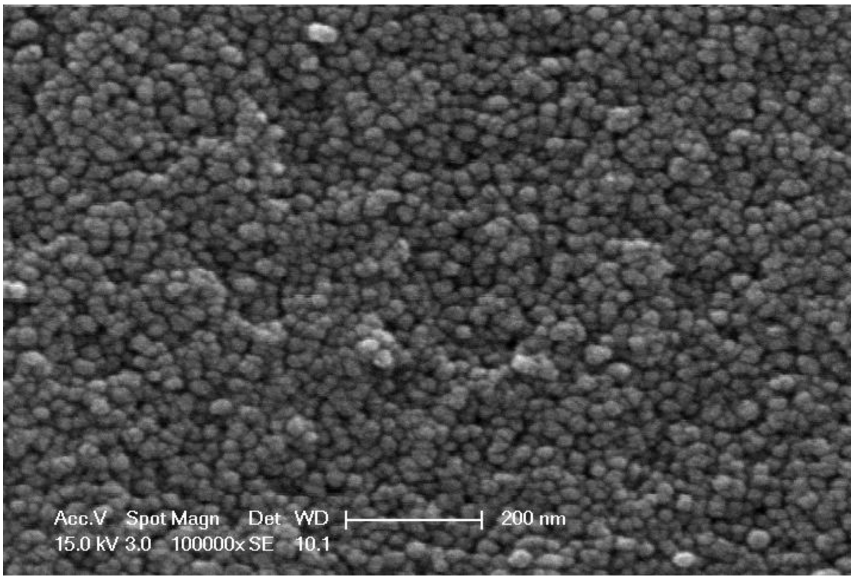

Figure 4.3. SEM image of 25% TiO_2.

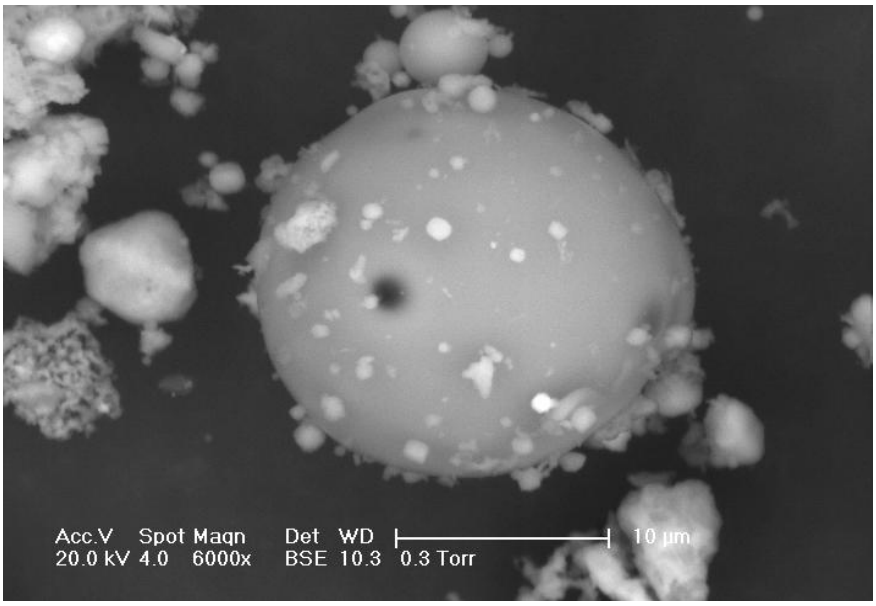

Figure 4.4. SEM image of raw FA.

Table 4.1. Elemental composition analysis of the raw FA, 40% TiO_2-FA sphere and 40% TiO_2-FA aggregate.

FA		**40% TiO_2-FA sphere**[a]		**40% TiO_2-FA aggregate**[b]	
Components	**Wt %**	**Components**	**Wt %**	**Components**	**Wt %**
Si	50.03	Si	24.05	Si	20.32
Al	20.47	Al	23.79	Al	14.56
Ca	14.06	Ca	5.18	Ca	2.56
O	10.47	O	16.28	O	6.20
Fe	4.94	Fe	3.45	Fe	3.02
Ti	0.06	Ti	27.25	Ti	53.34

[a]: SEM image was given in Figure 4.5 A.

[b]: SEM image was given in Figure 4.5 B.

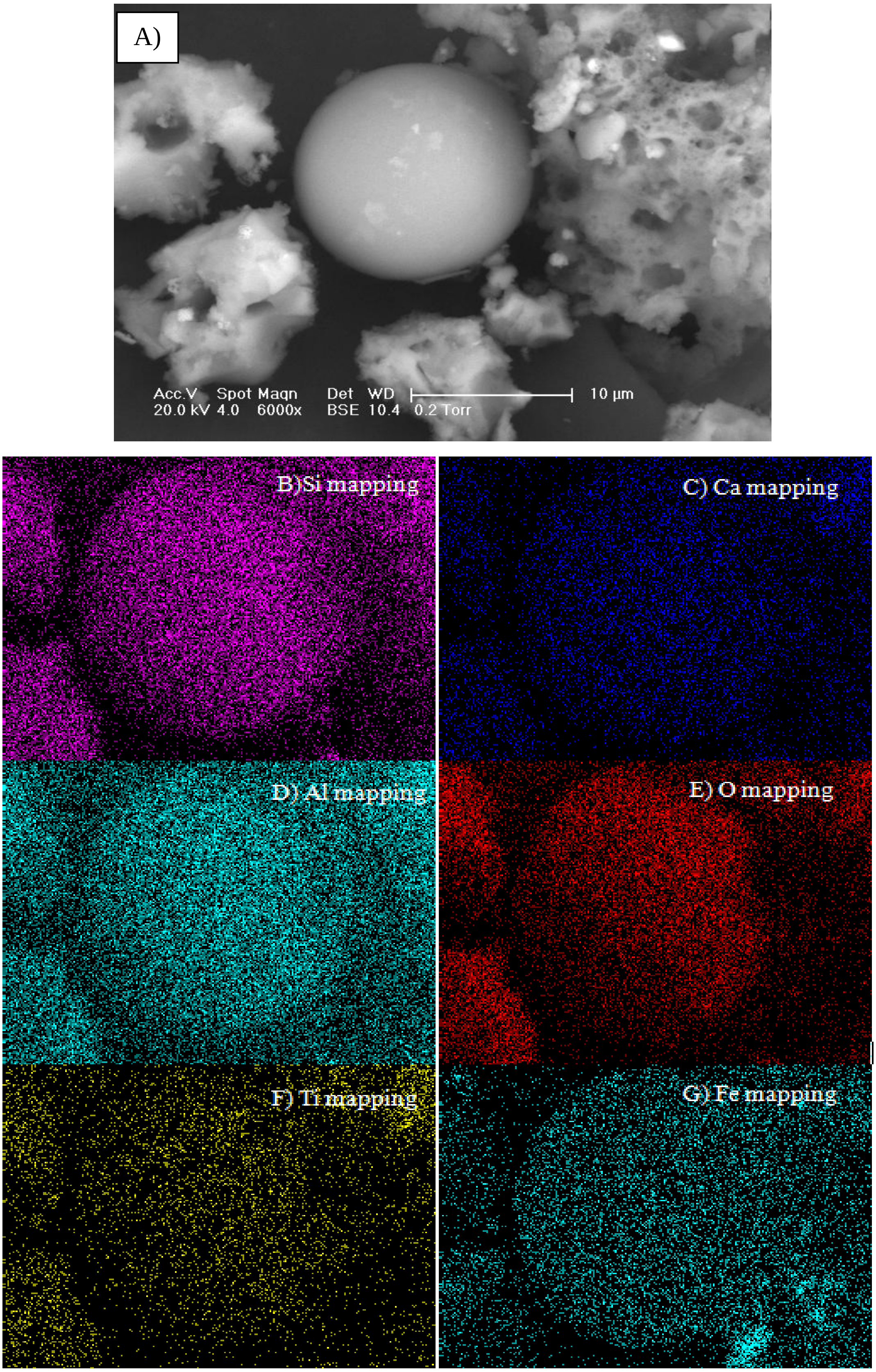

Figure 4.5. SEM and mapping images of 40% TiO_2-FA (A),Si, Ca, Al, O, Ti and Fe (B-G).

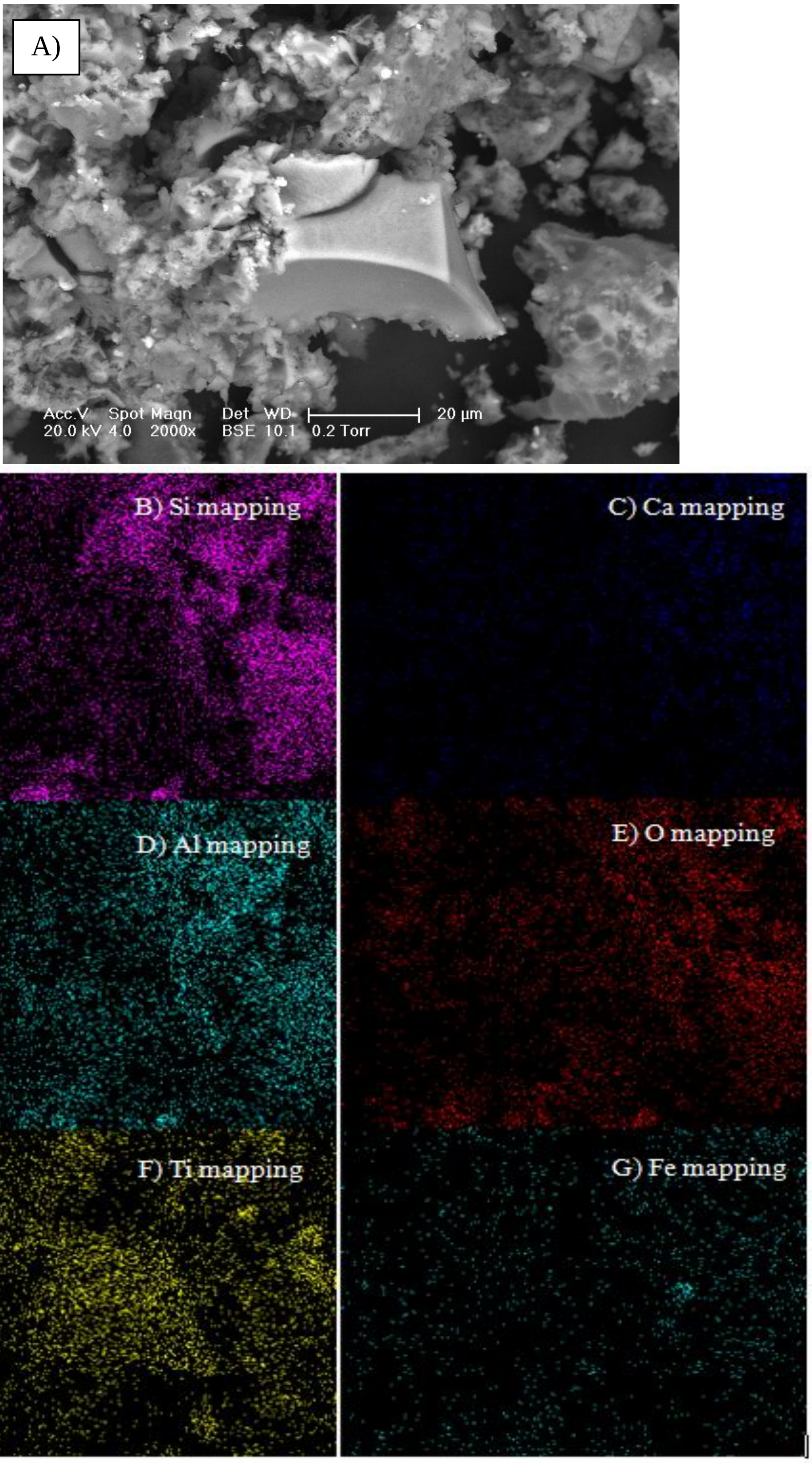

Figure 4.6. SEM and mapping images of 40% TiO_2-FA (A),Si, Ca, Al, O, Ti and Fe (B-G).

4.1.3. Nitrogen Adsorption-Desorption Isotherms

Nitrogen adsorption-desorption tests were carried out for the FA and supported catalysts (Figure 4.7). The FA exhibited Type II isotherm, specific of non-porous materials [92]. For the supported catalysts, Type IV isotherms were obtained due to the formation of mesopores [93]. The loading percentage of TiO_2 has an effect in the generation of these mesopores. The increments in the percentages created more mesopores, evidenced by the enlargement in the hysteresis loops [94]. The pore size distribution curves displayed that the pores of the supported catalysts existed in the typical mesoporous region of 20-40 Å (Figure 4.8). The increase in the pores volumes also pointed out increments in the surface areas of the supported catalysts in comparison to the FA (Table 4.2). In the line of these results, formation of more adsorption sites and hence degradation ability were expected for the supported catalysts.

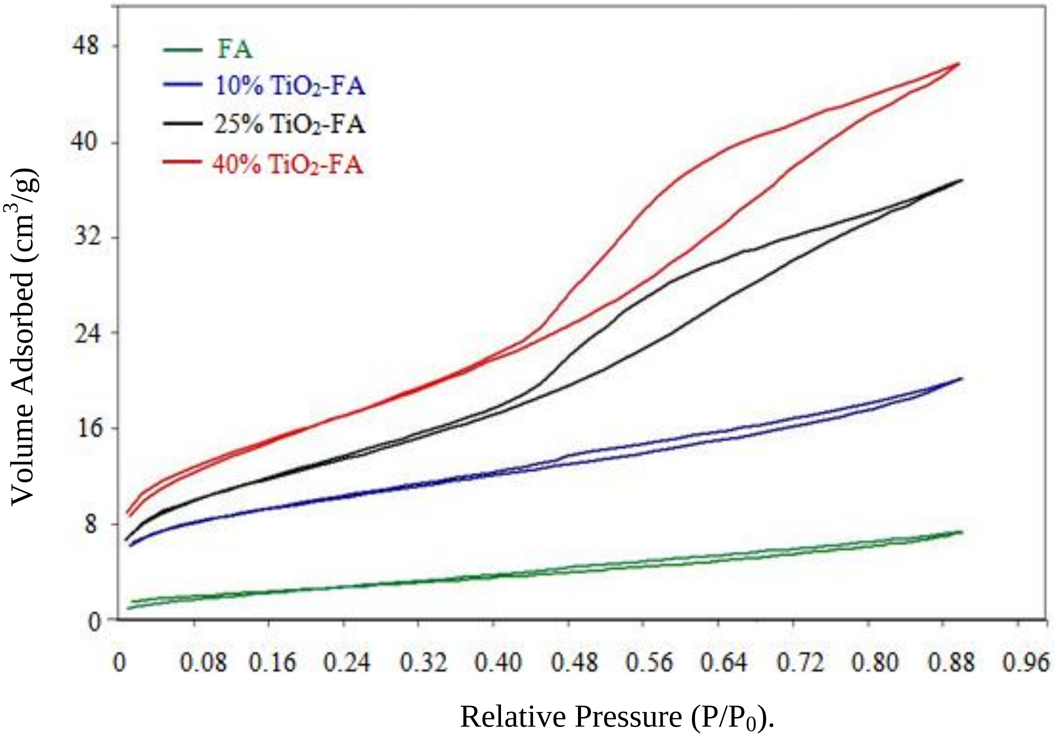

Figure 4.7. Nitrogen adsorption-desorption isotherms of FA and supported catalysts.

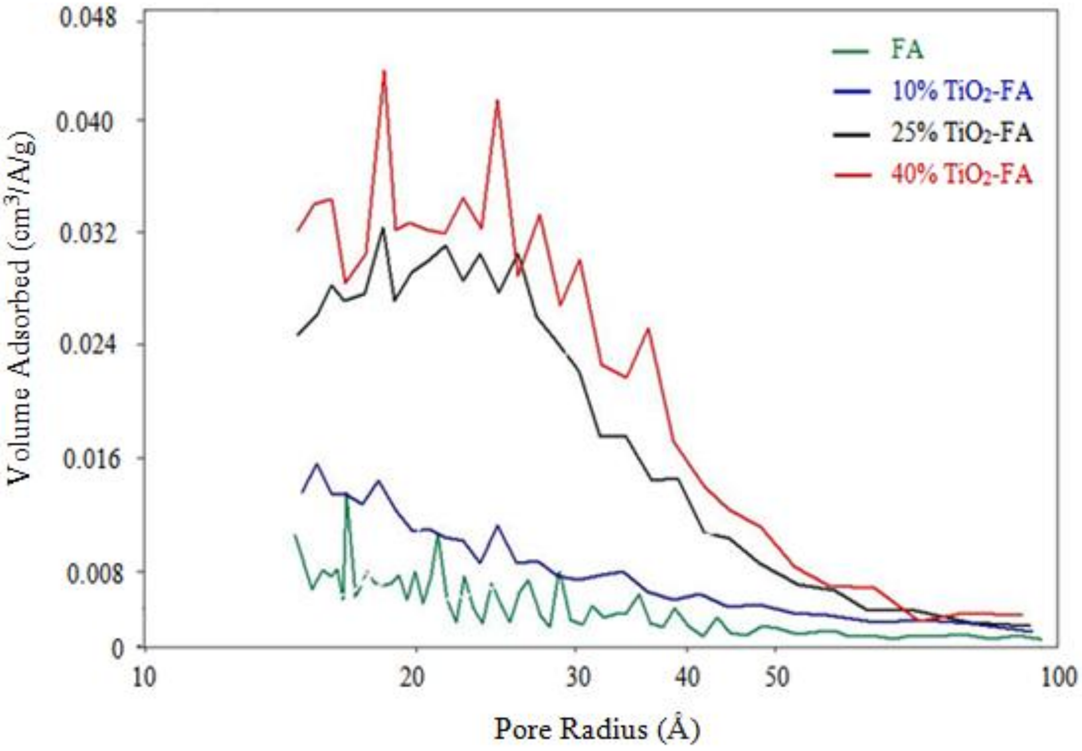

Figure 4.8. Pore size distribution plots of FA and supported catalysts.

Table 4.2. Surface area (BET) and pore volume (V_{pore}) values of raw FA, 25% TiO_2 and supported catalysts.

Materials	**BET (m^2/g)**	**V_{pore} (cm^3/g)**
FA	5.61	0.009
25% TiO_2	40.11	0.011
10% TiO_2-FA	15.97	0.019
25% TiO_2-FA	29.64	0.048
40% TiO_2-FA	37.84	0.061

4.1.4. UV-Vis DRS Analysis

UV-vis absorption profiles of the FA, 25% TiO_2 and the supported catalysts were presented in the Figure 4.9. The raw FA showed an extending absorption tail in between

200-600 nm. The characteristic absorption edge of TiO_2 was not observed in the supported catalysts even with 40% TiO_2 loading. Instead, profiles of the supported catalysts were mostly similar to the absorption spectra of the FA or a little higher than the sum of the absorbances of FA and 25% TiO_2. Thus, the extension to the longer wavelengths did not create a considerable alteration in the crystal structure of TiO_2 (within supported catalyst matrix) to prove the visible light activity.

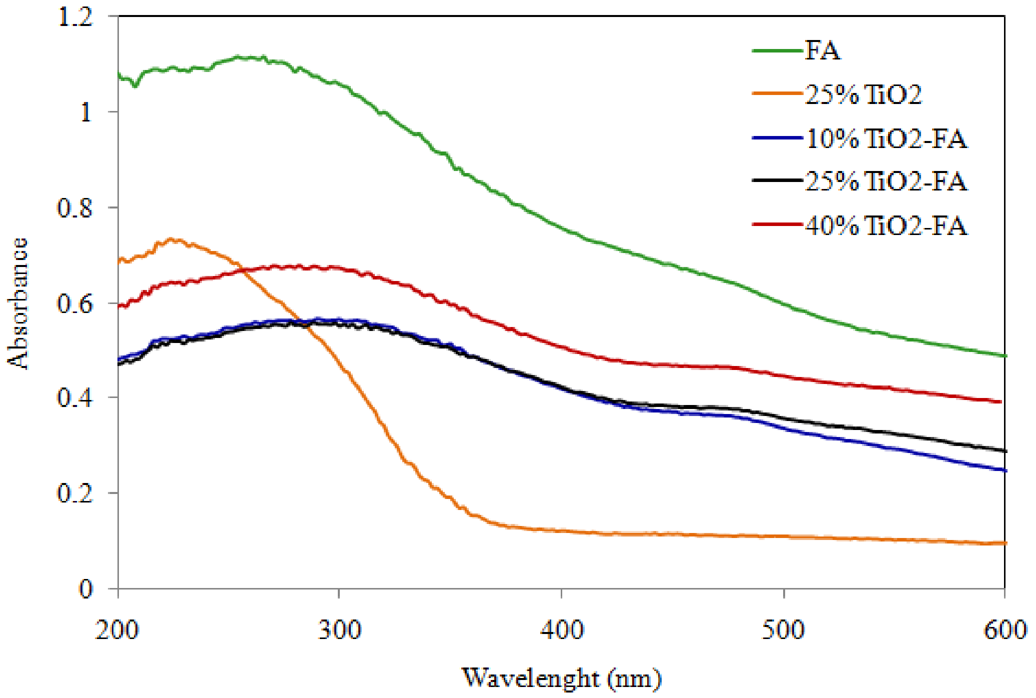

Figure 4.9. UV-vis DRS spectra of the raw FA, 25% TiO_2 and supported catalysts.

4.2. Degradation Results of TiO_2-FA catalysts

4.2.1. Control Experiments

Prior to the details of dark adsorption and photocatalytic degradation experiments, two sets of control experiments were performed. In the first part, adsorption capacities of the raw support (FA) and the as-prepared catalysts (25% TiO_2 and 25% TiO_2-FA) were investigated in the dark (Figure 4.10). In the second part, photolysis of MO (Figure 4.11 inset) and photocatalytic activities of the 25%TiO_2 and 25% TiO_2-FA catalysts were controlled under UV irradiation (Figure 4.11). Results of experiments performed in the dark were shown in Figure 3.11. MO amount remaining in the solution was found as 2.98 mg/L in the presence of only FA. However, 25% TiO_2-FA exhibited lower MO concentration, demonstrating a better adsorption capacity in comparison to the support. After 30 min mixing in the dark, no significant change in the MO concentration was noticed. The morphology of the catalyst was also investigated by an SEM analysis after dark adsorption experiment. The Ti percentage was found to lower (around 5%) in comparison to the percentages obtained in the structure of 25% TiO_2-FA (after preparation before the experiments) (Appendix A, Figure A.1). The color of MO was yellow and its natural pH in water was 5.85.

Accordingly, MO was negatively charged in water solution due to its pK_a value of 3.4 [95]. The alkaline character of FA converted the acidic pH of the MO to $pH_{FA+MO\ solution}$ =11. Thus, repulsive forces seem to be dominant among the FA surface and MO molecules (in the anionic form). However, heterogeneity on the surface of the FA, the existence of minor amounts of Fe_2O_3, TiO_2, ZnO within the structure and also the pores (though they have very restricted volumes) might create a kind of weak interaction with the MO molecules. This resulted in decolorization, however, due to the dominant grayish color of the FA could not be visualized, instead could be followed by the decrease in the absorption band at 464 nm. Moreover, the interaction might also vary the conjugation in the benzenic rings through the chromophore (-N=N-) and resulting in the limited decrement of the 278 nm band. For 25% TiO_2-FA, the pH of solution with 3.27 mg/L MO was 8.5, indicating a reduction in the alkalinity of the FA solution. As a consequence, alteration in the charge nature of the supported catalyst was expected with a stronger adsorption effect of TiO_2 nanoparticles. This might again induce damage within the localized conjugation of the MO skeleton being responsible from the decrease in the 278 nm peak during the dark period. Additionally, the higher surface area and the larger pore volume of the supported catalyst increased adsorption of MO and resulted in lower degradation amount in comparison to that of FA alone.

Under irradiation, a negligible degradation was observed in the absence of catalysts (Figure 4.11 inset). 25% TiO_2-FA exhibited a better activity than 25% TiO_2. This was in consistency with the improved dark adsorption capacity of the supported catalyst.

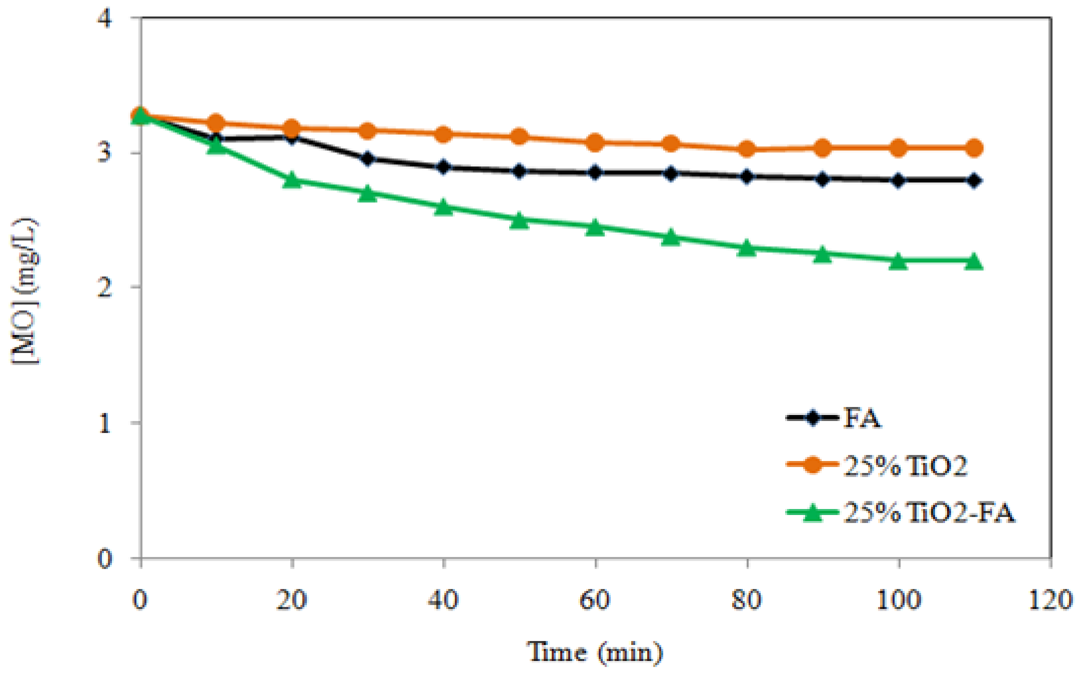

Figure 4.10. Control experiments in the dark. Conditions: pH: 5.85 (Natural), $[MO]_0$= 3.27 mg/L, T=298 K, Flow rate= 2000 rpm.

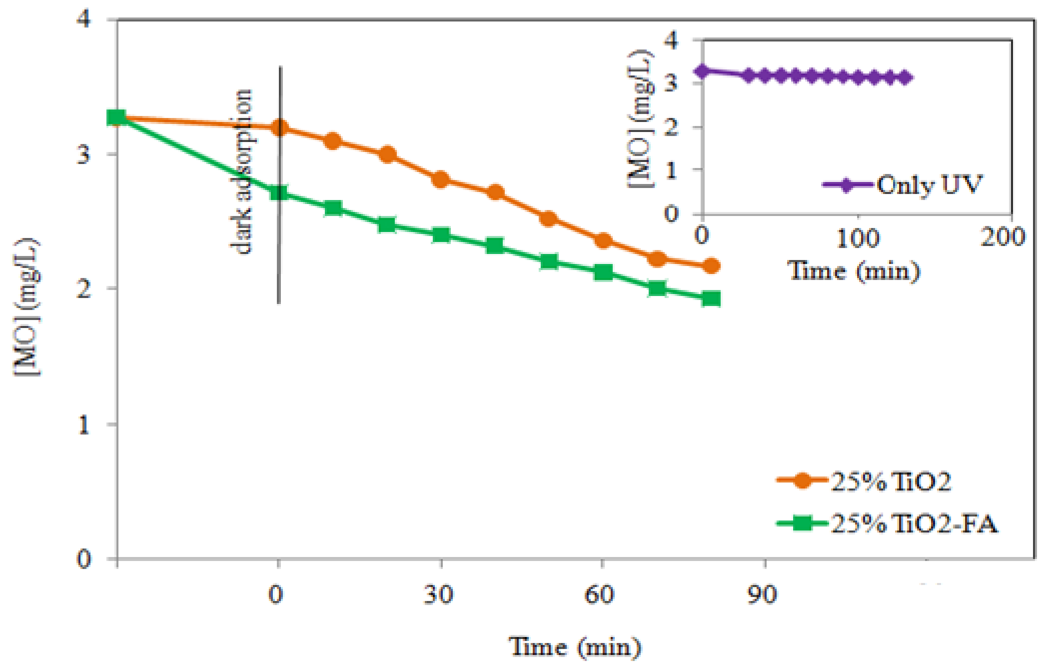

Figure 4.11. Control experiments under UV irradiation. Inset: Photolysis of MO Conditions: pH: 5.85 (Natural), [MO]0= 3.27 mg/L, I= 4.7x1015 photons/s, T=298 K, Flow rate= 2000 rpm.

4.2.2. Dark Adsorption Experiments

4.2.2.1. Adsorption Kinetics. Adsorption kinetic experiments investigated the dark adsorption details of MO (3.27 mg/L, 0.01 mmol/L) on the 25% TiO_2-FA catalyst.

According to the pseudo-first order model (Equation 3.4), the plot of ln (q_e-q_t) versus t gave straight lines with correlation coefficients of 0.7935 (for degradation) and 0.4034 (for decolorization) (Figure 4.12 and Figure 4.13).

Pseudo-second order model (Equation 3.6), however, resulted in bigger correlation coefficients in the plots of t/q_t versus t, 0.9674 and 0.9763 for degradation and decolorization experiments, respectively (Figure 4.14, Figure 4.15). Thus, the higher values of the coefficients indicated a better adsorption of MO on the supported nanocatalyst by using the pseudo-second order model while only a certain extent of adsorption seems to be possible by the application of the pseudo-first order model.

4.2.2.2. Adsorption Isotherms. Freundlich (Equation 3.8) and Langmuir (Equation 3.9) models were employed at five different initial concentrations of MO (16.3, 8.17, 4.91, 3.27 and 1.62 mg/L) in the presence of 25% TiO_2-FA. The line fittings of ln q_e versus ln C_e in Freundlich isotherms gave 0.9395 (for degradation) and 0.8149 (for decolorization) correlation coefficients, respectively (Figure 4.16, Figure 4.27).

Langmuir isotherms for both degradation and decolorization experiments were presented in Figure 4.18 and Figure 4.19. It was observed that the amount of MO adsorbed per gram of adsorbent (q_t) reached an equilibrium as a function of time t (min). The linearity obtained in the plots of C_e/q_e versus C_e for degradation and decolorization processes (based on Langmuir isotherms) resulted in 0.9653 and 0.9981 correlation coefficients, respectively (Figure 4.18 inset, Figure 4.19 inset). Since the higher coefficients were obtained with the application of the Langmuir model, a monolayer coverage was supposed for the adsorption of MO on the 25% TiO_2-FA catalyst. From the slope of the lines, Langmuir adsorption capacities were calculated as 0.015 mg/g and 1.24 mg/g for degradation and decolorization processes, respectively.

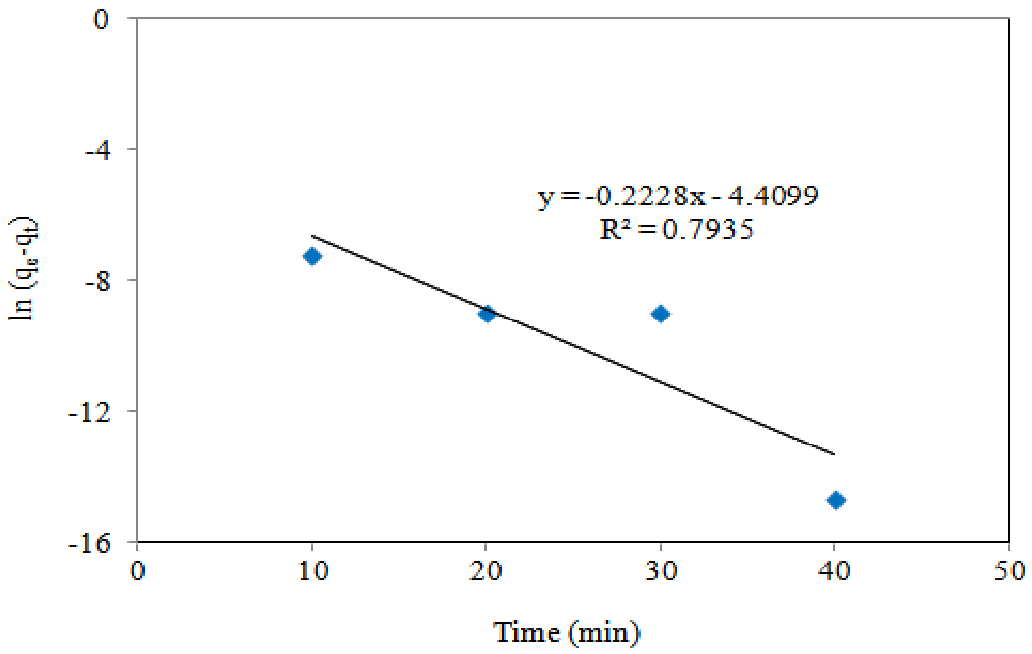

Figure 4.12. Pseudo-first order kinetics for the degradation of MO. Conditions: pH: 5.85 (Natural), $[MO]_0$= 3.27 mg/L, T=298 K, Flow rate= 2000 rpm.

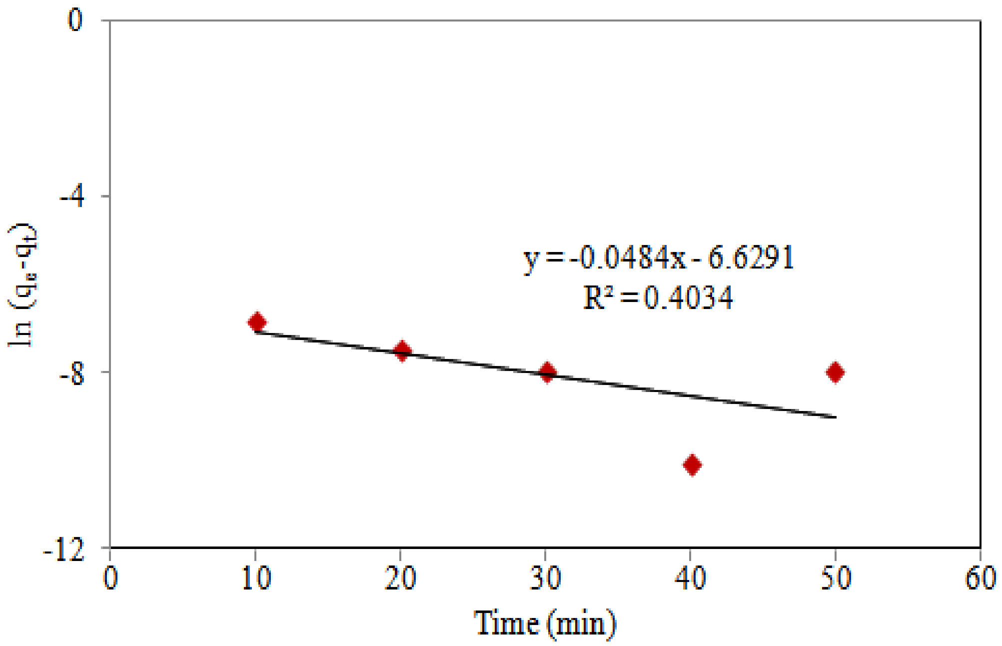

Figure 4.13. Pseudo-first order kinetics for the decolorization of MO. Conditions: pH: 5.85 (Natural), $[MO]_0$= 3.27 mg/L, T=298 K, Flow rate= 2000 rpm.

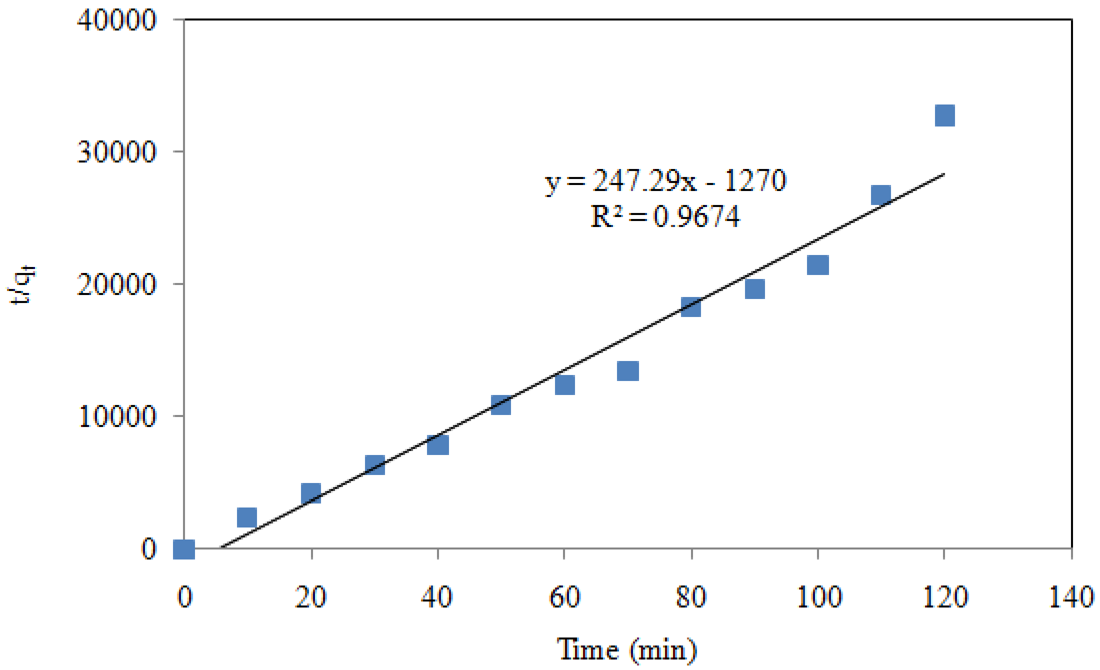

Figure 4.14. Pseudo-second order kinetics for the degradation of MO. Conditions: pH: 5.85 (Natural), $[MO]_0$= 3.27 mg/L, T=298 K, Flow rate= 2000 rpm.

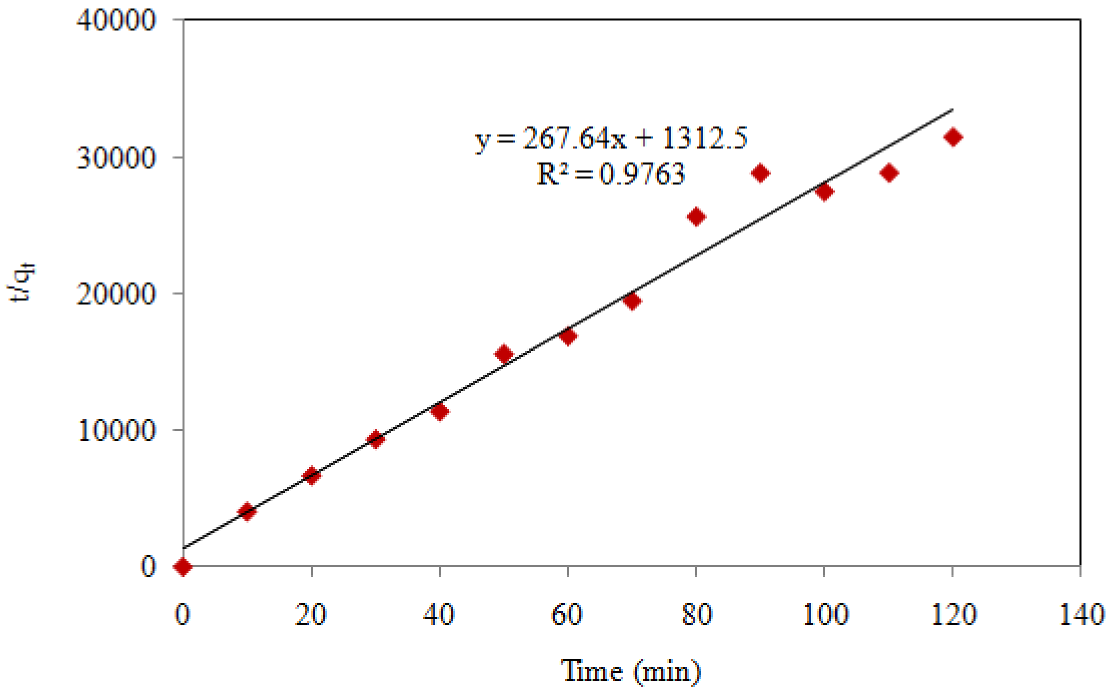

Figure 4.15. Pseudo-second order kinetics for decolorization of MO. Conditions: pH: 5.85 (Natural), $[MO]_0$= 3.27 mg/L, T=298 K, Flow rate= 2000 rpm.

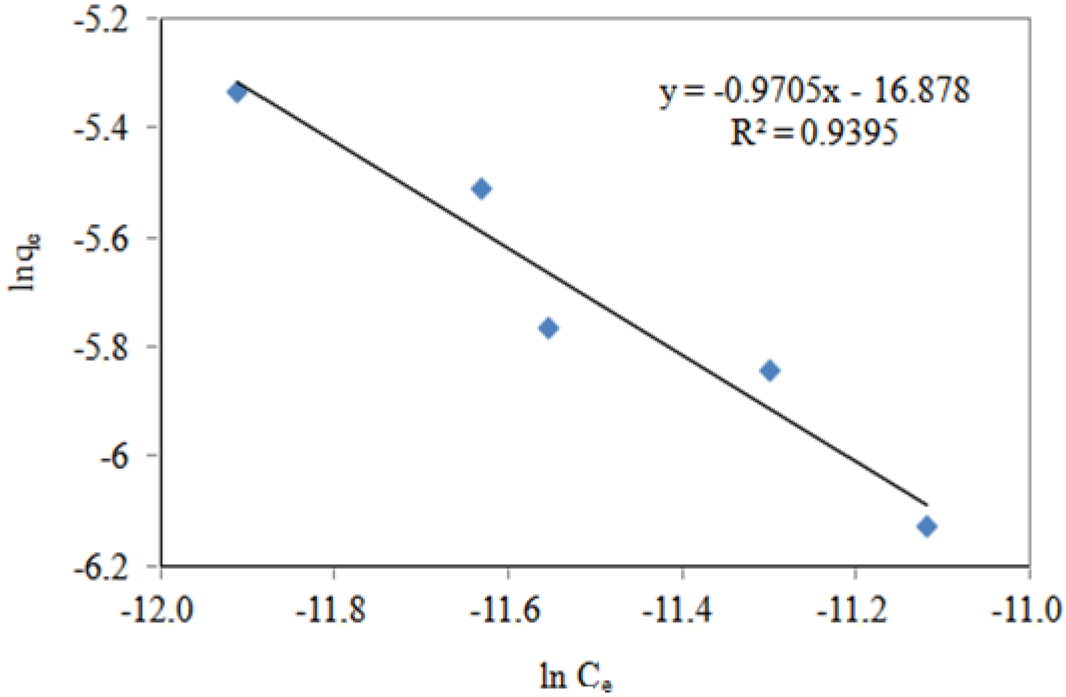

Figure 4.16. Freundlich adsorption isotherm for degradation of MO. Conditions: pH: 5.85 (Natural), T=298 K, Flow rate= 2000 rpm.

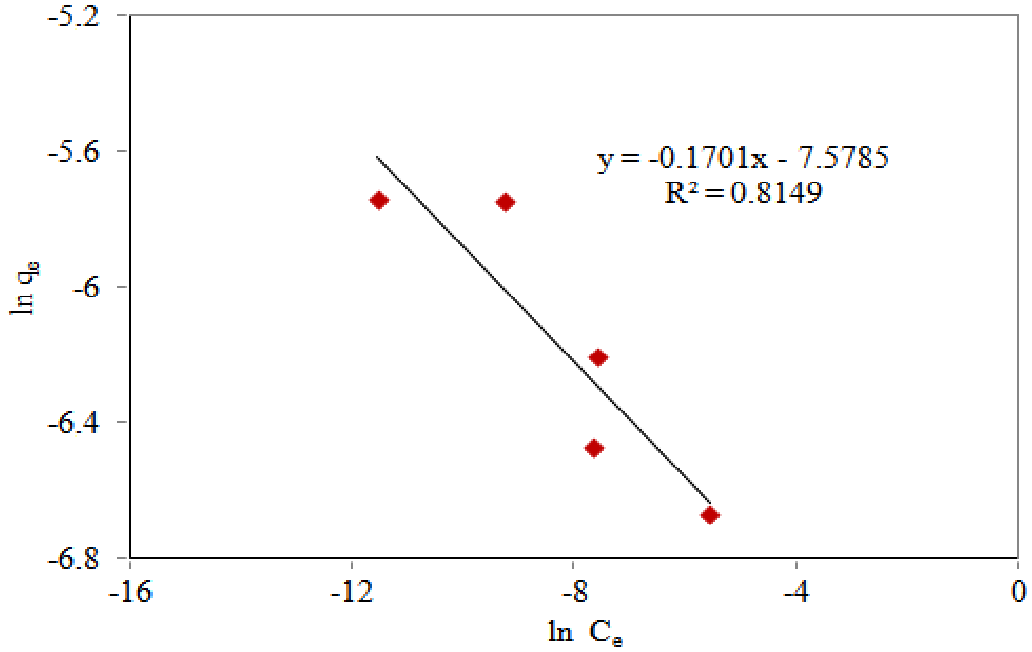

Figure 4.17. Freundlich adsorption isotherm for decolorization of MO. Conditions: pH: 5.85 (Natural), T=298 K, Flow rate= 2000 rpm.

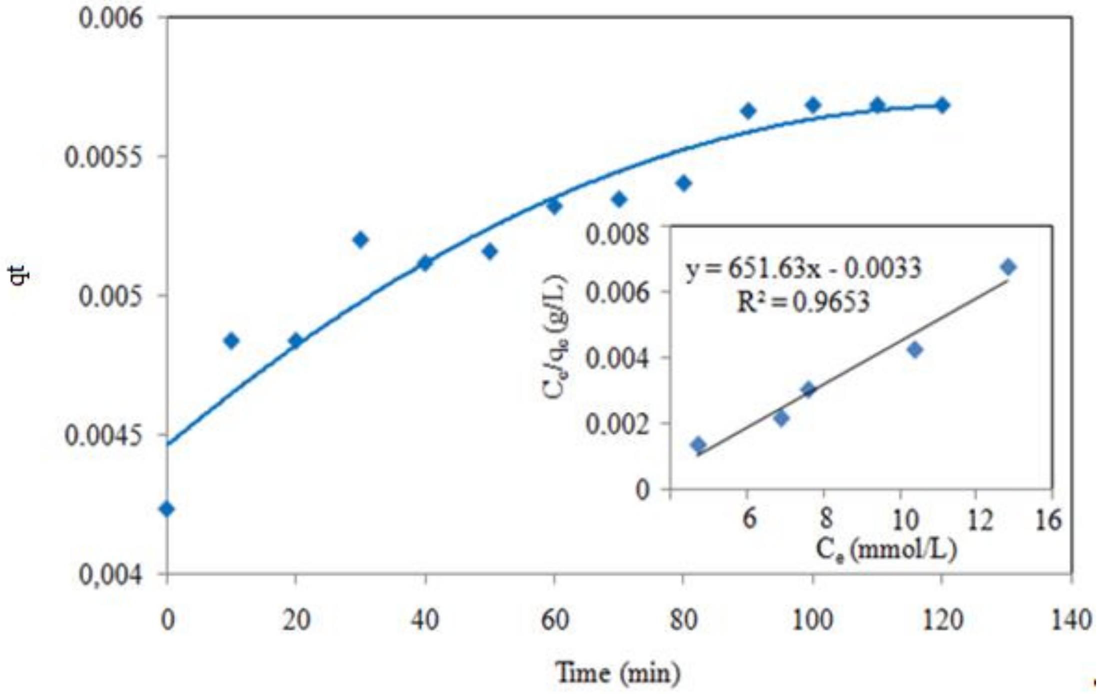

Figure 4.18. Langmuir adsorption isotherm for degradation of MO. Inset: Linearized form of Langmuir isotherm. Conditions: pH: 5.85 (Natural), T=298 K, Flow rate= 2000 rpm.

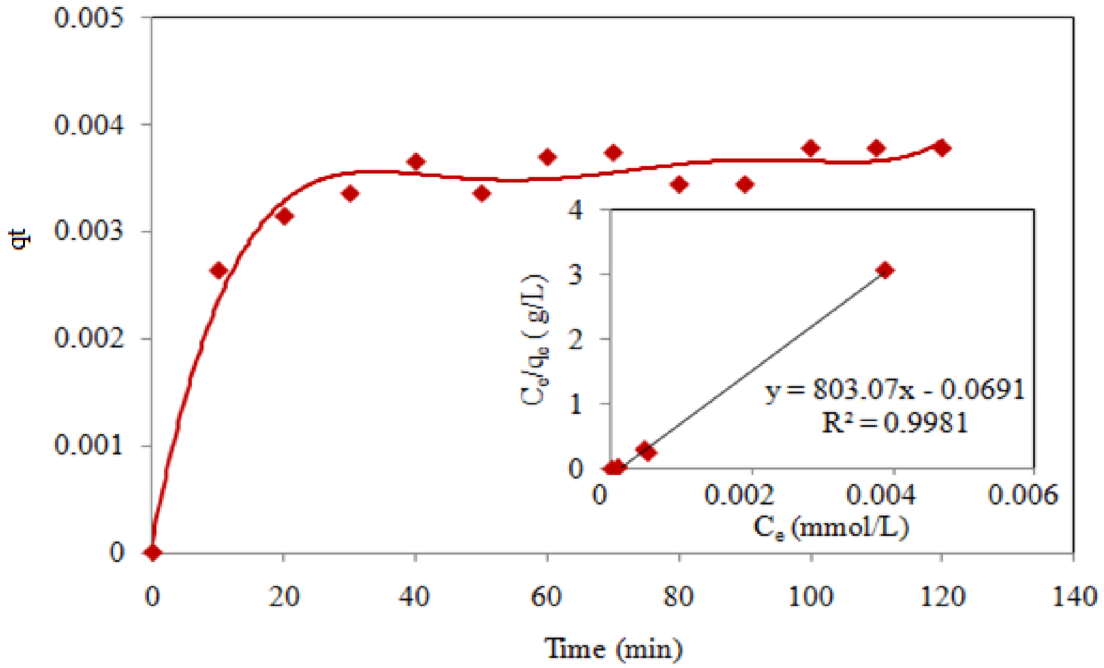

Figure 4.19. Langmuir adsorption isotherm for decolorization of MO. Inset:Linearized form of Langmuir isotherm. Conditions: pH:5.85 (Natural),T=298 K,Flow rate= 2000 rpm.

4.2.3. Photocatalytic Experiments

4.2.3.1. Effect of TiO_2 Loading. The photocatalytic experiments were performed with the catalysts of different TiO_2 loading under UV irradiation (Figure 4.20, Figure 4.21). Prior to the illumination, 30 min dark adsorption process was applied for all catalysts. Then, the remaining MO concentration was controlled for 10 min intervals. 40% TiO_2-FA catalyst revealed the best activity, with the lowest MO remaining concentration (53.3% for degradation and 30.5% for decolorization). Decrements in the TiO_2 contents lower the performances of the catalysts. As a general trend, the amount of MO remaining in solution following the decolorization processes were found to be lower than that of the degradation processes since it is more difficult to destroy the aromatic moiety of the substrate.

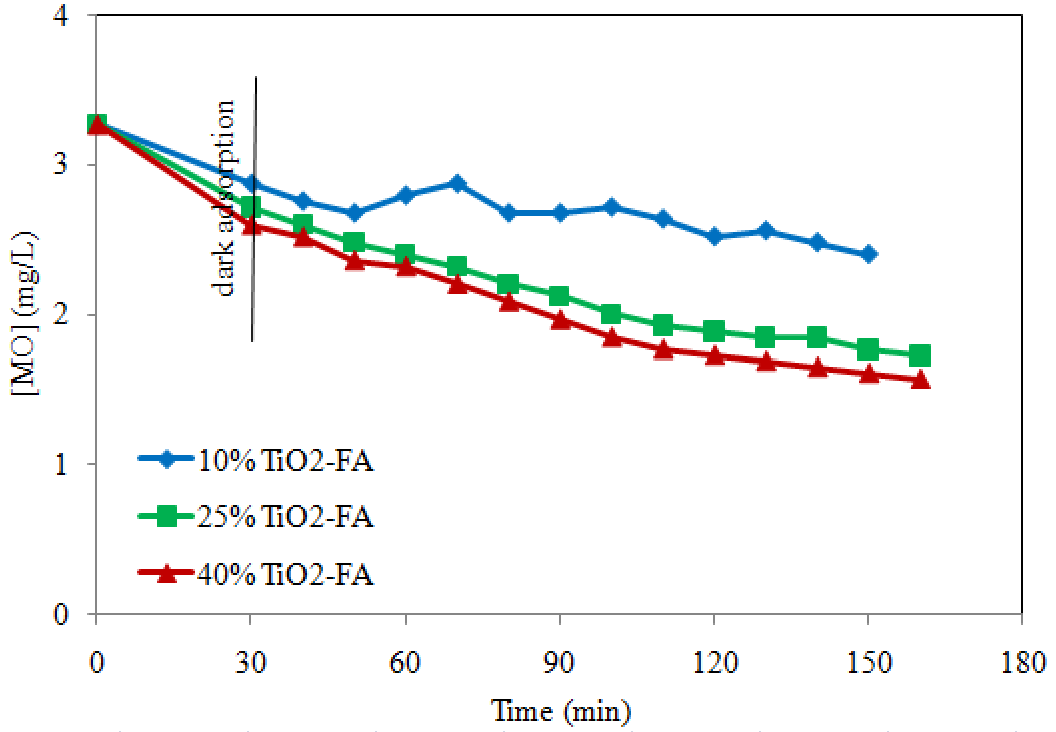

Figure 4.20. Effect of TiO_2 loading in the degradation of MO under UV irradiation. Conditions: pH: 5.85 (Natural), $[MO]_0$= 3.27 mg/L, I= 4.7x10^{15} photons/s, T=298 K, Flow rate= 2000 rpm.

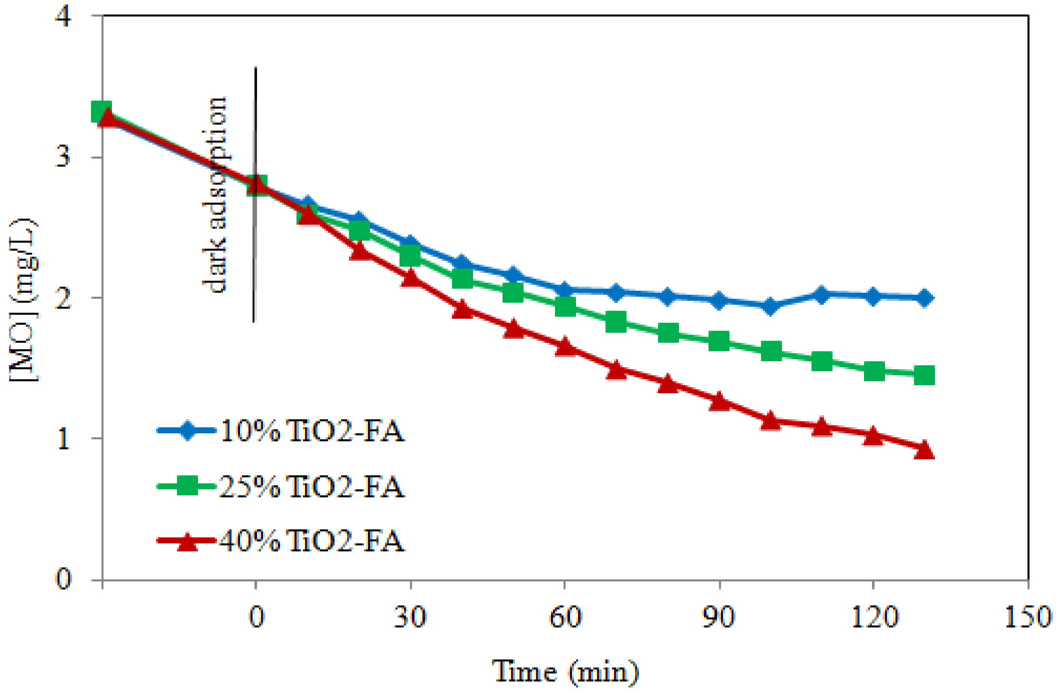

Figure 4.21. Effect of TiO_2 loading in the decolorization of MO. Conditions: pH: 5.85 (Natural), $[MO]_0$= 3.27 mg/L, I= $4.7x10^{15}$ photons/s, T=298 K, Flow rate= 2000 rpm.

4.2.3.2. Effect of Initial MO Concentration. The influence of initial MO concentration on the photocatalytic degradation and decolorization reactions was studied in the range of 16.3-3.27 mg/L in the presence of 25% TiO_2-FA (Figure 4.22, Figure 4.23). Pseudo-first order kinetics was confirmed by the linearity in the plot of ln (C_0/C) versus t based on equation 3.18 (Figure 4.24, Figure 4.25).

The rate constants (k min^{-1}) of the degradation and decolorization processes calculated from the slopes of the lines (Table 4.3). It was found that degradation and decolorization rates were inversely related to the MO concentration, i.e., with the increasing of the MO concentration, the decrement in the rate of the photocatalytic reactions was noticed. This might be as a result of blocking of the photocatalytically active sites on the supported catalysts and reducing the interaction of photons with these sites.

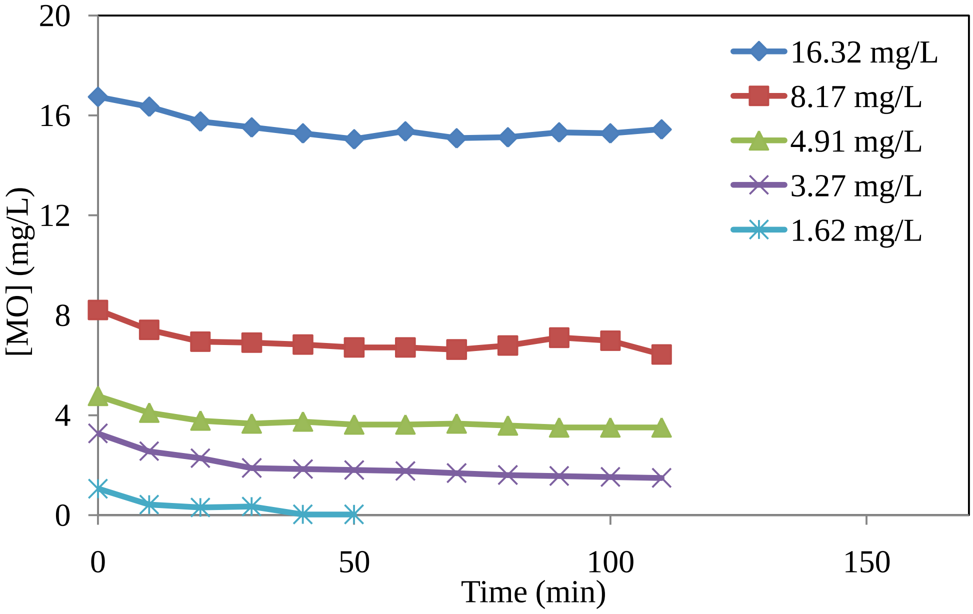

Figure 4.22. Effect of initial MO concentration on the photocatalytic degradation of MO in the presence of 25% TiO_2-FA. Conditions: pH: 5.85 (Natural), I= 4.7x10^{15} photons/s, T=298 K, Flow rate= 2000 rpm.

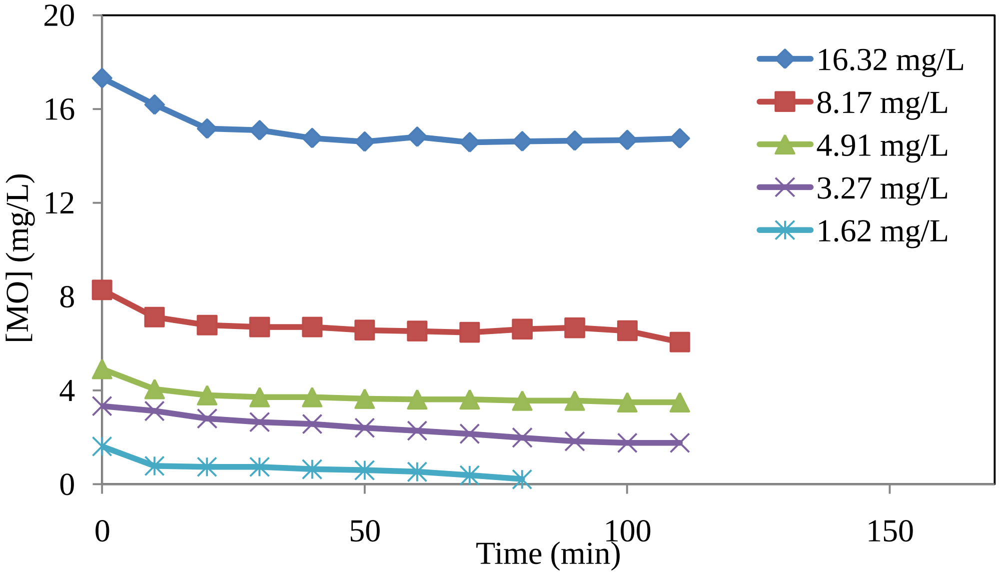

Figure 4.23. Effect of initial MO concentration on the photocatalytic degradation of MO in the presence of 25% TiO_2-FA Conditions: pH: 5.85 (Natural), I= 4.7x10^{15} photons/s, T=298 K, Flow rate= 2000 rpm.

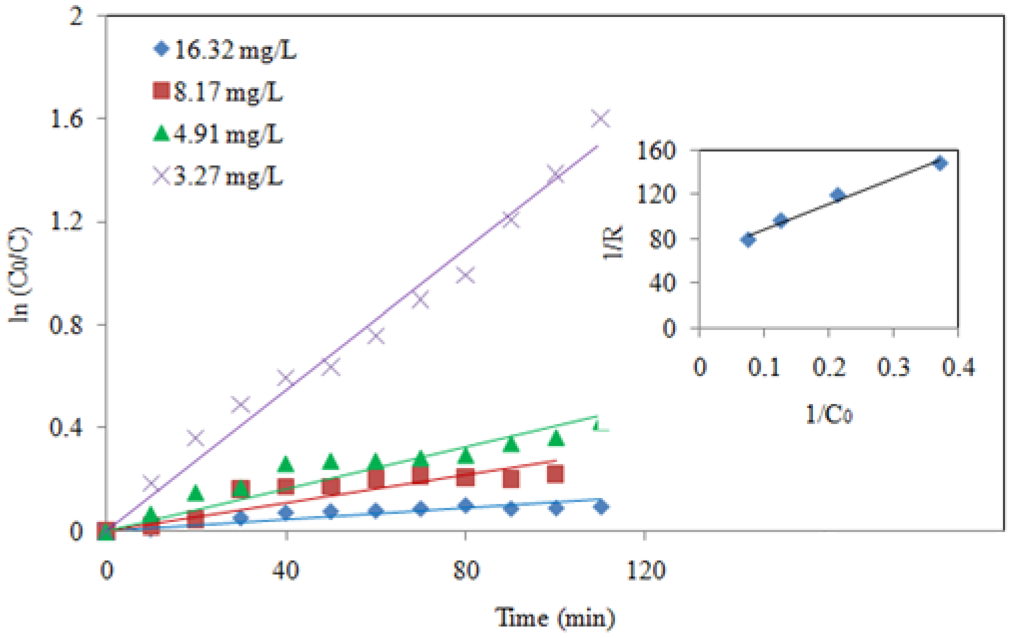

Figure 4.24. Pseudo-first order kinetics for degradation of MO. Inset: Langmuir-Hinshelwood kinetics for the degradation of MO. Conditions: pH: 5.85 (Natural), I= 4.7x1015 photons/s, T=298 K, Flow rate= 2000 rpm.

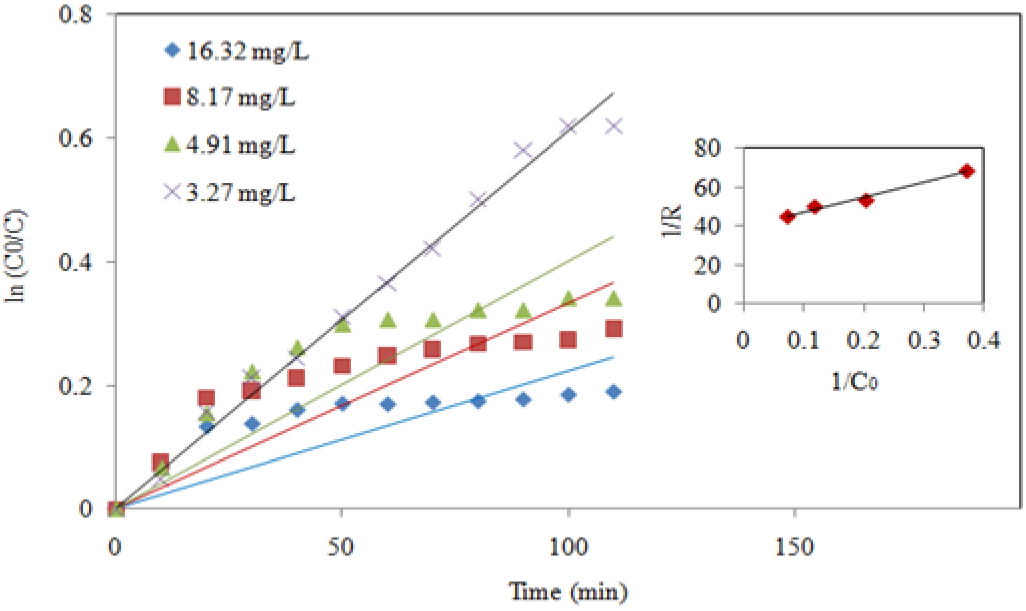

Figure 4.25. Pseudo-first order kinetics for decolorization of MO. Inset: Langmuir-Hinshelwood kinetics for the decolorization of MO. Conditions: pH: 5.85 (Natural), I= 4.7x10^{15} photons/s, T=298 K, Flow rate= 2000 rpm.

Table 4.3. Rate constants (k) and linear regression values (R) for the degradation and decolorization processes of the different initial concentrations of MO in the presence of 25% TiO_2-FA.

	k (min^{-1})		**R**	
[MO] (mg/L)	**degradation**	**decolorization**	**degradation**	**decolorization**
16.32	0.0009	0.0008	0.816	0.825
8.17	0.0011	0.0012	0.937	0.922
4.91	0.0014	0.0014	0.901	0.909
3.27	0.0015	0.0025	0.959	0.973

The kinetics of the photocatalytic degradation and decolorization processes was also analyzed by using Langmuir-Hinshelwood model. The applicability of Langmuir-Hinshelwood equation for the degradation and decolorization processes was confirmed by the linearity in the plot of reciprocal rate (1/R) against reciprocal of MO concentration ($1/C_0$) (Equation 3.12) (Figure 4.24 inset, Figure 4.25 inset). The values of the adsorption coefficient (K) and the reaction rate constant (k) were found to be 0.215 L/mg and 0.0163 mg/L min (for degradation) and 0.788 L/mg and 0.0237 mg/L min (for decolorization).

4.2.4. Reuse Properties of TiO_2-FA Catalysts

Reusing properties of the supported catalysts were investigated in recycling experiments (Figure 4.26). In general, particle filtration arises as a major problem whenever TiO_2 was utilized alone as a photocatalyst [96]. TiO_2 loaded FA catalysts can be used to minimize the problems in the filtration step. Hence, reuse properties of the 25% TiO_2-FA catalyst were determined by the recycling experiments for which the catalyst was filtrated, washed and calcinated at 500^oC about 2 h for each run. After four cycles, the remaining MO concentration in solution was found to increase only approximately 0.15 mg/L (from 1.64 to 1.79 mg/L) (for degradation) and 0.09 mg/L (from 0.99 to 1.08) (for decolorization). These results indicated that the photocatalytic activity of 25% TiO_2-FA had repeatability. The insignificant loss of the photoactivity could be explained either by the presence of reaction by-products adsorbed on the photocatalyst after the first run or by the loss of the photocatalyst during each collection and rinsing steps. Moreover, about 5% Ti was noticed in the SEM-EDX analysis of the catalyst after the fourth cycle. This percentage was almost similar to that obtained after the dark adsorption experiment. (Appendix A, Figure A.2)

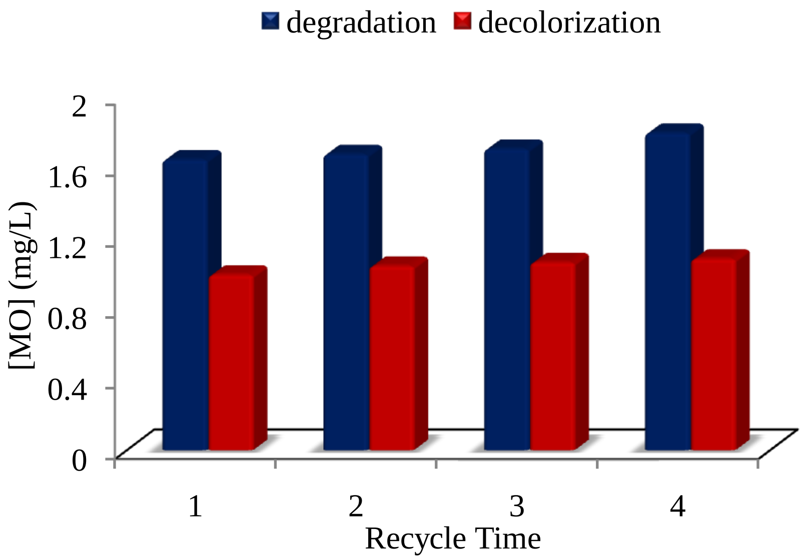

Figure 4.26. Results of recycling studies in the presence of 25% TiO_2-FA. Conditions: pH: 5.85 (Natural), $[MO]_0$= 3.27 mg/L, I= 4.7x10^{15} photons/s, T=298 K, Flow rate= 2000 rpm.

4.2.5. Photocatalytic Experiments for Visible Light Irradiation

The control of SA degradation under visible light irradiation was found to be negligible (Figure 4.27 inset). In the presence of the supported catalysts, following the 30 min dark adsorption, reductions in the SA concentration were not significant (Figure 4.30). Only a small variation in the initial SA concentration was noticed (11% in the presence of 25% TiO_2-FA and ~20% in the presence of 40% TiO_2-FA) and attributed to the adsorption abilities of the catalysts. These results corroborated with the UV-vis profiles of the catalysts. The lack of absorbance within the visible range resulted in the lower efficiency of the catalysts.

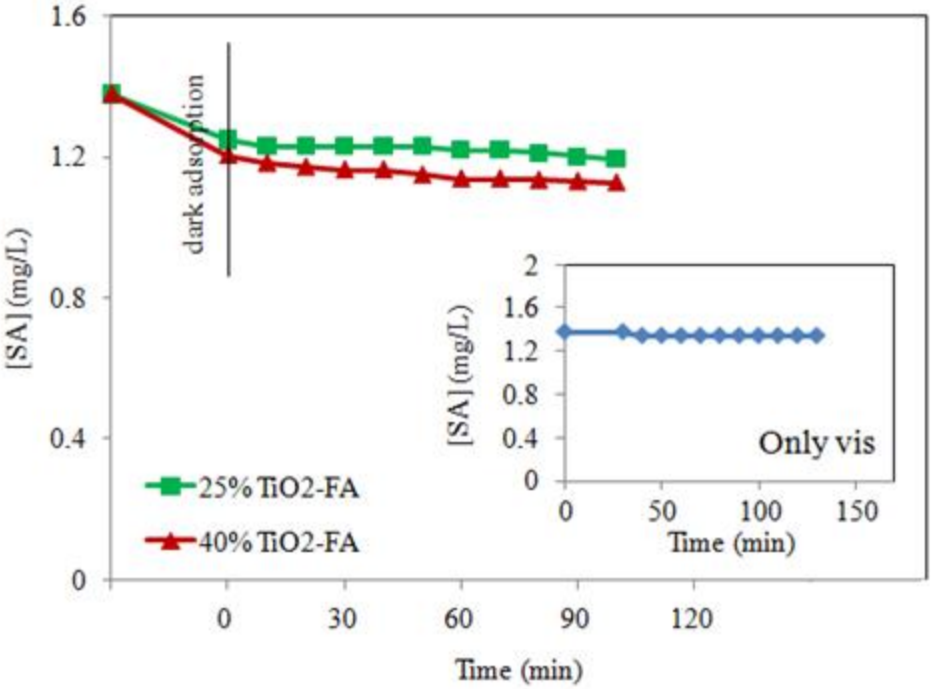

Figure 4.27. Photocatalytic degradation of salicylic acid with 25% TiO_2 and 40% TiO_2-FA catalysts under visible light irradiation. Inset: Photolysis of SA. Conditions: pH: 6.5 (Natural), $[SA]_0$= 1.38 mg/L, T=298 K, Flow rate= 2000 rpm.

4.3. Characterization Results of ZnO-FA Catalysts

4.3.1. XRD Analysis

ZnO diffraction peaks of (100), (002), (101), (102), (110), (103) and (200) were observed at 31.9, 34.6, 36.4, 47.7, 56.7, 63.1 and 66.6^o (2θ), respectively (Figure 4.28). Among these, the most intense (101) reflection at 36.4^o (2θ) was considered as the characteristic ZnO peak. Patterns of FA and the supported catalysts were shown in Figure 4.29. The typical FA and ZnO peaks were retained in the patterns of supported catalysts (Figure 4.29 A-D). ZnO peaks were more clearly observable in the pattern of 0.25 M ZnO-FA in comparison to those noticed in the pattern of 0.125M ZnO-FA. In the meantime, signals were not intensified for the 0.5M ZnO-FA catalyst, indicating formation of a saturation effect at 0.25M ZnO loading. The crystalline sizes of ZnO nanoparticles (D_{ZnO}), based on the broadening of the most intense (101) diffraction at 36.4° (2θ), were calculated by employing the Scherrer equation. The supported catalysts exhibited smaller crystalline sizes of ZnO nanoparticles in comparison to the 0.25M ZnO (16.18 nm). Also, increments in the loading concentration of ZnO reduced the crystalline sizes as 11.56 nm, 9.67 nm and 8.12 nm for 0.125M ZnO-FA, 0.25M ZnO-FA and 0.5M ZnO-FA, respectively. Thus, formation of ZnO aggregates was inhibited by the hollow structure of the FA. Moreover, the decrements in the reflections of the FA suggest their uniform distribution throughout the surface and bulk.

4.3.2. SEM (EDX) and Elemental Mapping Analysis

Structural morphologies of 0.25M ZnO and 0.25 M ZnO-FA were investigated by SEM analysis. 0.25 M ZnO catalyst exhibited a well ordered kidney-shaped crystals with the detection of only Zn (88.8 wt %) and O (11.2 wt %) peaks in the EDX analysis (Figure 4.30). The SEM image of FA was already shown in section 4.1.2. For 0.25 M ZnO-FA, the spherical and non-shaped particles of FA were retained, but non-uniform outer layers on top of the aggregates were additionally formed (Figure 4.31A). EDX analysis of the whole surface gave 58.5 wt % Zn (Table 4.4). Vacancies noticed in Si, Al, Ca mappings were considered as the probable adsorption sites of ZnO nanoparticles with dominated Zn signals on the top of the spheres or non-shaped particles of the support (Figure 4.31B-G).

4.3.3. Nitrogen Adsorption-Desorption Isotherms

Nitrogen adsorption-desorption isotherms and pore size distribution curves of the FA and supported catalysts were depicted in Figure 4.32 and Figure 4.33, respectively. The FA and 0.25M ZnO revealed Type II isotherms, specific non-porous materials. On the other hand, the supported catalysts exhibited Type IV isotherms with capillary condensation taking place in the range of high P/P_0. The pores of the supported catalysts existed in the typical mesoporous region of 20-40 Å (Figure 4.33). Besides, increments in the pore volumes resulted in higher surface areas for the supported catalysts (Table 4.5). 0.25M ZnO-FA and 0.5M ZnO-FA catalysts possessed similar surface areas due to the saturation effect at the 0.25M ZnO concentration. This was consistent with the limited variation of the XRD peak intensities of the catalysts.

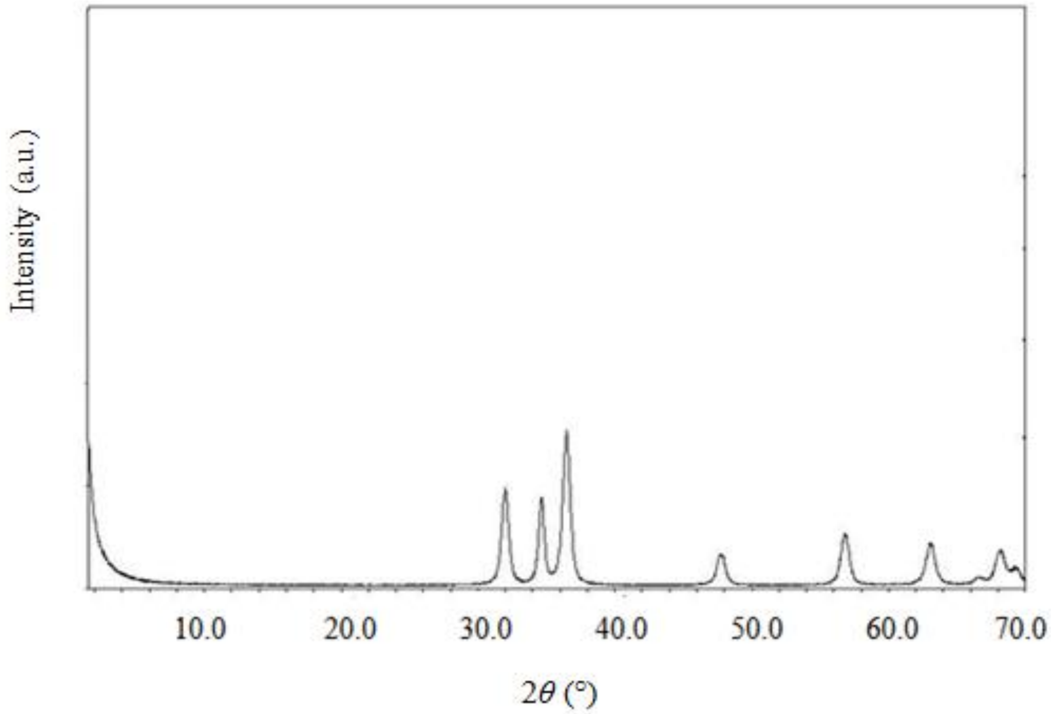

Figure 4.28. XRD pattern of 0.25M ZnO

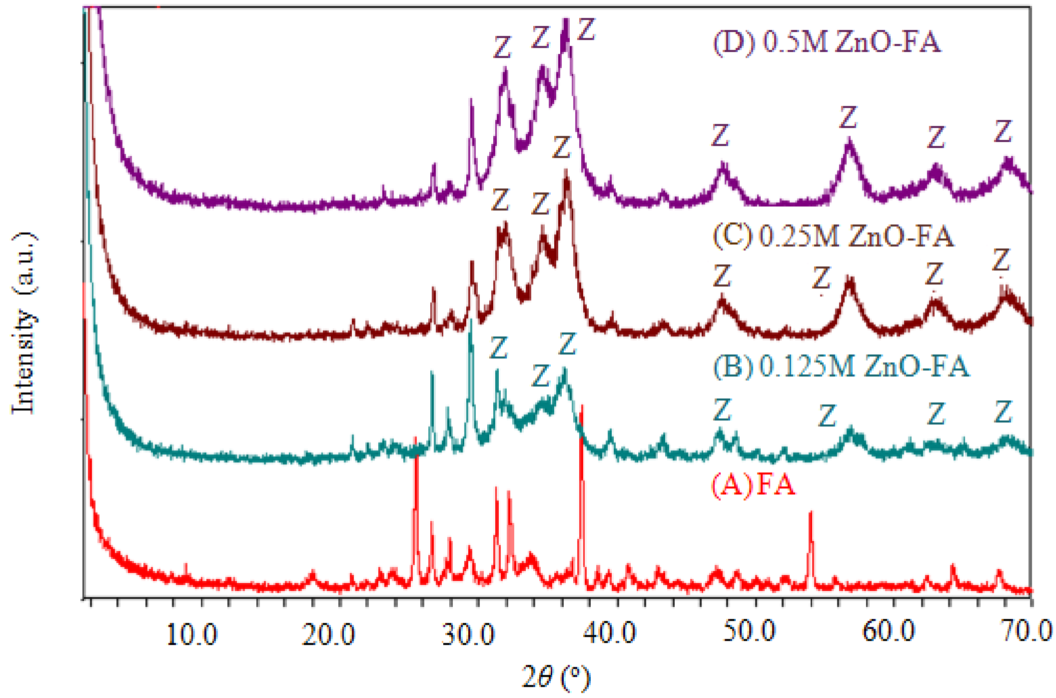

Figure 4.29. XRD patterns of FA (A) and supported catalysts (B-D). (Z: ZnO).

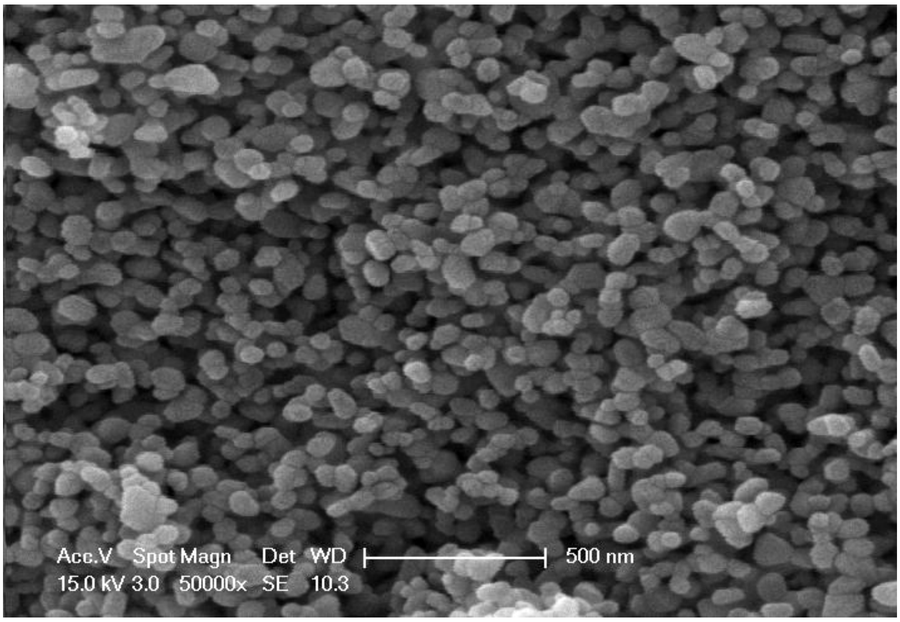

Figure 4.30. SEM image of 0.25M ZnO.

Table 4.4. Elemental composition of 0.25M ZnO-FA.

0.25M ZnO-FA	
Components	**Wt %**
Zn	58.54
O	18.80
Si	9.17
Al	6.13
Ca	7.36

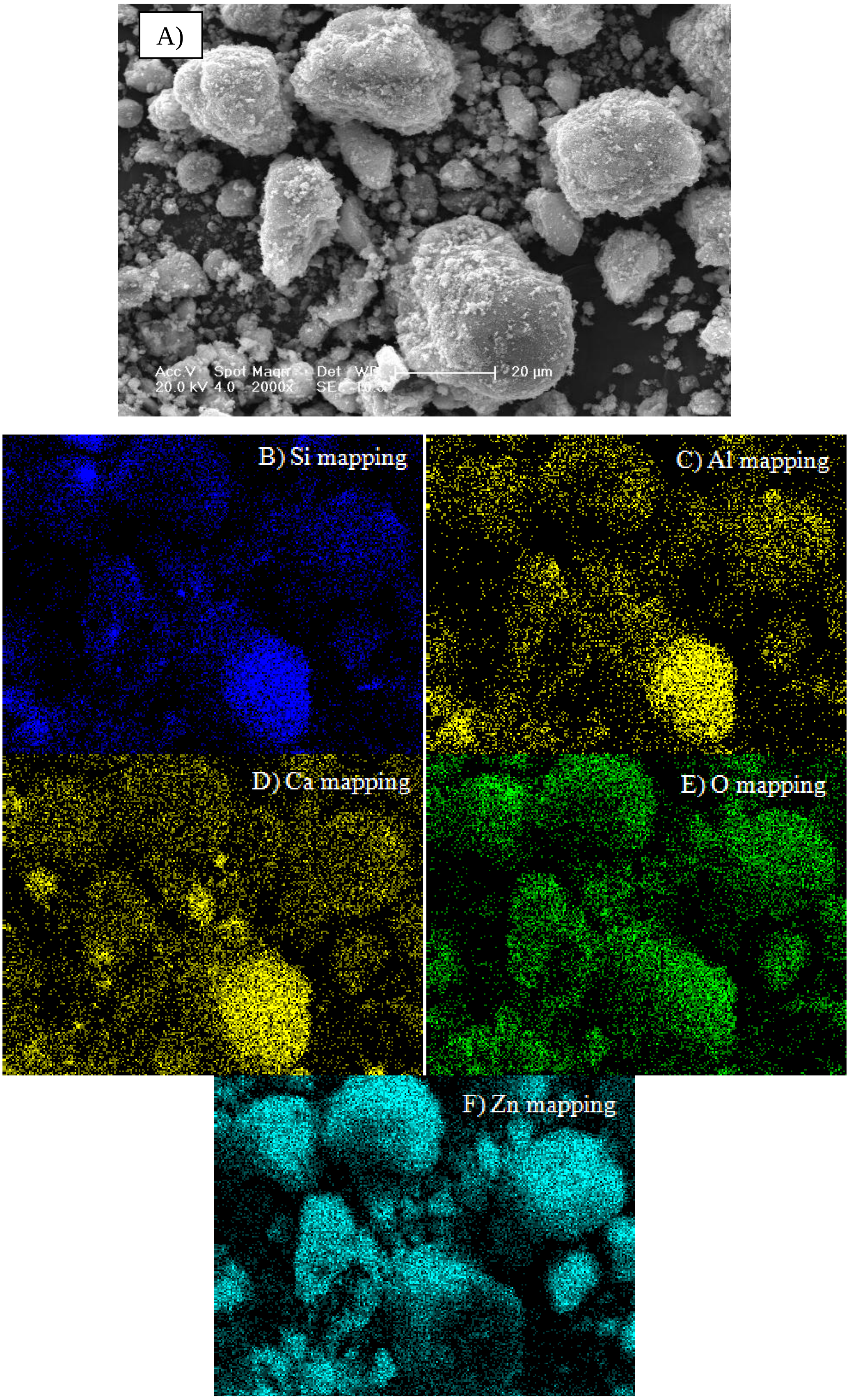

Figure 4.31. SEM and mapping images of 0.25M ZnO-FA (A), Si, Al, CA, O, Zn (B-F).

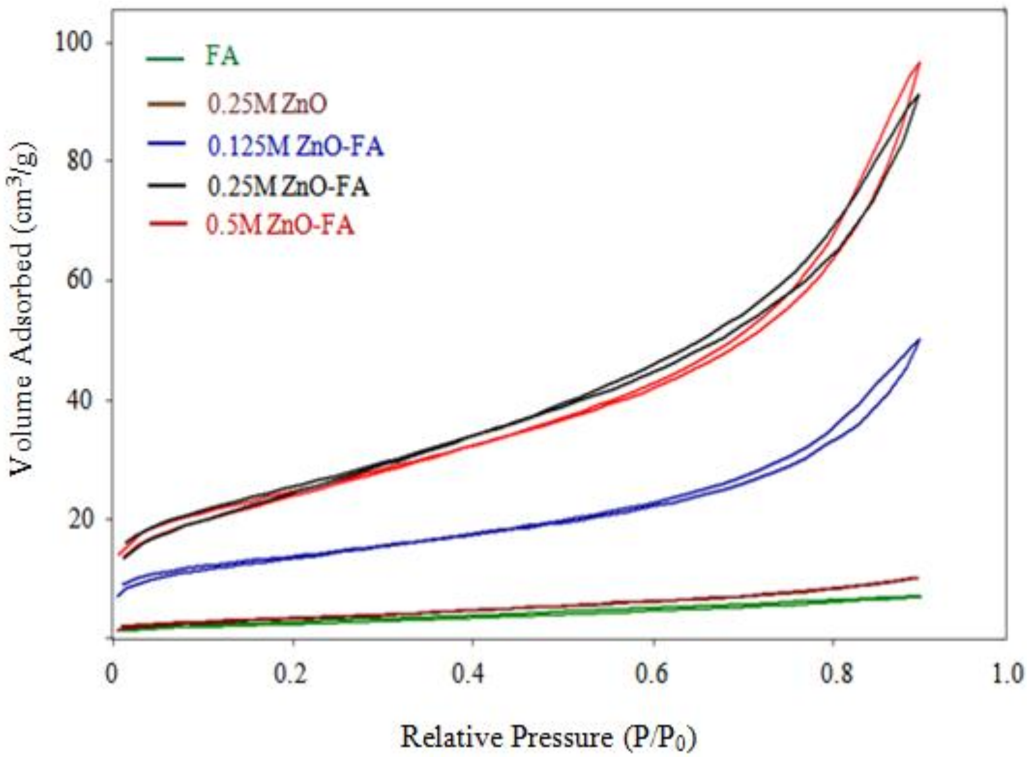

Figure 4.32. Nitrogen adsorption-desorption isotherms of FA, 0.25M ZnO and supported catalysts.

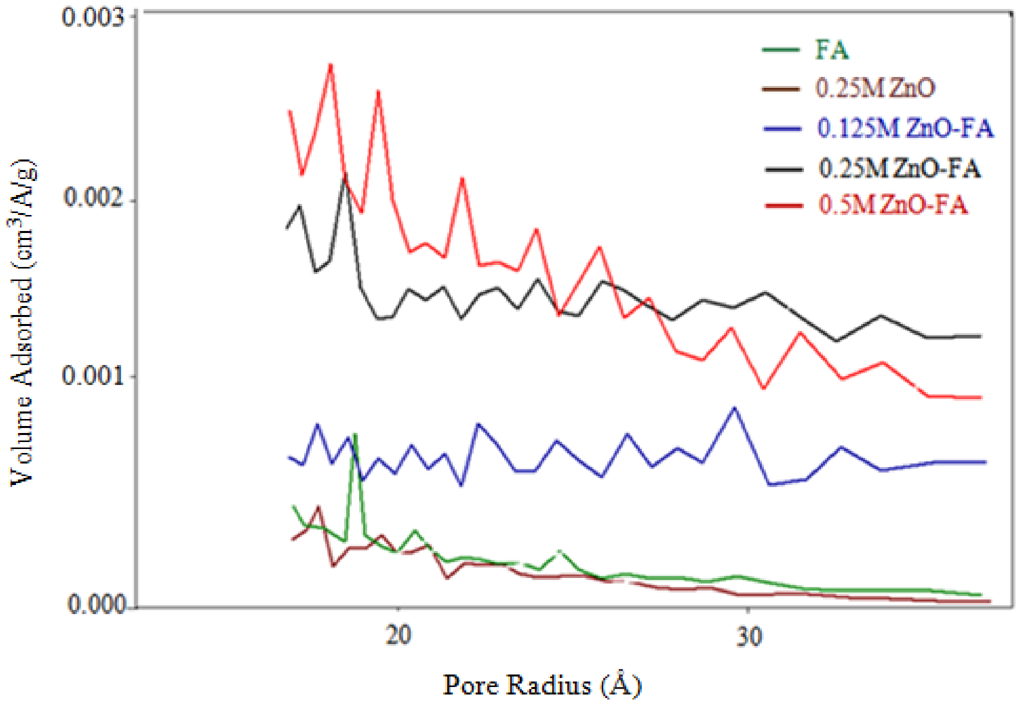

Figure 4.33. Pore size distribution plots of FA, 0.25M ZnO and supported catalysts.

Table 4.5. Surface areas (BET) and pore volumes (V_{pore}) of 0.25M ZnO, FA, and catalysts.

Materials	**BET (m^2/g)**	**V_{pore} (cm^3/g)**
0.25M ZnO	7.58	0.012
FA	5.61	0.009
0.125M ZnO-FA	30.81	0.067
0.25M ZnO-FA	59.08	0.133
0.5M ZnO-FA	60.15	0.122

4.3.4. UV-Vis DRS Analysis

The UV-vis absorption spectra of the FA, 0.25M ZnO and the supported catalysts were illustrated in Figure 4.34. All ZnO loaded FA catalysts exhibited the characteristic sharp absorption edge of ZnO and their absorption profiles increase with the loading concentration of ZnO in the low wavelength regions (below 380-390 nm). Around 380-390 nm, the absorption edges of all supported catalysts shifted slightly to the longer wavelength regions in comparison to 0.25M ZnO due to the existence of FA in the composite structure.

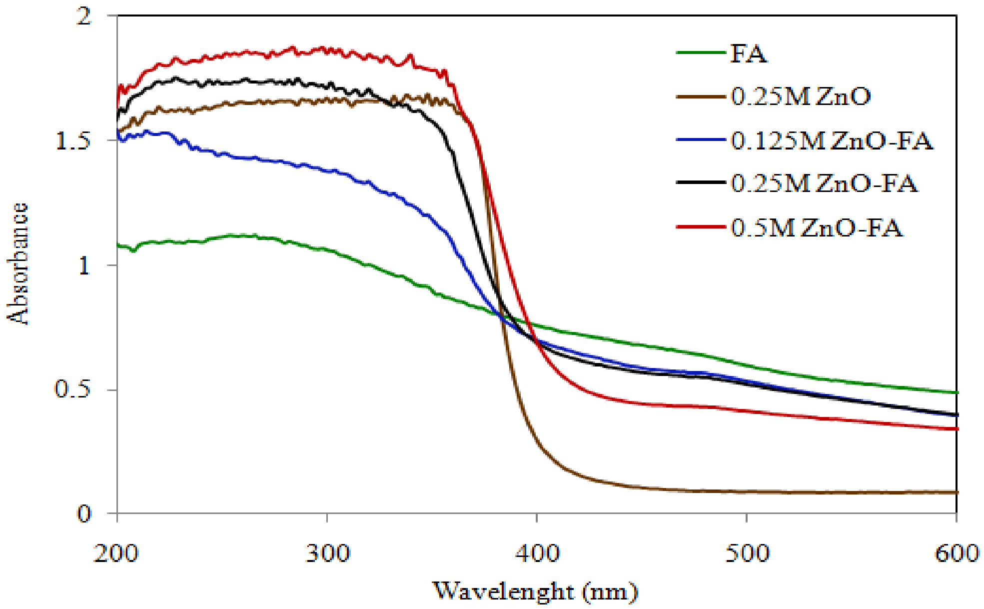

Figure 4.34. UV-vis DRS spectra of FA, 0.25M ZnO and supported catalysts.

4.4. Degradation Results of ZnO-FA Catalysts

4.4.1. Control Experiments

Similar to the TiO_2-FA systems, two sets of control experiments were done in order to examine the dark adsorption capacities and photocatalytic degradation abilities of ZnO-FA catalysts. In the first set, the raw support (FA) and the as-prepared catalysts (0.25M ZnO and 0.25M ZnO-FA) were compared in terms of dark adsorption capacities (Figure 4.35). In the second set, photolysis of MO (Figure 4.36 inset) and photocatalytic activities of the 0.25M ZnO and 0.25M ZnO-FA catalysts were controlled under UV illumination (Figure 4.36).

In the dark, the remaining MO concentration in the solution did not vary significantly in the presence of only FA and 0.25M ZnO. Meanwhile, 0.25M ZnO showed a better adsorption in comparison to FA. The transformation of FA structure into a mesoporous adsorbent with in situ growth of ZnO nanoparticles enhanced the adsorption ability of the 0.25M ZnO-FA catalyst (Figure 4.35). Also, Zn percentage (about 57 wt %) in the catalyst matrix did not vary after the dark adsorpton experiment (Appendix A, Figure A.3).

For the irradiation experiments, a different route was followed (in comparison to TiO_2-FA systems). Since dark adsorption capacity of the 0.25M ZnO-FA was quite high, the short period of 2 min was selected for the mixing of 0.25M ZnO-FA with MO in the dark. In contrast, 30 min contact of MO was applied to 0.25M ZnO under dark. Following the dark experiments, both catalysts (0.25M ZnO and 0.25M ZnO-FA) demonstrated photoactivities while the supported one revealed a higher degradation ability within a relatively shorter irradiation time (Figure 4.36).

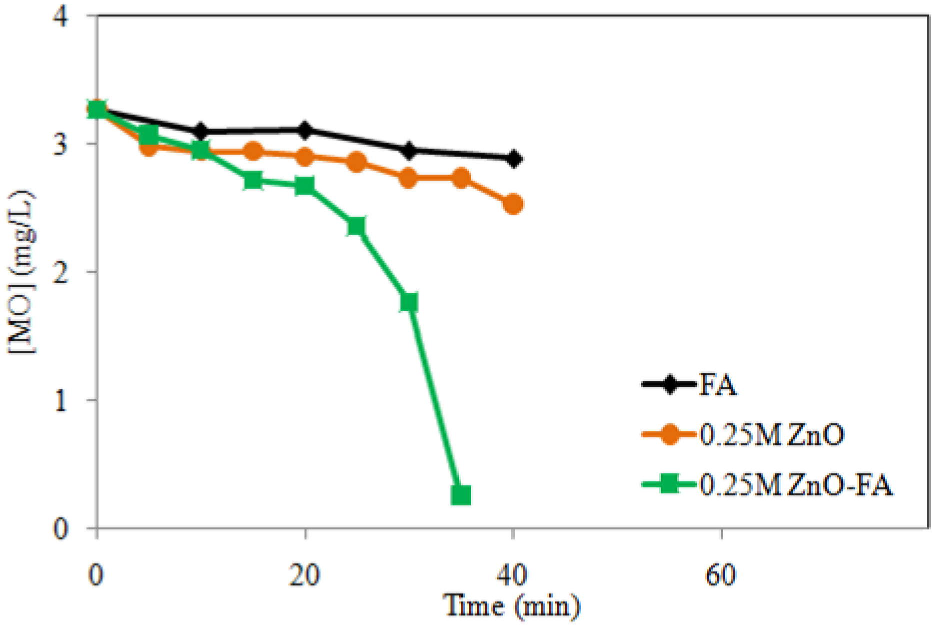

Figure 4.35. Control experiments in the dark. Conditions: pH: 5.85 (Natural), $[MO]_0$= 3.27 mg/L, T=298 K, Flow rate= 2000 rpm.

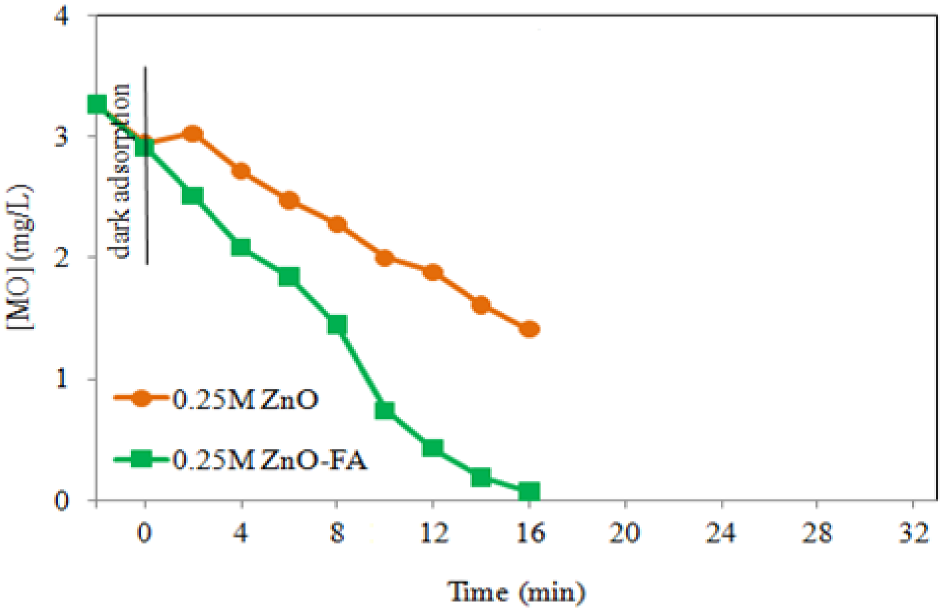

Figure 4.36. Control experiments under UV irradiation. Inset: Photolysis of MO Conditions: pH: 5.85 (Natural), $[MO]_0$= 3.27 mg/L, I= 4.7×10^{15} photons/s, T=298 K, Flow rate= 2000 rpm.

4.4.2. Dark Adsorption Experiments

4.4.2.1. Adsorption Kinetics. In this section, adsorption details of MO (3.27 mg/L, 0.01 mmol/L) over the 0.5M ZnO-FA catalyst was studied.

The pseudo-first order model (Equation 3.4) gave straight lines in the plots of ln (q_e-q_t) versus t with correlation coefficients of 0.9171 (for degradation) and 0.9150 (for decolorization) (Figure 4.37, Figure 4.38).

However, higher correlation coefficients with a better adsorption possibility of MO molecules were obtained with the application of the pseudo-second order model (Equation 3.6), 0.9958 and 0.9967 for degradation and decolorization experiments (Figure 4.39, Figure 4.40), respectively.

4.4.2.2. Adsorption Isotherms. Five different MO concentrations (32.7, 16.3, 8.17, 4.91, 3.27 mg/L) were controlled in the presence of 0.5M ZnO-FA catalyst for the Freundlich (Equation 3.8) and Langmuir (Equation 3.9) isotherm models.

The line fittings of ln q_e versus ln C_e in Freundlich isotherms revealed 0.6473 (for degradation) and 0.9288 (for decolorization) correlation coefficients (Figure 4.41, Figure 4.42)

According to the Langmuir isotherm model, the amount of MO adsorbed per gram of adsorbent (q_t) reached an equilibrium by time t (min) for degradation and decolorization processes (Figure 4.43, Figure 4.44). Also, the correlation coefficients (noticed in the linearity of C_e/q_e versus C_e plots*)* were obtained as 0.9951 (for degradation) from the Figure 4.43 inset and 0.9943 (for decolorization) the Figure 4.44 inset. Thus, Langmuir model indicated a kind of monolayer coverage of the MO molecules on the supported catalyst surface. From the slope of the lines in Figure 4.43 and Figure 4.44, Langmuir adsorption capacities were calculated as 2.05 mg/g and 2.25 mg/g for degradation and decolorization processes, respectively.

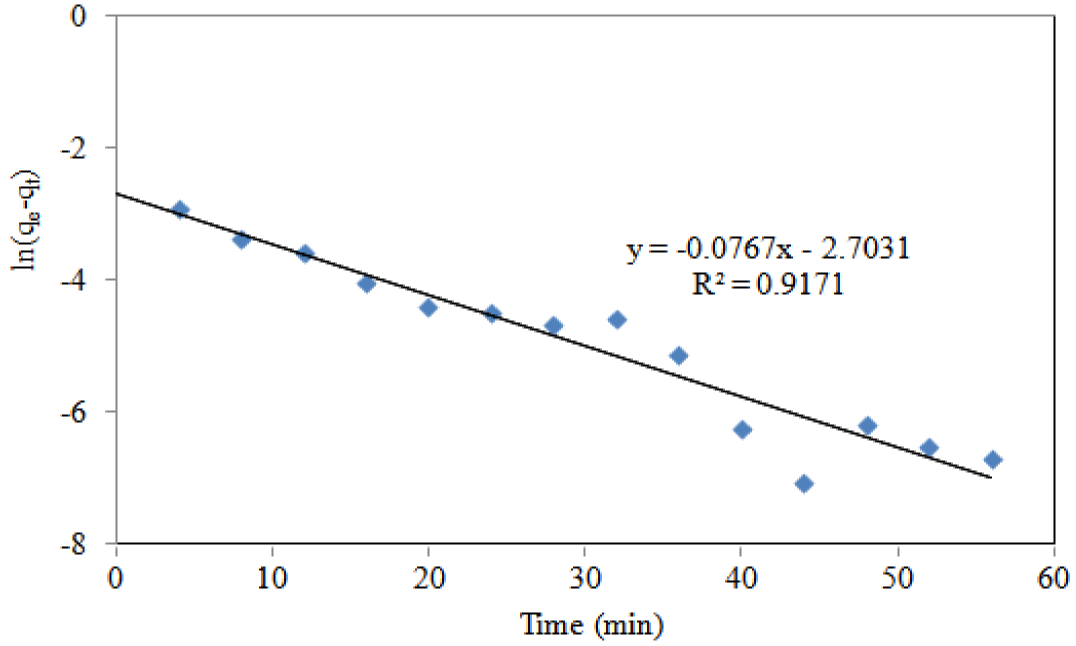

Figure 4.37. Pseudo first order kinetics for degradation of MO. Conditions: pH: 5.85 (Natural), $[MO]_0$= 3.27 mg/L, T=298 K, Flow rate= 2000 rpm.

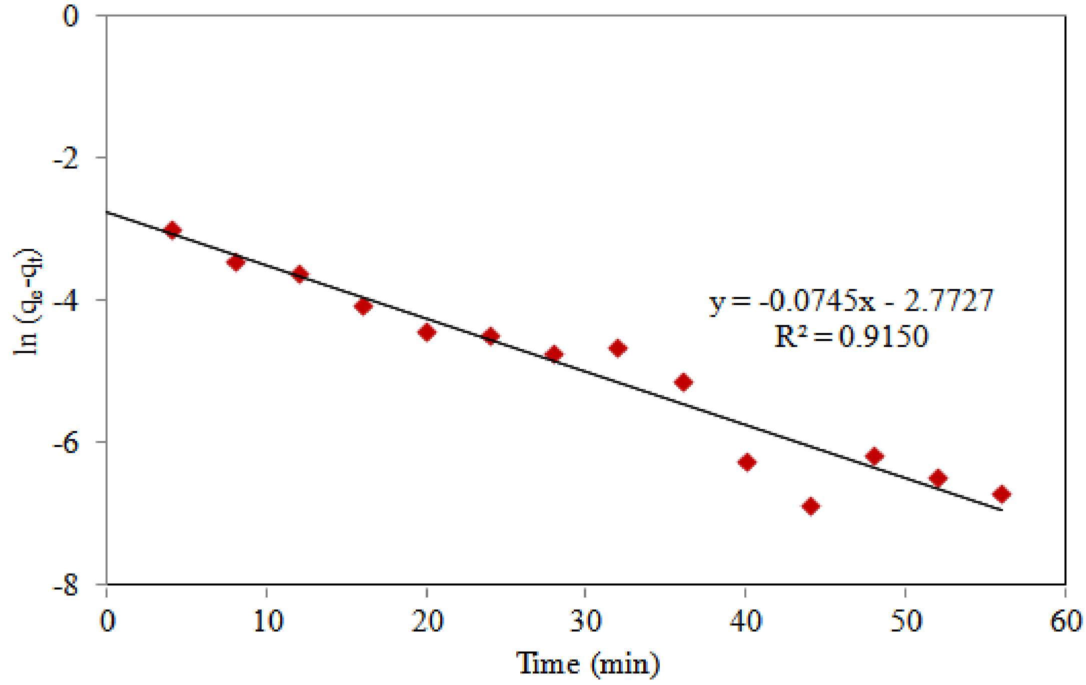

Figure 4.38. Pseudo first order kinetics for decolorization of MO. Conditions: pH: 5.85 (Natural), $[MO]_0$= 3.27 mg/L, T=298 K, Flow rate= 2000 rpm.

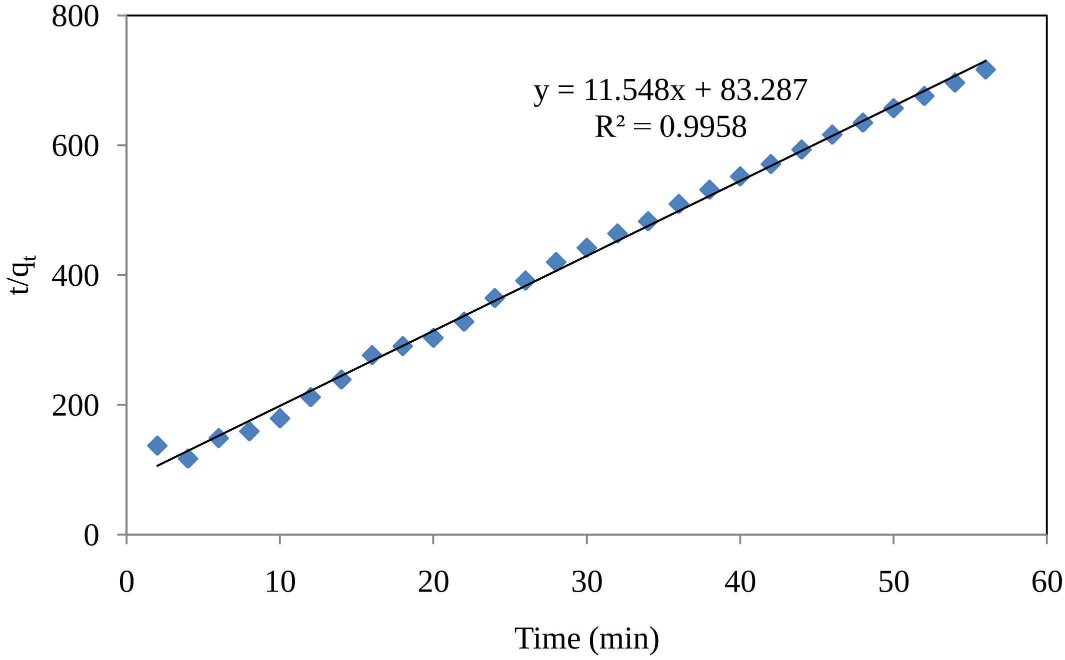

Figure 4.39. Pseudo-second order kinetics for degradation of MO. Conditions: pH: 5.85 (Natural), $[MO]_0$= 3.27 mg/L, T=298 K, Flow rate= 2000 rpm.

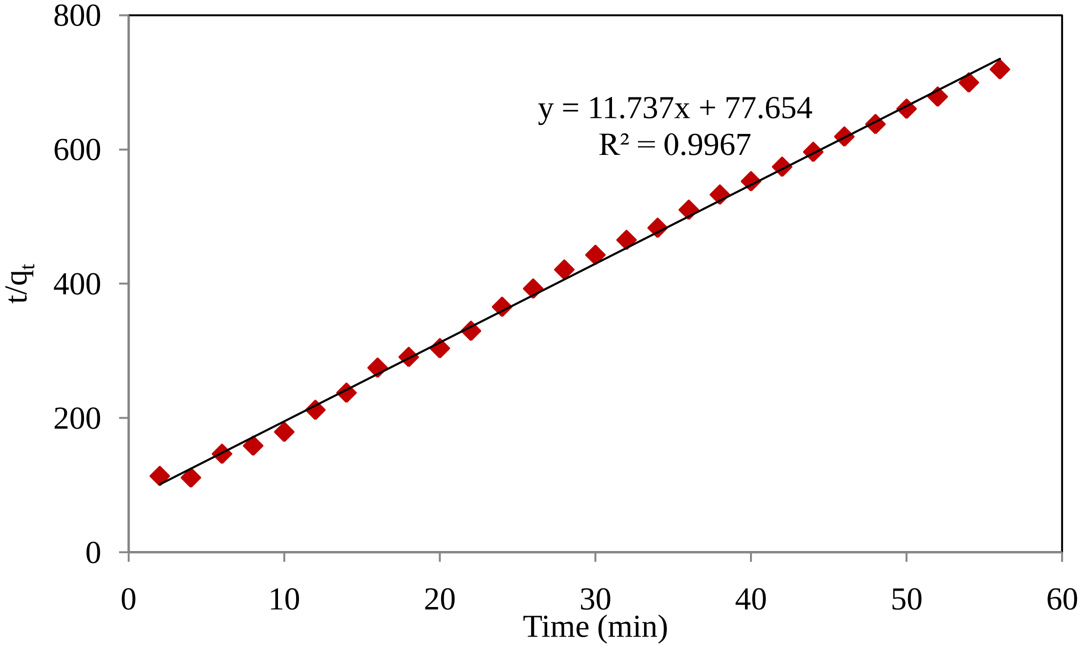

Figure 4.40. Pseudo-second order kinetic for decolorization of MO. Conditions: pH: 5.85 (Natural), $[MO]_0$= 3.27 mg/L, T=298 K, Flow rate= 2000 rpm.

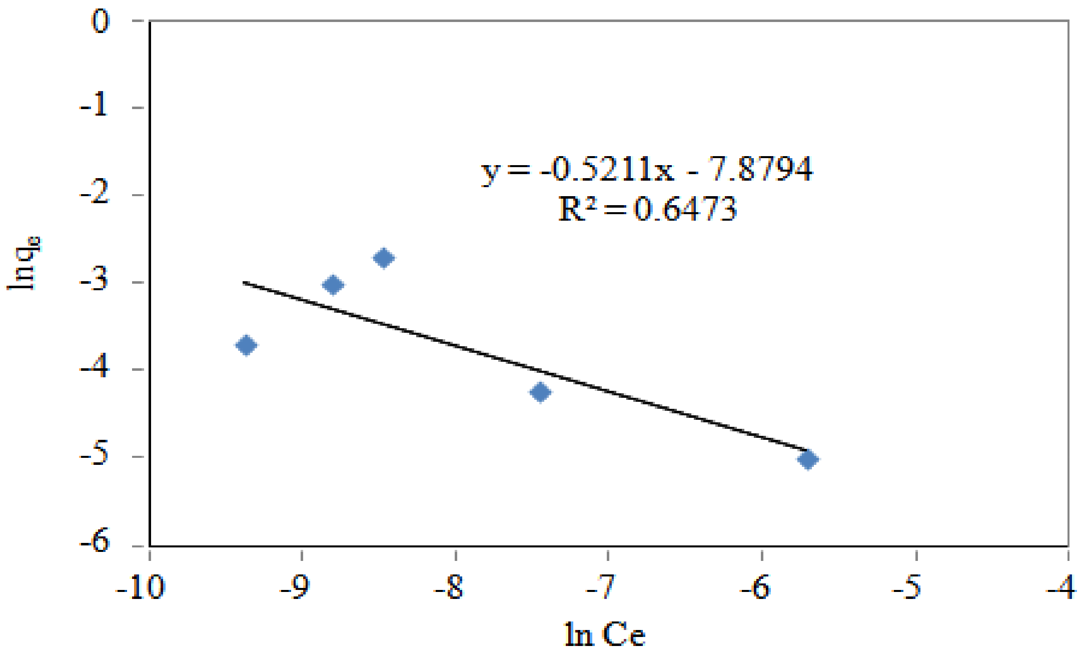

Figure 4.41. Freundlich adsorption isotherm for degradation of MO. Conditions: pH: 5.85 (Natural), T=298 K, Flow rate= 2000 rpm.

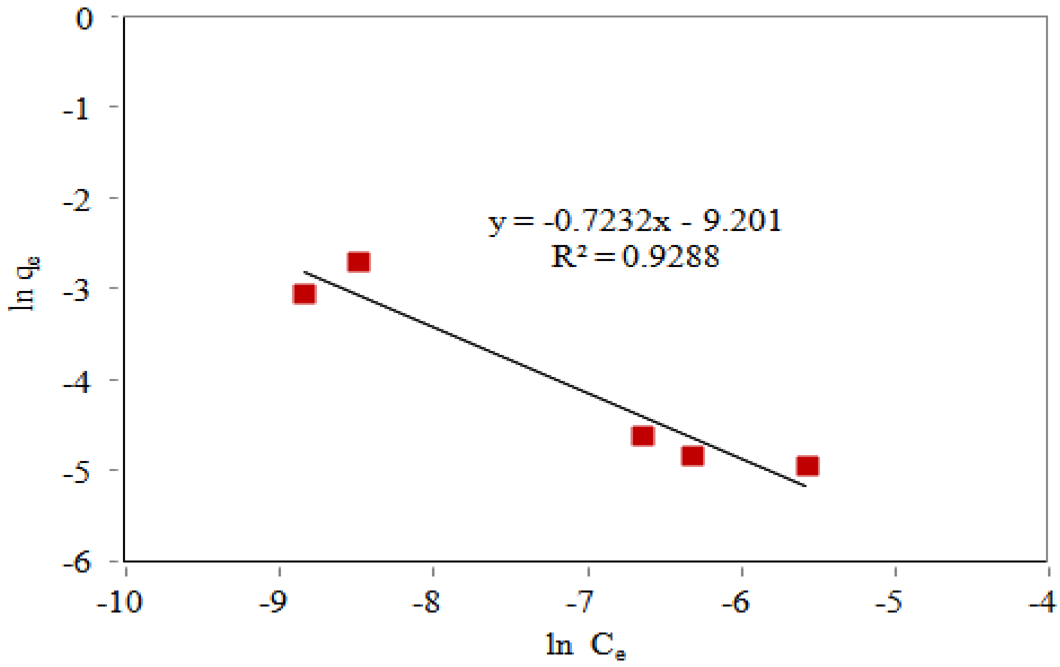

Figure 4.42. Freundlich adsorption isotherm for decolorization of MO. Conditions: pH: 5.85 (Natural), T=298 K, Flow rate= 2000 rpm.

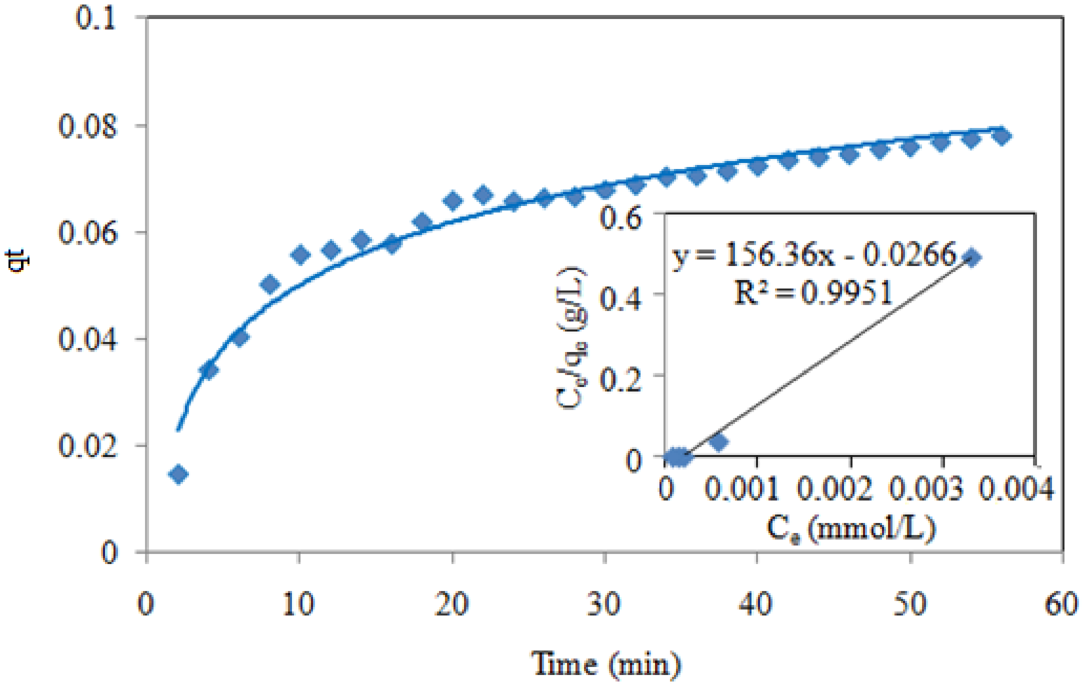

Figure 4.43. Langmuir adsorption isotherm for degradation of MO. Inset: Linearized form of Langmuir isotherm. Conditions: pH: 5.85 (Natural), T=298 K, Flow rate= 2000 rpm.

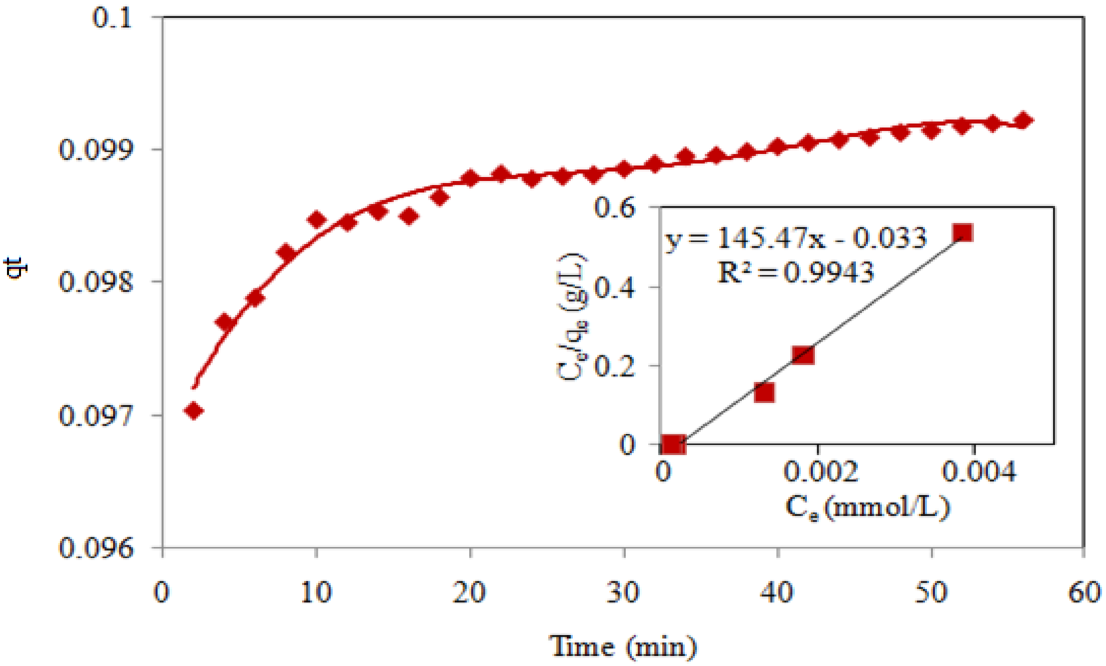

Figure 4.44. Langmuir adsorption isotherm for decolorization of MO. Inset: Linearized form of Langmuir adsorption isotherm. Conditions: pH:5.85 (Natural), T=298 K, Flow rate= 2000 rpm.

4.4.3. Photocatalytic Experiments

4.4.3.1. Effect of ZnO Loading. The photocatalytic experiments were performed with the catalysts of different ZnO loading concentrations under UV irradiation (Figure 4.45, Figure 4.46). Prior to the illumination, 2 min dark adsorption process was applied for all catalysts and the MO concentrations remaining in the solution were found as 3.0 mg/L, 2.9 mg/L, 0.73 mg/L (for degradation) and 2.8 mg/L, 2.8 mg/L, 0.9 mg/L (for decolorization) in the presence of 0.125M ZnO-FA, 0.25M ZnO-FA and 0.5M ZnO-FA, respectively. Then, MO concentrations were controlled for 2 min intervals under irradiation. The best photocatalytic performance was exhibited by 0.5M ZnO-FA catalyst in less than 10 min whereas 0.125M ZnO-FA showed an activity within approximately 30 min irradiation.

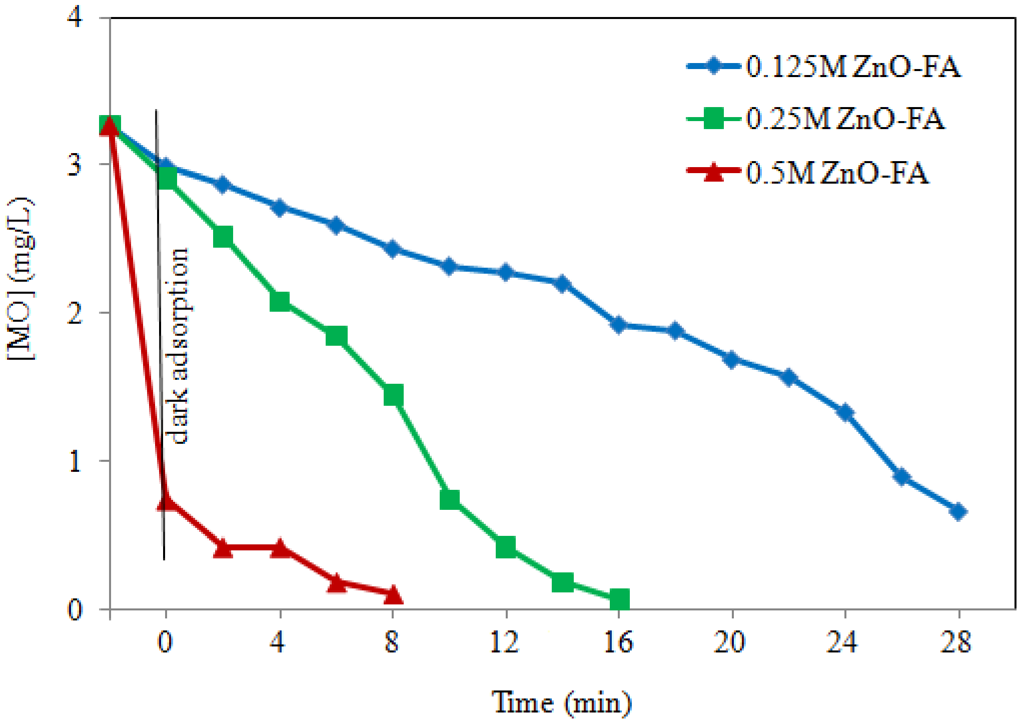

Figure 4.45. Effect of ZnO loading for the photocatalytic degradation of MO under UV irradiation. Conditions: pH: 5.85 (Natural), $[MO]_0$= 3.27 mg/L, I= 4.7x10^{15} photons/s, T=298 K, Flow rate= 2000 rpm.

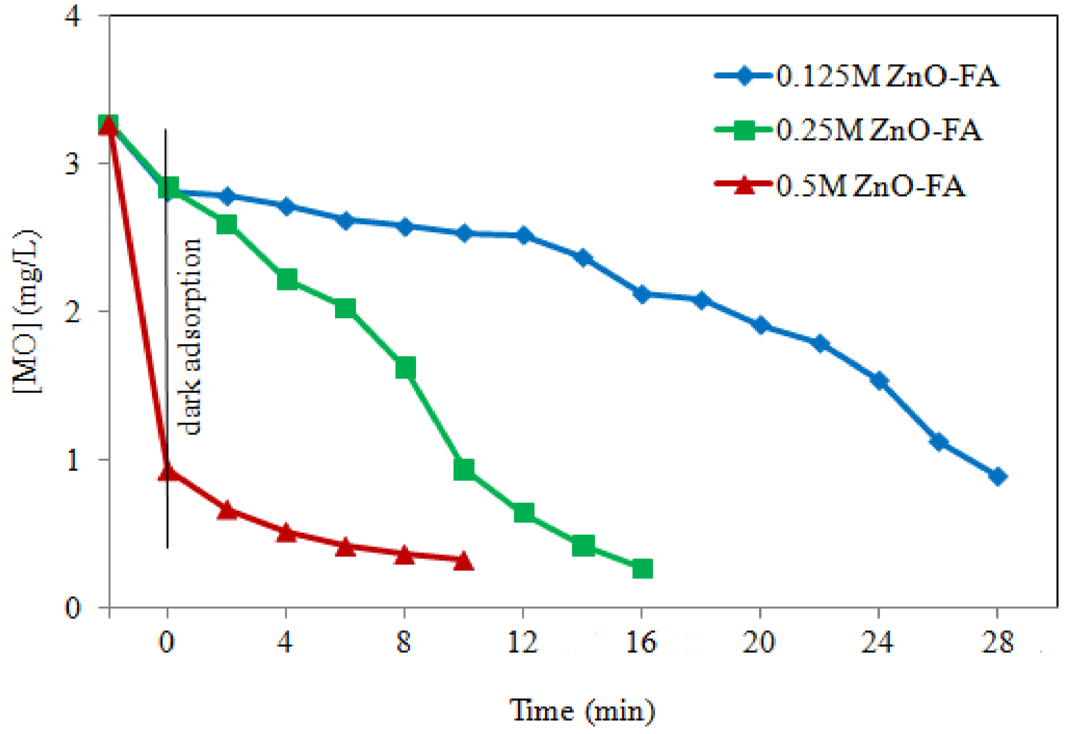

Figure 4.46. Effect of ZnO loading for the photocatalytic decolorization of MO under UV irradiation. Conditions: pH: 5.85 (Natural), $[MO]_0$= 3.27 mg/L, I= 4.7x10^{15} photons/s, T=298 K, Flow rate= 2000 rpm.

4.4.3.2. Effect of Initial MO Concentration. Experiments in this section were conducted in the initial concentration range of 3.27-32.7 mg/L with the 0.5M ZnO-FA catalyst (Figure 4.47, Figure 4.48). Following 2 min dark adsorption experiments (not labeled in the figures), MO remaining concentrations decreased by time. The kinetics obeyed pseudo-first order model based on the linearity obtained in the plot of ln (C_0/C) versus t for all concentrations (Equation 3.10, Figure 4.49 and Figure 4.50).

The rate constants (k min^{-1}) of the degradation and decolorization processes calculated from the slopes of the lines (Table 4.6). An inverse relation was detected between rate constants and MO concentrations.

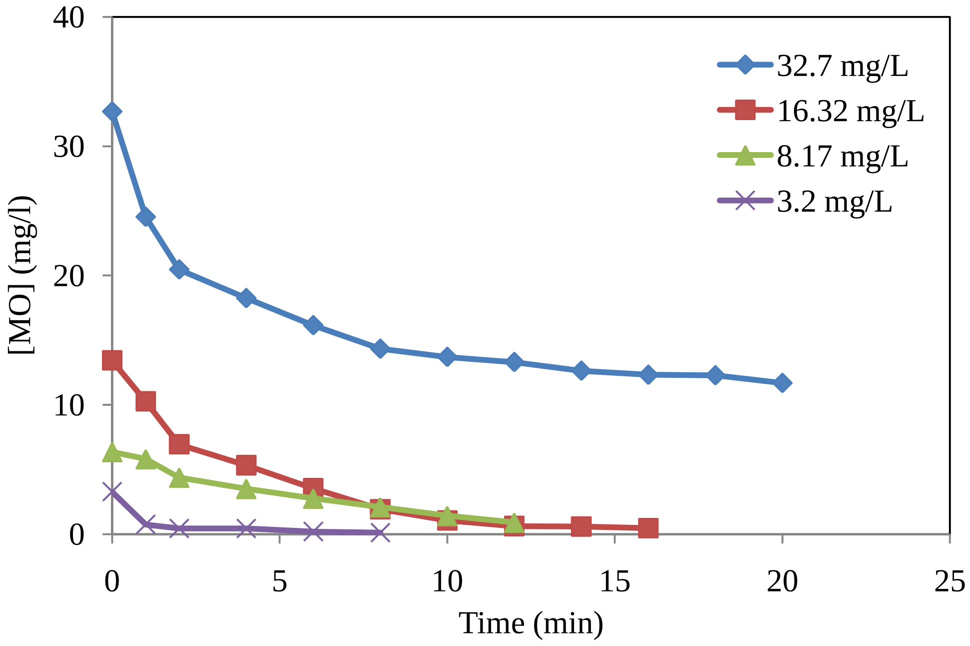

Figure 4.47. Photocatalytic degradation of MO in the presence of 0.5M ZnO-FA at different initial MO concentrations. Conditions: pH: 5.85 (Natural), I= 4.7x10^{15} photons/s, T=298 K, Flow rate= 2000 rpm.

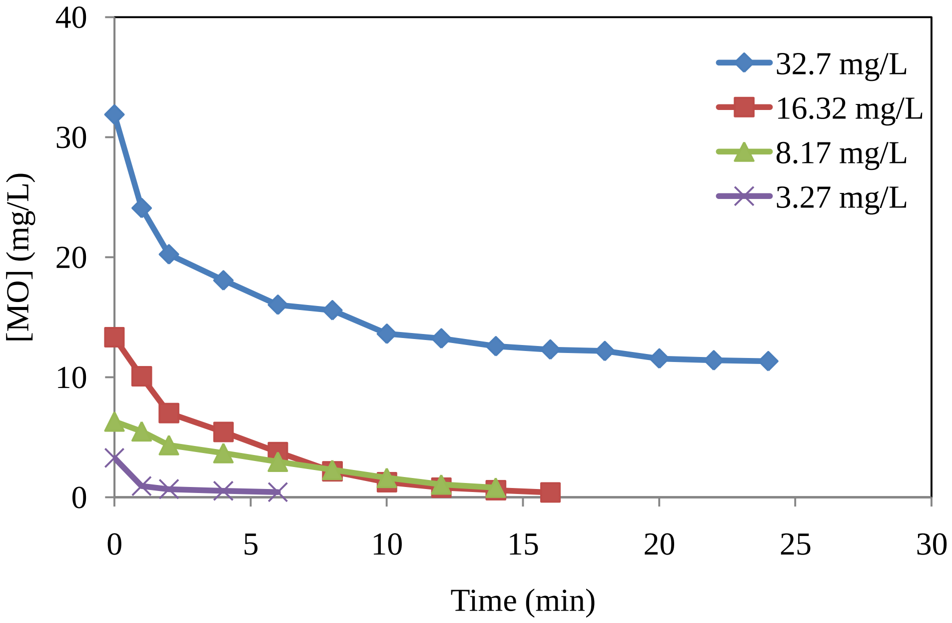

Figure 4.48. Photocatalytic decolorization of MO in the presence of 0.5M ZnO-FA at different initial MO concentrations. Conditions: pH: 5.85 (Natural), I= 4.7x10^{15} photons/s, T=298 K, Flow rate= 2000 rpm.

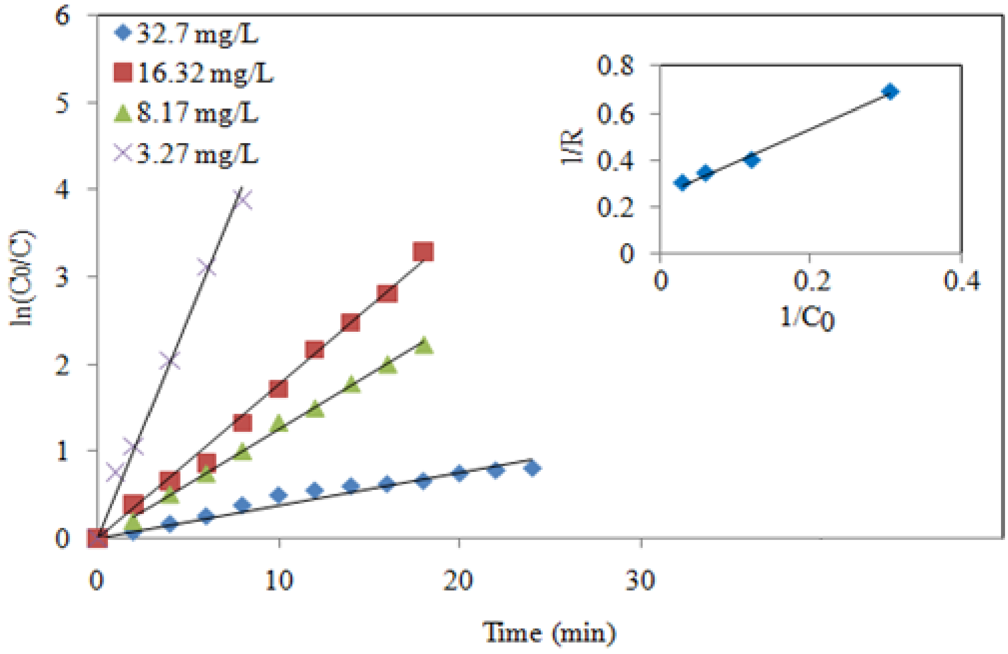

Figure 4.49. Pseudo-first order kinetics for degradation of MO. Inset: Langmuir-Hinshelwood plot for degradation of MO Conditions: pH: 5.85 (Natural), I= 4.7x10^{15} photons/s, T=298 K, Flow rate= 2000 rpm.

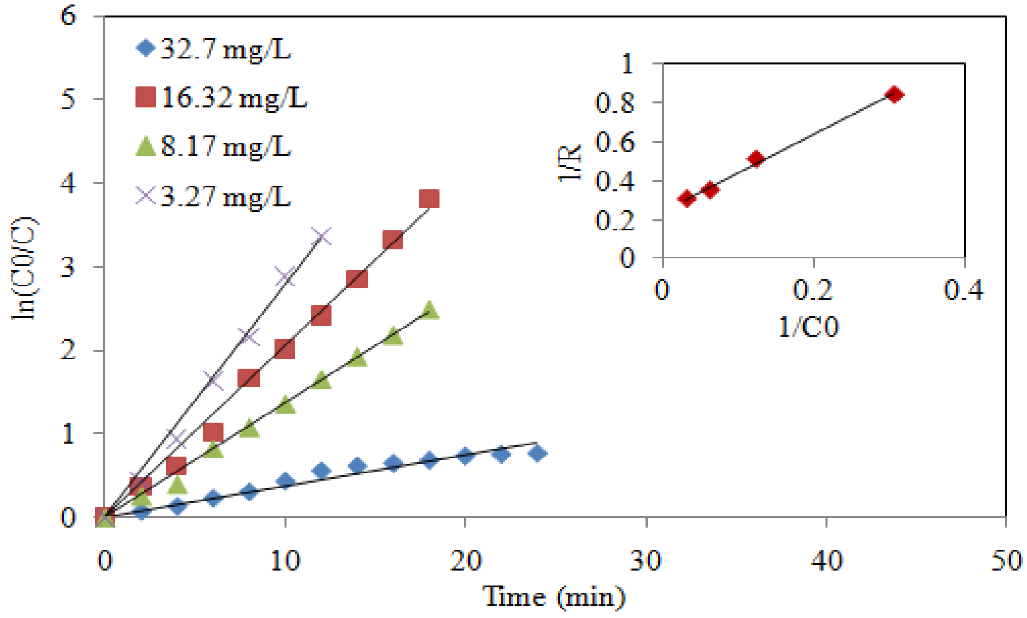

Figure 4.50. Pseudo-first order kineticsfor decolorization of MO. Inset: Langmuir-Hinshelwood kinetics for the decolorization. Conditions: pH: 5.85 (Natural), I= 4.7x10^{15} photons/s, T=298 K, Flow rate= 2000 rpm.

Table 4.6. First order rate constants (k) and linear regression values (R) for the photocatalytic degradation and decolorization processes of the different initial concentrations of MO in the presence of 0.5M ZnO-FA.

	k (min^{-1})		**R**	
$[MO]_0$ (mg/L)	**degradation**	**decolorization**	**degradation**	**decolorization**
32.7	0.0381	0.0373	0.9423	0.9456
16.3	0.1785	0.1364	0.9938	0.9941
8.17	0.2254	0.2045	0.9983	0.9984
3.27	0.5023	0.3534	0.9912	0.9931

Langmuir-Hinshelwood model was confirmed by the linearity in the plot of reciprocal rate (1/R) against reciprocal of MO concentrations ($1/C_0$) (Equation 3.12, Figure 4.49 inset, Figure 4.50 inset). The values of K and k were found to be 0.191 L/mg and 3.82 mg/L min for degradation while 0.122 L/mg and 4.17 mg/ L min for decolorization.

4.4.4. Reuse Properties of ZnO-FA Catalysts

To examine the stability of ZnO-FA catalysts, recycling experiments were carried out (Figure 4.51). For each new cycle, the 0.25M ZnO-FA catalyst was filtrated, washed and calcinated at 500^{o}C for 2 h. After four cycles, the concentration of MO remaining in solution was found to increase only 0.05 mg/L (from 0.06 to 0.11) for the degradation process and 0.06 mg/L (from 0.21 to 0.27) for the decolorization process. Thus, 0.25M ZnO-FA has a reuse property with a minor loss of the activity owing to the adsorption of the by-products on the catalyst after the first run or loose of the photocatalyst during each collection and rinsing steps. The EDX analysis after the fourth cycle did not show a significant variation in the percentage of Zn (about 53.2 wt %), indicating the stability of the supported catalyst (Appendix A, Figure A.4).

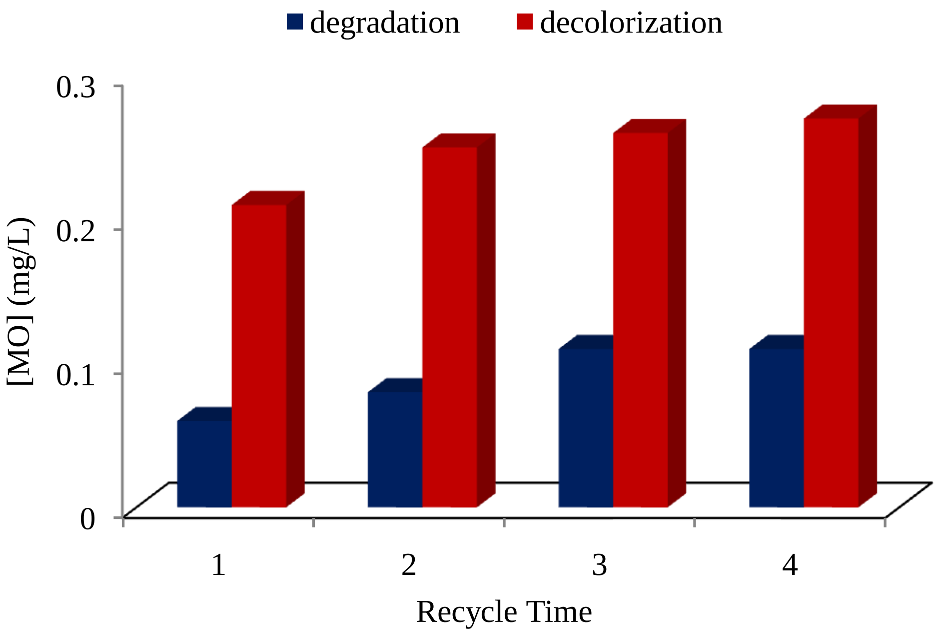

Figure 4.51. Results of recycling studies in the presence of 0.25M ZnO-FA. Conditions: pH: 5.85 (Natural), $[MO]_0$= 3.27 mg/L, I= $4.7x10^{15}$ photons/s, T=298 K, Flow rate= 2000 rpm.

4.4.5. Photocatalytic Experiments for Visible Light Irradiation

The photoactivities of 0.25M ZnO-FA and 0.5M ZnO-FA catalysts were also examined under visible light irradiation (Figure 4.52). After the dark adsorption experiments, only 17% and 30% decrements were observed in the remaining SA concentrations in the presence of 0.25M ZnO-FA and 0.5M ZnO-FA, respectively. This was in agreement with the UV-vis DRS profiles of the catalysts.

4.5. Postulated Mechanism for MO Decomposition

Oxidative degradation of azo dyes carried out by hydroxyl radicals, known as highly reactive electrophilic oxidants. It is believed that a series of transient intermediates usually invisible and unavoidable, are formed after the first attack of hydroxyl radical to the MO molecule. A mechanism is proposed in Figure 4.54. The parent molecule MO disintegrates mainly into two fragments (A and B).

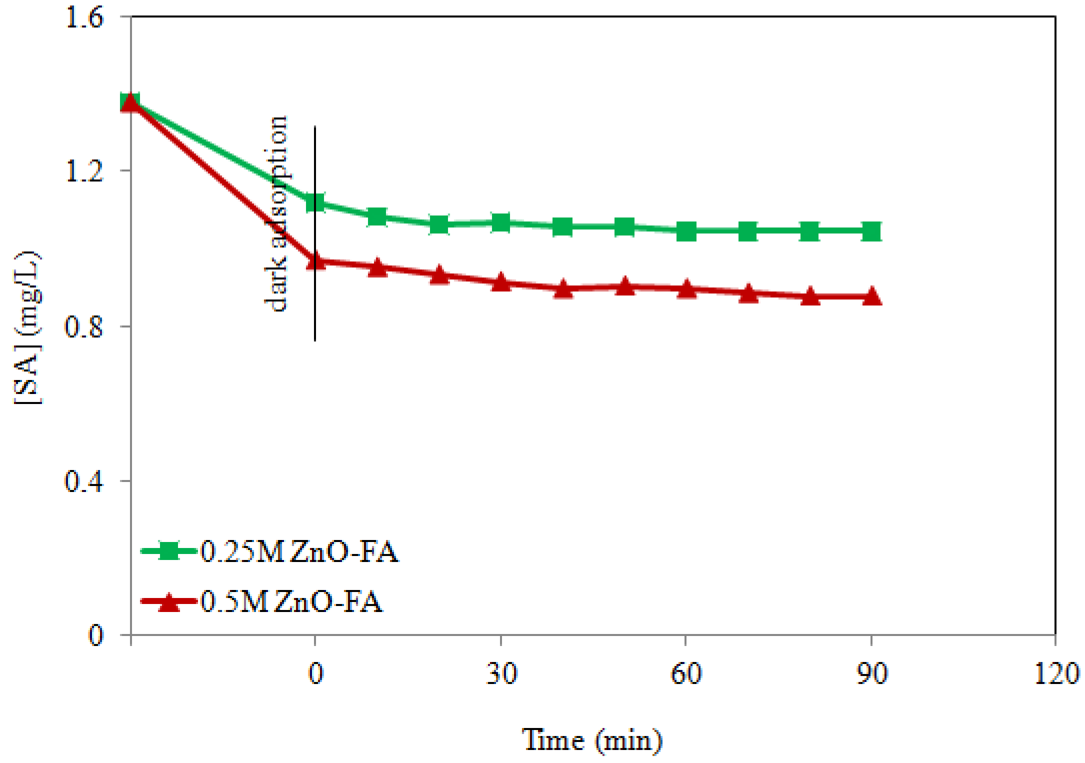

Figure 4.52. Photocatalytic degradation of salicylic acid with 0.25M ZnO-FA and 0.5M ZnO-FA catalysts under visible light irradiation. Inset: Photolysis of SA. Conditions: pH: 6.5 (Natural), $[SA]_0$=1.38 mg/L, T=298 K, Flow rate= 2000 rpm.

An initial •OH radical attack may occur on the sulfonic group with the the release of SO_4^{2-} anion. This results in the formation of compound A [97]. The C-N bonds in between the aromatic ring and azo bond is facile to rupture during the degradation process. Moreover, the attack of the •OH radical to the chromophoric group (-N=N-) causes rapid disappearance of the color [98]. Accordingly, hydroxybenzene (C), N,N-dimethylaniline (D) and N_2 gas can be formed [99]. Further •OH radical attacks to the N,N-dimethylaniline (D) leads to formation of (F) and (G- aniline) molecules. The ortho-para directing character of $–NH_2$ produces the 4-hydroxyaniline (H). Dihydroxybenzene molecule (I) and NH_4^+ anion form before the final oxidation route. Meanwhile, the dihydroxybenzene (E) can also be generated by the hydroxylation of hdyroxybenzene molecule (C).

An alternative MO degradation route may proceed by the substitution of methyl groups with hydrogen atoms in the aminic group. This results in the formation of product B [100]. Hereafter, the mechanism can follow two different pathways. In the first path, •OH attack to the remaining methyl group may lead to compound J. Then, further •OH attacks to the carbon atoms bearing the azo bond result in the formation of benzenesulfonic acid (L), aniline (M) and N_2 gas. These series may lead to the production of dihydroxybenzene molecule, NH_4^+ and SO_4^{2-} inorganic ions. In the second path, the sulfonic group in the molecule B can be hydroxylated with the appearance of K molecule. Hydroxybenzene (S) and N-methlyaniline (T) molecules may be generated by subsequent •OH attacks. The formation of dihydroxybenzene from these molecules can be suggested as the final point in the second path.

At the end of the proposed pathways, 1,4-Benzoquinone can be obtained by hydroxylation of dihydorxybenzene molecule (labeled as molecule E,I,O,R,U and Z) After the ring opening reaction, the aliphatic acids and carboxylic acids may be generated as intermediates. Inorganic anions (SO_4^{2-}, NH_4^+) can progressively form during the course of degradation. Although decolorization is believed to be very fast, complete mineralization of the dye to yield CO_2 and H_2O takes much longer [101].

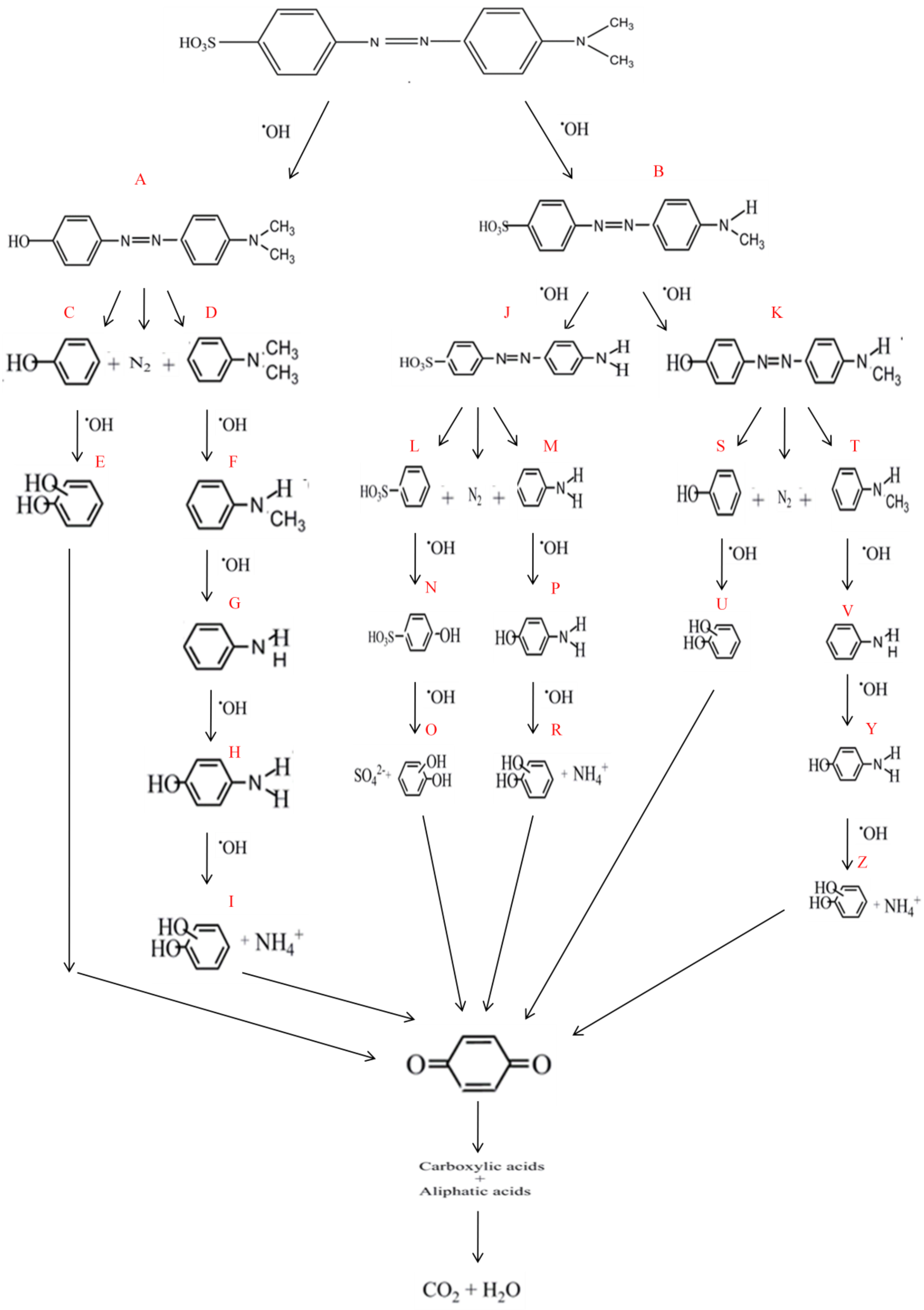

Figure 4.53. Proposed degradation mechanism of MO.

5. CONCLUSION

This study was based on two main supported catalyst systems; TiO_2-FA and ZnO-FA. Characterizations of the catalysts follow their detailed activity investigations. To sum up our experimental results, the following general remarks can be done.

TiO_2-FA catalysts: In the XRD analysis, only anatase diffractions were observed. Although TiO_2 nanoparticles did not show a significant difference in dimensions, the decrements in the reflections of the raw support suggested their uniform distribution throughout the surface and bulk. Also, variation in the FA morphology was noticeable with the addition of TiO_2 nanoparticles. Ti existence was evidenced by EDX and mapping analysis with the generation of a uniform layer on top of the spheres and/or formation of bright-distinct aggregates. The non-porous nature of the FA structure was transformed into a mesoporous adsorbent with the addition of TiO_2 nanoparticles. Thus, increments were detected in the surface areas and pore sizes of the supported catalysts. 25% TiO_2-FA catalyst exhibited a higher MO adsorption capacity in comparison to 25% TiO_2 and FA. The dark adsorption of the 25% TiO_2-FA catalyst obeyed the pseudo-second order kinetics. The Freundlich and Langmuir model isotherms were examined for the dark experiments. The Langmuir model was found to be applicable to our supported catalyst system by the higher correlation coefficients obtained in the linearized form of the equation. Accordingly, adsorption sites of the catalysts were assumed to be identical, energetically equivalent and accompanied with a monolayer coverage at the maximum amount of adsorption. An adsorption equilibrium was achieved within 30 min in the dark. These experiments followed by the irradiation runs, where progressive decrease in the absorption bands of the model compounds were controlled. Under UV irradiation, decolorization of MO was faster than the degradation due to the complexity in the destruction of the benzene rings. TiO_2 loading percentages were also effective in the degradation processes, while the catalyst with the highest TiO_2 content showed the best performance. The rate of photocatalytic reactions obeyed pseudo-first order kinetics, indicating an inverse relation between initial MO concentrations and the corresponding rate constants. Langmuir-Hinshelwood kinetic model was also applicable with the adsorption coefficients (K) and

the reaction rate constants (k) as 0.215 L/mg and 0.0163 mg/L min (for degradation) and 0.788 L/mg and 0.0237 mg/L min (for decolorization). Moreover, TiO_2-FA catalysts were found to be re-usable. However, visible light activities of the TiO_2-FA catalysts were much lower in comparison to UV light activities. This was in agreement with their DRUV spectra where the masking role of the FA was mostly responsible for the observed red shift in the patterns.

ZnO-FA Catalysts: The characteristic ZnO reflections were clearly observable in the XRD patterns of the ZnO-FA catalysts. The hollow structure of FA prohibited the aggregation of ZnO nanoparticles. This was evidenced by the decrease in the ZnO crystalline sizes with the increment in the loading concentration of ZnO. Meanwhile, uniform dispersion of ZnO nanoparticles on the surface was suggested owing to the decrements in the intensities FA peaks. SEM images together with EDX and mapping analysis demonstrated the presence of Zn within the matrix. A mesoporous structure also formed in ZnO-FA catalysts with higher surface areas, bigger pore volumes and dark adsorption capacities in comparison to the raw support and 0.25M ZnO. Pseudo-second order equation and Langmuir model adsorption isotherm were well fitted to the experimental data under dark conditions. Under UV irradiation, all ZnO-FA catalysts revealed very good photocatalytic activities with fast degradation and decolorization rates. The best photocatalytic activity was exhibited by the 0.5M ZnO-FA catalysts in less than 10 min. Effect of the initial MO concentration was examined and kinetics were confirmed by the pseudo-first order model. The adsorption coefficients (K) and the reaction rate constants (k) were found as 0.191 L/mg and 3.82 mg/L min (for degradation) and 0.122 L/mg and 4.17 mg/L min (for decolorization) by the application of Langmuir-Hinshelwood model. Likewise TiO_2-FA catalysts, ZnO-FA catalysts were re-usable and did not posses visible light activities.

These results indicated that both catalyst systems can be representative in supported catalyst matrixes. The significant FA transformation was observed for the first time and was analogous to its alteration to a porous material under time and alkaline treatments. The characterization techniques corroborated the porosity creation with in situ build up of TiO_2 or ZnO nanoparticles on the cenospheric surface. This eventually enhanced dark adsorption capacities and photocatalytic efficiencies of the TiO_2-FA and ZnO-FA catalysts under UV irradiation.

APPENDIX A: SEM AND MAPPING IMAGES

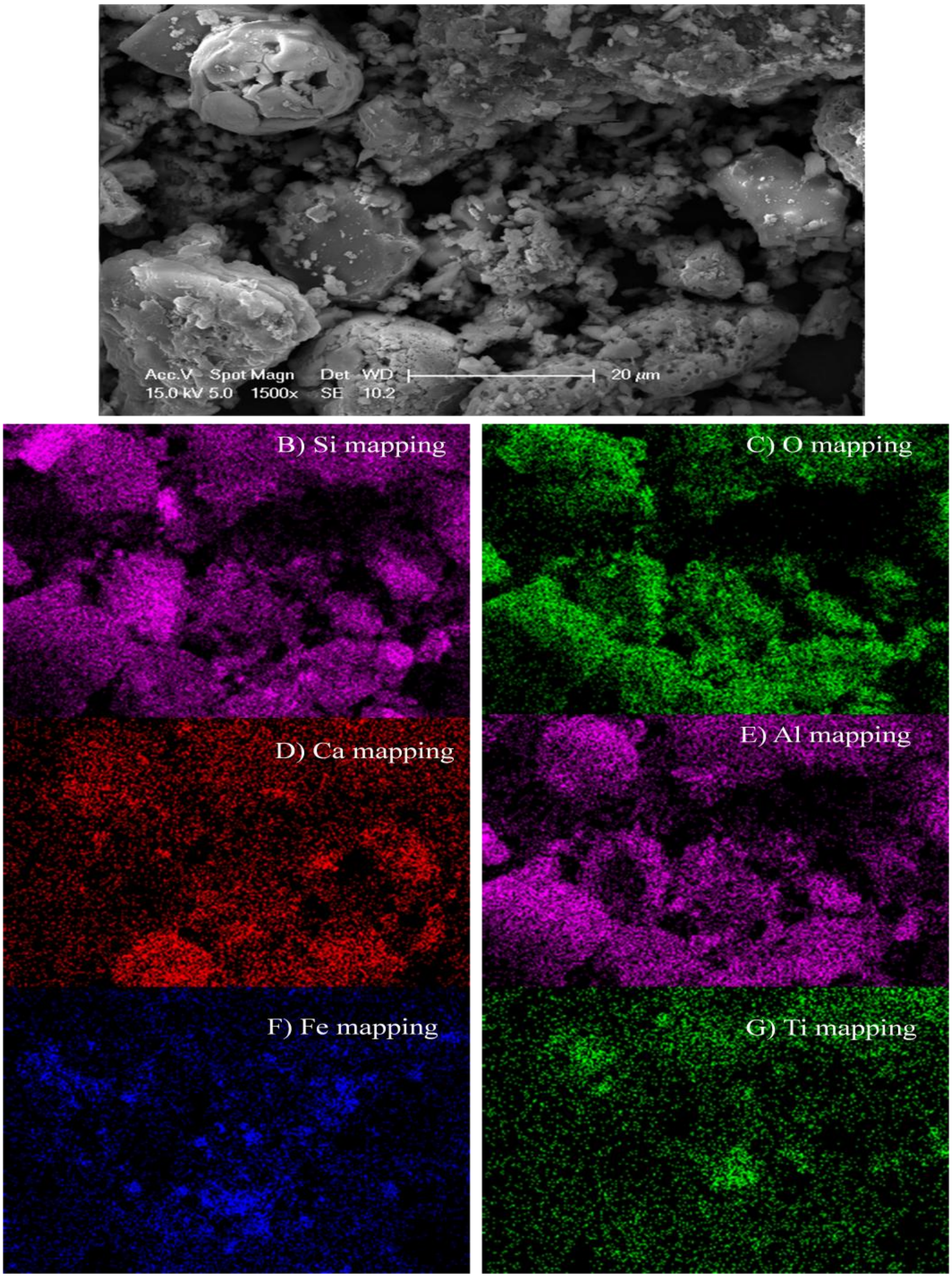

Figure A.1. SEM and mapping images of 40% TiO_2-FA after dark adsorption.

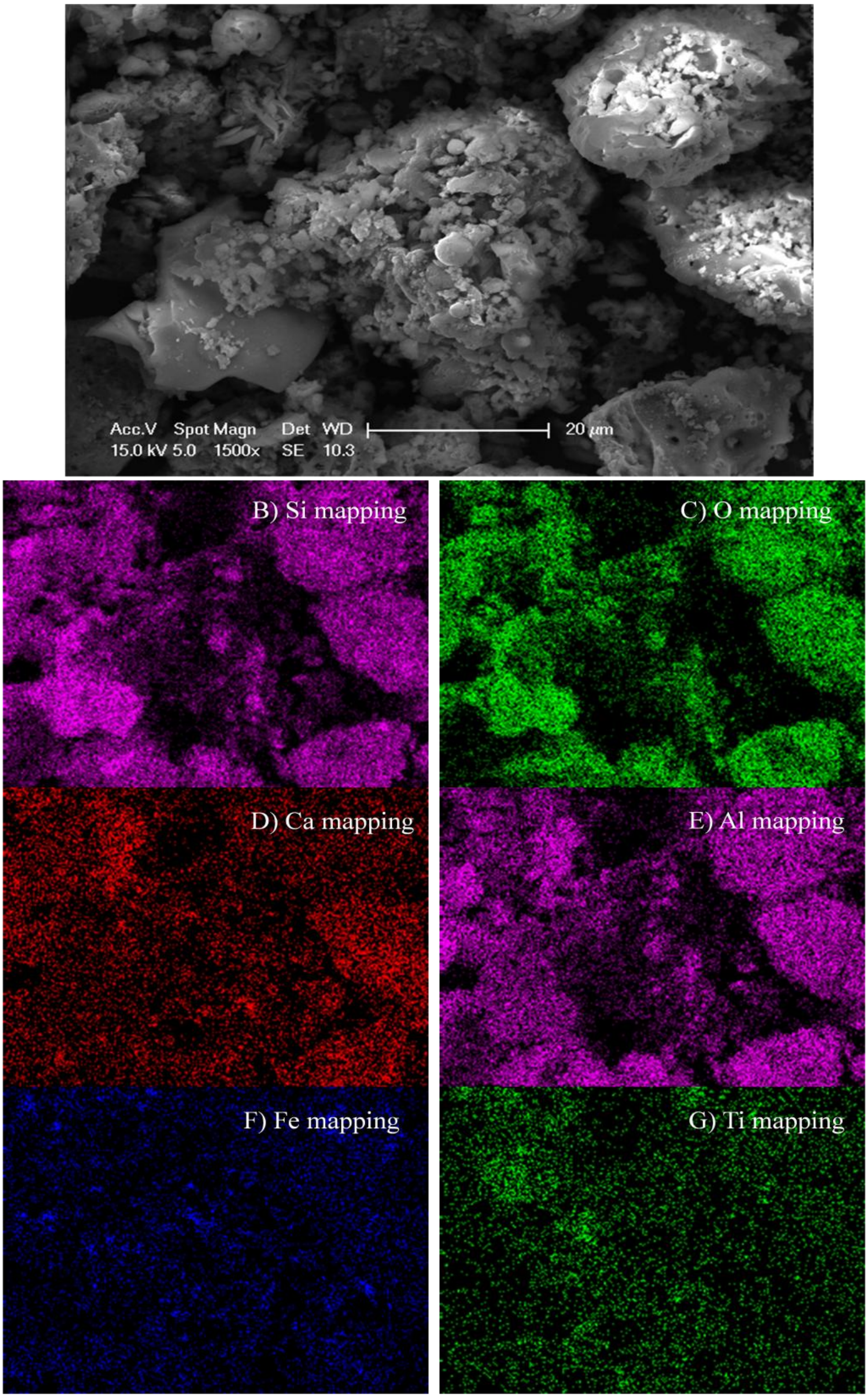

Figure A.2. SEM and mapping images of 40% TiO_2-FA after the fourth irradiation cycle.

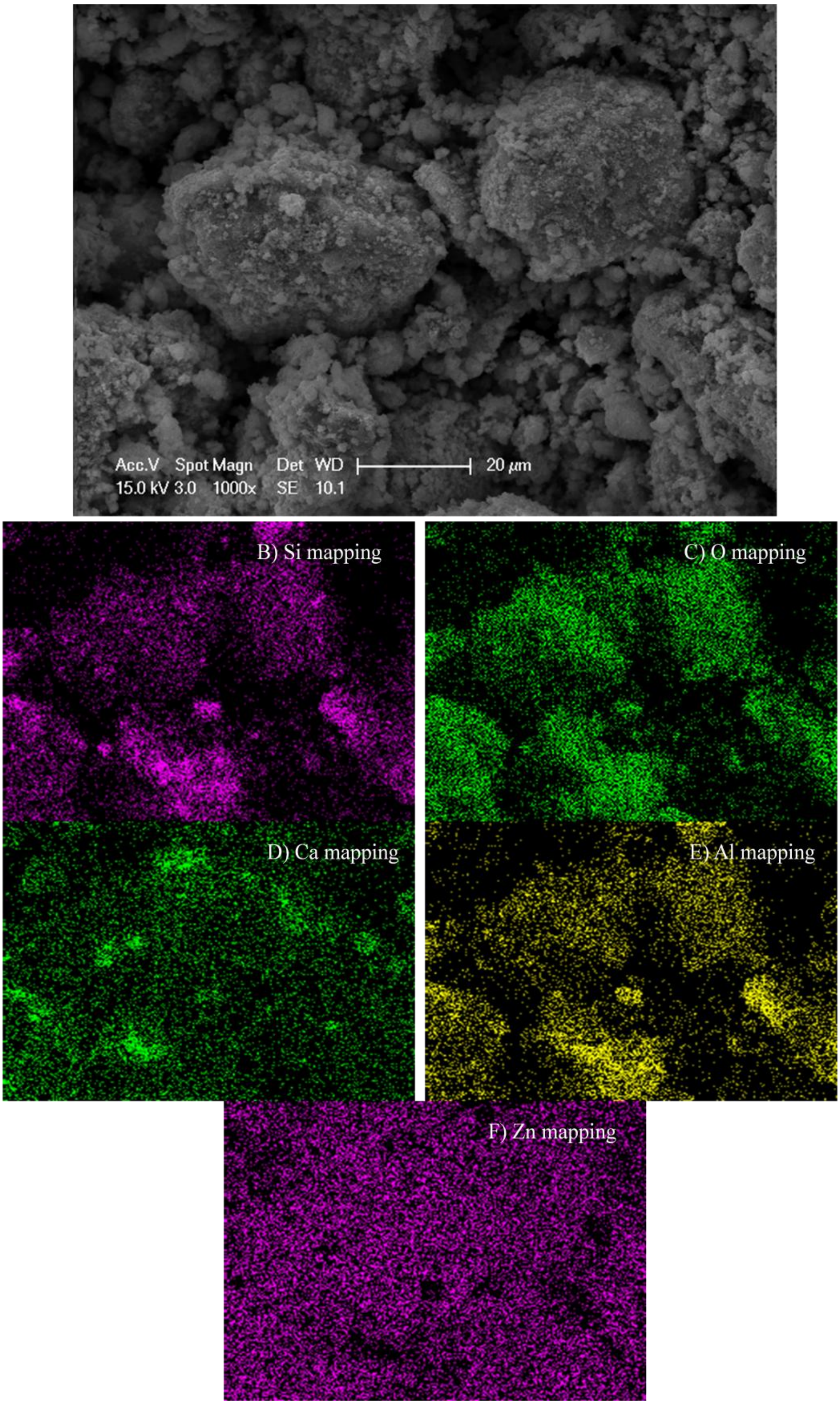

Figure A.3. SEM and mapping images of 0.25M ZnO-FA after dark adsorption.

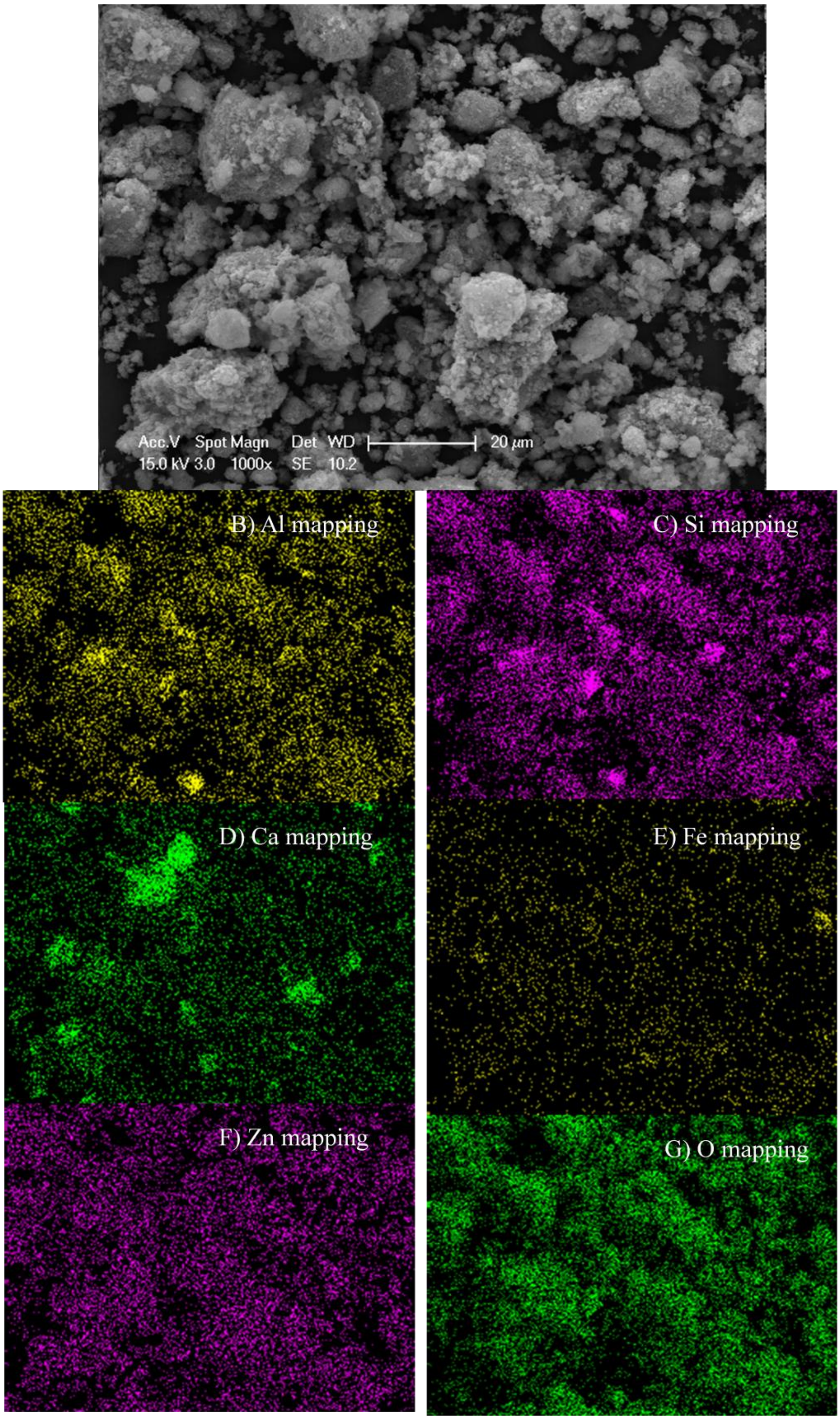

Figure A.4. SEM and mapping images of 0.25M ZnO-FA after the fourth irradiation cycle.

REFERENCES

1. Benitez, F. J., J. L. Acero, F. J. Real, “Degradation of Carbofuran by Using Ozone, UV radiation and Advanced Oxidation Processes”, *Journal of Hazardous Materials,* Vol. 89, pp. 51–65, 2002.

2. Mills, A., L. Hunte, “An Overview of Semiconductor Photocatalysis”, *Journal of Photochemistry and Photobiology A: Chemistry,* Vol. 108, pp. 1–35, 1997.

3. Slater, J. C., “Band Theory”, *Journal of Physics and Chemistry of Solids,* Vol. 8, pp. 21–25, 1959.

4. Yu, P. and M. Cardona, “Fundamentals of Semiconductors, Physics and Material Properties”, 2nd edition, Springer, New York, 1999.

5. Mahmoodi, N. M., M. Arami, N. Y. Limaee, N. S. Tabrizi, “Kinetics of Heterogeneous Photocatalytic Degradation of Reactive Dyes in an Immobilized TiO_2 Photocatalytic Reactor”, *Journal of Colloid and Interface Science,* Vol. 295, pp. 159–164, 2006.

6. Flores, N. M., U. Pal, E. S. Mora, “Photocatalytic behavior of ZnO and Pt-Incorporated ZnO Nanoparticles in Phenol Degradation”, *Applied Catalysis A: General,* Vol. 394, pp. 269-275, 2011.

7. Carp, O., C. L. Huisman, A. Reller, “Photoinduced Reactivity of Titanium Dioxide”, *Progress in Solid State Chemistry,* Vol. 32, pp. 33-177, 2004.

8. Marschall, R., L. Wang, “Non-Metal Doping of Transition Metal Oxides for Visible-Light Photocatalysis”, *Catalysis Today,* Vol. 225, pp. 111-135, 2014.

9. Natarajan, N. C., N. Funaga, G. Nogami, “Titanium Dioxide Thin Film deposited by Spray Pyrolysis of Aqueous Solution” *Thin Solid Films,* Vol. 322, pp. 6-8, 1998.

10. Macleod, H. A., *Thin Film Optical Filters*, 2nd edition, MacMillan, New York, 1986, p. 370.

11. Poluncheck, L., J. Elbel, L. Eckert, J. Blum, E. Wintermantel, H. M. Eppenberger, “Improved Cell Adhesion by Plasma-Induced Grafting of lactide onto Polyurethane Surface”, *Biomaterials*, Vol. 21, pp. 359-367, 2000.

12. Frank, S. N., A. J. Bard, “Heterogeneous Photocatalytic Oxidation of Cyanide Ion in Squeous Solution at TiO_2 Powder”, *Journal of the American Chemical Society*, Vol. 99, pp. 303-304, 1977.

13. Carp, O., C. L. Huisman, A. Reller, “Photoinduced Reactivity of Titanium Dioxide”, *Progress in Solid State Chemistry*, Vol. 32, pp. 33-177, 2004.

14. Zhang, H., J. F. Banfield, “Understanding Polymorphic Phase Transformation Behavior during Growth of Nanocrystalline Aggregates: Insights from TiO_2”, *Journal of Physical Chemistry B*, Vol. 104, pp. 3481-3487, 2000.

15. Kavan, L., B. O. Regan, A. Kay, M. Grätzel, “Preparation of TiO_2 (anatase) Films on Electrodes by Anodic Oxidative Hydrolysis of $TiCl_3$”, *Journal of Electroanalytical Chemistry*, Vol. 346, pp. 291-307, 1993.

16. Wu, Q., X. Chen, P. Zhang, Y. Han, X. Chen, Y. Yan, S. Li, “Aminoacid-Assisted Synthesis of ZnO Hierarchical Architectures and Their Novel Photocatalytic Activities”, *Crystal Growth and Design*, Vol. 8, pp. 3010–3018, 2008.

17. Cheung, J. T., *History and Fundamentals of Pulsed Laser Deposition, In: Pulsed Laser Deposition of Thin Films*, 1st edition, Wiley-Interscience, New York, 1994.

18. Klingshirn, C., “ZnO: Material, Physics and Applications”, *A European Journal of Chemical Physics and Physical Chemistry*, Vol. 8, pp. 782, 2007.

19. Dindar, B., S. Icli, “Unusual Photoreactivity of Zinc Oxide Irradiated by Concentrated Sunlight”, *Journal of Photochemistry and Photobioogy A: Chem*istry, Vol. 140, pp. 263–268, 2001.

20. Poulios, I., D. Makri, X. Prohaska, “Photocatalytic Treatment of Olive Milling Wastewater, Oxidation of Protocatechuic Acid”, *Global Nest: International Journal*, Vol. 1, pp. 55, 1999.

21. Lizama, C., J. Freer, J. Baeza, H. D. Mansilla, “Optimized Photodegradation of Reactive Blue 19 on TiO_2 and ZnO suspension”, *Catalysis Today*, Vol. 76, pp. 235-246, 2002.

22. Uddin, M., M. A. Hasnat, A. J. Samed, R. K. Majumdar, “Influence of TiO_2 and ZnO Photocatalysts on Adsorption and Degradation Behaviour of Erythrosine”, *Dyes and Pigments*, Vol. 75 pp. 207-212, 2007.

23. Pall, B. and M. Sharon, “Enhanced Photocatalytic Activity of Highly Porous ZnO Thin Films Prepared by Sol-Gel Process”, *Materials Chemistry and Physics*, Vol. 76, pp. 82-87, 2002.

24. Brunauer, S., P. H. Emmett and E. Teller, “Adsorption of gases in Multimolecular Layers”, *Journal of the American Chemical Society,* Vol. 60, pp. 309-319, 1938.

25. Atkins, P., J. Paula, *Atkin’s Physical Chemistry*, 7th edition, Oxford Universiy Press, New York, 2002.

26. Rivera A. P., Tanaka K., “Photocatalytic Degradation of Pollutant over TiO_2 in Different Crystal Structure”, *Applied Catalysis B: Environmental*, Vol. 3, pp. 37-44, 1993.

27. Wang, C., Zhang Z., “Photocatalytic Decomposition of Halogenated Organics over Nanocrystalline Titania”, *Nanostructured Materials,* Vol. 9, pp. 583-586, 1997.

28. Jung, Y. K., S. B. Park, “Anatase-phase Titania: Preparation by Embedding Silica and Photocatalytic Activity for the Decomposition of Tricholoroethylene”, *Journal of Photochemistry and Photobiology A: Chemistry,* Vol. 127, pp. 117-122, 1999.

29. Mohajerani, M. S., Mazloumi M., “Self-assembled Zinc Oxide Nanostructures via a Rapid Microwave-assisted Route”, *Journal of Crystal Growth,* Vol. 310, pp. 3621-3625, 2008.

30. Su, C., B. Y. Hong, C. M. Tseng, “Sol–gel Preparation and Photocatalysis of Titanium Dioxide”, *Catalysis Today,* Vol. 96, pp 119–126, 2004.

31. Wang, C., J. Y. Ying, “Sol-Gel Synthesis and Hydrothermal Processing of Anatase and Rutile Titania Nanocrystals”, *Chemistry of Materials,* Vol. 11, pp. 3113-3120, 1999.

32. Yin, H., Y. Wada, T. Kitamura, S. Kamb, “Hydrothermal Synthesis of Nanosized Anatase and Rutile TiO_2 Using Amorphous Phase TiO_2”, *Journal of Materials Chemistry,* Vol. 11, pp. 1694-1703, 2001.

33. Chen, H. S., R. V. Kumar, “Sol–gel TiO_2 in Self-Organization Process: Growth, Ripening and Sintering”, *RSC Advances,* Vol. 2, pp. 2294–2301, 2012.

34. Ding, X. Z., X. H. Liu, “Synthesis and Microstructure Control of Nanocrystalline Titania Powders via Sol-Gel Process”, *Materias Sciences and Engineering: A*, Vol. 224, pp. 210-215, 1997.

35. Fujitani, T. And J. Nakamura, “The Effect of ZnO in Methanol Synthesis Catalysts on Cu Dispersion and the Specific Activity”, *Catalysis Letters,* Vol. 56, pp. 119-124, 1998.

36. Mukhtar, M., L. Munisa, R. Saleh, “Co-Precipitation Synthesis and Characterization of Nanocrystalline Zinc Oxide Particles Doped with Cu^{2+} Ions”, *Materials Sciences and Applications,* Vol. 3, pp. 543-551, 2012.

37. Dijkstra**,** M. F. J, A. Michorius, H. Buwalda, "Comparison of the Efficiency of Immobilized and Suspended Systems in Photocatalytic Degradation", *Catalysis Today*, Vol. 66, pp. 487–494, 2001.

38. Roberto, L., M. A. Baltanfis, A. E. Cassano, "Supported Titanium Oxide as Photocatalyst in Water Decontamination: State of the Art", *Catalysis Today*, Vol. 39, pp. 219-231, 1997.

39. Yu, Y., "Preparation of Nanocrystalline TiO_2-Coated Coal Fly Ash and Effect of Iron Oxides in Coal Fly Ash on Photocatalytic Activity", *Powder Technology*, Vol. 146, pp.154–159, 2004

40. Vohra M. S., K. Tanaka, "Photocatalytic Degradation of Aqueous Pollutants Using Silica-Modified TiO_2", *Water Research*, Vol. 37, pp. 3992-3996, 2003.

41. Tanaka T., K. Teramura, T. Yamamoto, S. Takenaka, S. Yoshida, T. Funabiki, "TiO_2/SiO_2 Photocatalysts at Low Levels of Loading: Preparation, Structure and Photocatalysis", *Journal of Photochemistry and Photobiology A: Chemistry*, Vol. 148, pp. 277-281, 2002.

42. Yoneyama, H., T. Torimoto, "Titanium Dioxide/Adsorbent Hybrid Photocatalysts for Photodestruction of Organics Substance of Dilute Concentrations", *Catalysis Today*, Vol. 58, pp. 133-140, 2000.

43. Sun, Z., Y. Chen, Q. Ke, Y. Yang, J. Yuan, "Photocatalytic degradation of Cationic Azo dye by TiO_2/Bentonite Nanocomposite", *Journal of Photochemistry and Photobiology A: Chemisty*, Vol. 149, pp. 169-174, 2002.

44. Reddy, E. P., L. Davydov, P. Smirniotis, "TiO_2-Loaded Zeolites and Mesoporous Materials in the Sonophotocatalytic Decomposition of Aqueous Organic Pollutants: the Role of the Support", *Applied Catalysis B: Environmental*, Vol. 42, pp. 1-11, 2003.

45. Yoneyama, H., T. Torimoto, “Titanium Dioxide/Adsorbent Hybrid Photocatalysts for Photodestruction of Organic Substances of Dilute Concentrations”, *Catalysis Today*, Vol. 58, pp. 133-140, 2000.

46. Styszko-Grochowiak, K., H. Jankowski., S. Kozi, “Characterization of the Coal Fly Ash for the Purpose of Improvement of Industrial On-Line Measurement of Unburned Carbon Content”, *Fuel*, Vol. 83, pp. 1847–1853, 2004.

47. Bayat, O., “Characterisation of Turkish Fly Ashes”, *Fuel*, Vol. 77, pp. 1059-1066, 1998.

48. Wang, S. B, H. W. Wu, “Environmental-Benign Utilization of Fly Ash as Low-Cost Adsorbents”, *Journal of Hazardous Materials*, Vol. 136, pp. 482-501, 2006.

49. Blissett, R. S., Rowson N. A., “A Review of the Multi-Component Utilization of Coal Fly Ash”, *Fuel*, Vol. 97, pp. 1-23, 2012.

50. Ahmaruzzaman M., “A Review on the Utilization of Fly Ash”, *Progress in Energy and Combustion Science*, Vol. 36, pp. 327-363, 2010.

51. Iyer, R .S., J. A. Scott, “Power Station Fly Ash: A Review of Value-Added Utilization Outside of the Construction Industry Resources”, *Conservation and Recycling*, Vol. 31 pp. 217–228, 2001.

52. Akinyemi, S. A., A. Akinlua, W. M. Gitari, S. M. Nyale, R. O. Akinyeye, L. F. Petrik, “An Investigative Study on the Chemical, Morphological and Mineralogical Alterations of Dry Disposed Fly Ash During Sequential Chemical Extraction”, *Energy Science and Technology*, Vol. 3, pp. 28-37, 2012.

53. Ghosal, S., S. A. Self, “Particle Size-Density Relation and Cenosphere Content of Coal Fly Ash”, *Fuel*, Vol. 74, pp. 522–529, 1995.

54. Ahmaruzzaman, M., “A Review on Utilization of Fly Ash”, *Progress in Energy and Combustion Science*, Vol. 36 pp. 327–363, 2010.

55. Ngu, L., H. Wu, D. Zhang, “Characterization of Ash Cenospheres in Fly Ash from Australian Power Stations”, *Energy Fuels*, Vol. 21, pp. 3437–3445, 2007.

56. Anshits, N. N., O. A. Mikhailova, A. N. Salanov, A. G. Anshits, “Chemical Composition and Structure of the Shell of Fly Ash Nonperforated Cenospheres Produced from the Combustion of the Kuznetsk Coal”, *Fuel*, Vol. 89, pp. 1849-1862, 2010.

57. Inada, M., Y. Eguchi, N. Enomoto, J. Hojo, “Synthesis of Zeolite from Coal Fly Ashes with Different Silica-Alumina Composition”, *Fuel*, Vol. 84, pp. 299-304, 2005.

58. Manoharan, V., I. M. Yunusa, P. Loganathan, R. Lawrie, C. G. Skilbeck, M. D. Burchett, “Assessments of Class F Fly Ashes for Amelioration of Soil Acidity and Their Influence on Growth and Uptake of Mo and Se by Canola”, *Fuel*, Vol. 89, pp. 3498–504, 2010.

59. Holler, H., U. Wirsching, “Zeolite Formation from Fly Ash” *Forsch Miner*, Vol. 63, pp. 21-43, 1985.

60. Yao, Z. T., S. H. Tan, M. S. Xia, Y. Ye, J. H. Li, “Synthesis, Characterization and Sintering Behavior of Indialite Ceramic from Fly Ash”, Waste Management and Researches, Vol. 29, pp. 1090-1097, 2011.

61. Nyale, S. M., O. Babajide , G. D. Birch, N. Böke, L. F. Petrik, “Synthesis and Characterization of Coal Fly Ash-Based Foamed Geopolymer”, *Procedia Environmental Sciences*, Vol. 18, pp. 722–730, 2013.

62. Torralvo, A. F., C. Fernández-Pereira, “Recovery of Germanium from Real Fly Ash Leachates by Ion-Exchange Extraction”, *Miner Engineering*, Vol. 24, pp. 35–41, 2011.

63. Kao, P. C, J. H. Zheng, T. L. Huang, “Removal of Chlorophenols from Aqueous Solution by Fly Ash”, *Journal of Hazardous Materials*, Vol. 76, pp. 237–249, 2000.

64. Yu, Y., “Preparation of Nanocrystalline TiO_2-Coated Coal Fly Ash and Effect of Iron Oxides in Coal Fly Ash on Photocatalytic Activity”, *Powder Technology*, Vol. 146, pp. 154–159, 2004.

65. Cetin, S., E. Pehlivan, “The Use of Fly Ash as a Low Cost, Environmentally Friendly Alternative to Activated Carbon for the Removal of Heavy Metals from Aqueous Solutions”, *Colloids and Surfaces A: Physicochemical and Engineering Aspects*, Vol. 298, pp. 83–87, 2007.

66. Mohan, S., R. Gandhimathi, “Removal of Heavy Metal Ions From Municipal Solid Waste Leachate Using Coal Fy Ash as an Adsorbent”, *Journal of Hazardous Materials*, Vol. 169, pp. 351–359, 2009.

67. Visa, M., R. A. Carcel, L. Andronic, A. Duta, “Advanced Treatment of Wastewater with Methyl Orange and Heavy Metals on TiO_2, Fly Ash and Their Mixtures”, *Catalysis Today*, Vol. 144, pp. 137-142, 2009.

68. Huo, P., Y. Yan, S. Li, W. Huang, S.Chen, X. Zhang,” H_2O_2 Modified Surface of TiO_2/Fly-Ash Cenospheres and Enhanced Photocatalytic Activity on Methylene Blue”, *Desalination*, Vol. 263, pp. 258–263, 2010.

69. Huo, P., Y. Yan, S. Li, W. Huang, ”Floating Photocatalysts of Fly-Ash Cenospheres Supported AgCl/TiO_2 films With Enhanced Rhodamine B Photodecomposition Activity”, *Desalination*, Vol. 256, pp. 196-200, 2010.

70. Wang, B., Q. Li, W. Wang, Y. Li, J. Zhai, “Preparation and Characterization of Fe^{3+}-Doped TiO_2 On Fly Ash Cenospheres for Photocatalytic Application”, *Applied Surface Science*, Vol. 257, pp. 3473-3479, 2011.

71. Wu, D., P. Huo, Z. Lu, X. Gaoa, X. Liu, W. Shi, Y. Yan,” Preparation of Heteropolyacid/TiO_2/Fly-Ash-Cenosphere Photocatalyst for the Degradation of

Ciprofloxacin from Aqueous Solutions”, *Applied Surface Science,* Vol. 258, pp. 7008– 7015, 2012.

72. Wang, B., C. Li, J. Pang, X. Qing, J. Zhai, Q. Li, “Novel Polypyrrole-Sensitized Hollow TiO_2/Fly Ash Cenospheres: Synthesis, Characterization, and Photocatalytic Ability Under Visible Light”, *Applied Surface Science*, Vol. 258, pp. 9989– 9996, 2012.

73. Huo, P., Z. Lu, X. Liu, X. Liu, X. Gao, “Preparation Molecular/ions Imprinted Photocatalysts of La^{3+}@POPD/TiO_2/fly-ash Cenospheres: Preferential Photodegradation of TCs Antibiotics”, *Chemical Engineering Journal*, Vol. 198, pp. 273–80, 2012.

74. Visa, M., A. Duta, “TiO_2/Fly Ash Novel Substrate for Simultaneous Removal of Heavy Metals and Surfactants”, *Chemical Engineering Journal*, Vol. 223 , pp. 860–868, 2013.

75. Li, C., B. Wang, H. Cui, J. Zhai, Q. Li “Preparation and Characterization of Buoyant Nitrogen-doped TiO_2 Composites Supported by Fly Ash Cenospheres for Photocatalytic Applications”, *Journal of Material Science and Technology*, Vol. 29, pp. 835-840, 2013.

76. Lv, J., T. Sheng, L. Su, G. Xu, D. Wang , Z. Zheng, Y. Wu, “N, S co-Doped-TiO_2/Fly Ash Beads Composite Material and Visible Light Photocatalytic Activity”, *Applied Surface Science,* Vol. 284, pp. 229-234, 2013.

77. Li, B., Q. Hu, Z. Fu, C. Wang, “Preaparation of Fly Ash/Nano-ZnO Composites and Its Adsorption Properties for Reactive Dyes From Aqueous Solution, *Advanced Materials Research,* Vol. 726, pp. 2936-2939, 2013.

78. Liu, Z., Z. Liu, T. Cui, J. Li, J. Zhang, T. Chen, X. Wang, X. Liang, “Photocatalysis of Two-Dimensional Honeycomb-Like ZnO Nanowalls on Zeolite”, *Chemical Engineering Journal*, Vol. 235, pp.257–263, 2014.

79. Okte, A.N, D. Karamanis, “A Novel Photoresponsive ZnO-Flay Ash Nanocomposite for Environmental and Energy Applications”, *Applied Catalysis B: Environmental* Vol.142-143, pp. 538-552, 2013.

80. Okte, A. N., D. Karamanis, D. Tuncel, “Dual Functionality of TiO2-Fly Ash Nanocomposites: Water Vapor Adsorption and Photocatalysis”, *Catalysis Today* Vol. 230, pp. 205-213, 2014.

81. Qu, P., J. Zhao, T. Shen, H. Hidaka, “TiO_2-Assisted Photodegradation of Dyes: A Study of Two Competitive Primary Processes in the Degradation of RB in an Aqueous TiO_2 Colloidal Solution”, *Journal of Molecular Catalysis A: Chemical*, Vol. 129, pp. 257-268, 1998.

82. Easton, J. R., *Colour in Dyehouse Effluent*, The Alden Press, Oxford, UK, 1995.

83. Dai, S., Y. Zuhang, L. Chen, “Study on the Relationship Between Structure of Synthetic Organic Chemicals and Their Biodegradability”, *Environmental Chemistry*, Vol. 14, pp. 354-67, 1995.

84. Goi, A., Y. Veressinina, M. Trapido, “Degradation of Salicylic Acid by Fenton and Modified Fenton Treatment”, *Chemical Engineering Journal*, Vol. 143, pp. 1-9, 2008.

85. Kanekp, T., M. Fuji, T. Kodama and Y. Kıyatama, “Synthesis of Titania Pillared Mica in Aqueous Solution of Acetic Acid”, *Journal of Porous Materials* Vol. 8, pp. 99-109, 2001.

86. Anandan, S., A. Vinua, K.L.P. Sheeja Lovely, N. Gokulakrishnan, P. Srinivasu, T.Mori, V. Murugesan, V. Sivamurugan, K. Ariga, “Photocatalytic Activity of La-doped ZnO for the Degradation of Monocrotophos in Aqueous Suspension”, *Journal of Molecular Catalysis* Vol. 266, pp. 149–157, 2007.

87. Sayinöz, E., “*Characterization and Photocatalytic Activity of Sepiolite-*TiO_2 *and Na Montmorillonite-*TiO_2*-catalyst*”, M.S. Thesis, Bogazici University, 2006.

88. Zhou, L., C. Gao and W. Xu, “Magnetic Dendritic Materials for Highly Efficient Adsorption of Dyes and Drugs”, *ACS Applied Materials and Interfaces*, Vol. 2, pp. 1483–1491, 2010.

89. Zhou, M., X. Gao, Y. Hu, J. Chen, X. Hu, “Uniform Hamburger-like Mesoporous Carbon-Incorporated ZnO Nanoarchitectures: One-Pot Solvothermal Synthesis, High Adsorption and Visible-Light Photocatalytic Decolorization of Dyes”, *Applied Catalysis B: Environmental*, Vol.138, pp. 1-8, 2013.

90. Kim, S. H., H. H. Ngo, H. K. Shon, S. Vigneswaran, “Adsorption and Photocatalysis Kinetics of Herbicide onto Titanium Oxide and Powdered Activated Carbon” *Separation and Purification Technology*, Vol. 58, pp. 335–342, 2008.

91. Zhou, Li., C. Gao, W. Xu, “Magnetic Dendritic Materials for Highly Efficient Adsorption of Dyes and Drugs”, *ACS Applied Materials and Interfaces*, Vol. 2, pp. 1483-1492, 2010.

92. Liu, Y., Y. Li, Y.T. Wang, L. Xie, J. Zheng, X.G. Li, “Sonochemical Synthesis and Photocatalytic Activity of Meso- and Macro-Porous TiO_2 for Oxidation of Toluene, Journal of Hazardous Materials, Vol. 150, pp. 153-157, 2008.

93. Sreethawong, T., Y. Yamada, T. Kobayashi, S. Yoshikawa, “Catalysis of Nanocrystalline Mesoporous TiO_2 on Cyclohexene Epoxidation with H_2O_2: Effects of Mesoporosity and Metal Oxide Additives”, Journal of Molecular Catalysis A: Chemical, Vol. 241, pp. 23-32, 2005.

94. Yu, J., H. Yu, B. Cheng, C. Trapalis, “Effects of Calcination Temperature on the Microstructures and Photocatalytic Activity of Titanate Nanotubes”, *Journal of Molecular catalysis A: Chemical*, Vol. 249, pp. 135-142, 2006.

95. Zhou, M., X. Gao, Y. Hu, J. Chen, X. Hu, “Uniform Hamburger-Like Mesoporous Carbon-Incorporated ZnO Nanoarchitectures: One-pot

Solvothermal Synthesis, High Adsorption and Visible-Light Photocatalytic Decolorization of Dyes", *Applied Catalysis B: Environmental*, Vol. 138, pp. 1-8, 2013.

96. Shi, J., S. Chen, S. Wang, P. Wu, G. Xu, "Favorable Recycling Photocatalyst TiO_2/CFA: Effects of Loading Method on the Structural Property and Photocatalytic Activity", *Journal of Molecular Catalysis A: Chemical*, Vol. 303, pp. 141–147, 2009.

97. Dai, K., H. Chen, T. Peng, D. Ke, H. Yi, "Photocatalytic Degradation of Methyl Orange in Aqueous Suspension of Mesoporous Titania Nanoparticles", *Chemosphere*, Vol. 69, pp. 1361-1367, 2007.

98. Joseph, J. M., H. Destaillat, H. Hung and M. R. Hoffman, "The Sonochemical Degradation of Azobenzene and Related Azo Dyes: Rate Enhancements via Fenton's Reactions", *Journal of Physical Chemistry. A*, Vol. 104, pp. 301-307, 2000.

99. Spadaro, J. T., L. Isabelle and V. Renganathan, "Hydroxyl Radical mediated Deagradation of Azo Dyes: Evidence for Benzene Generation", *Environmental Science Technology*, Vol. 28, pp. 1389-1393, 1994.

100. Bianco, A, A. Basso, C. Baiocchi, M. Pazzi, G. Marci, V. Auguliaro, L. Palmisano, E. Pramauro, "Analytical Control of Photocatalytic Treatments: Degradation of Sulfonated Azo Dye", *Analytic Bioanalytic Chemistry*, Vol. 378, pp. 214-220, 2004.

101. Ioannis K., T. Albanis, "TiO_2-Assisted Photocatalytic Degradation of Azo Dyes in Aqueous Solution: Kinetic and Mechanistic Investigations", *Applied Catalysis B: Environmental*, Vol. 49, pp. 1-14, 2004.